3D PLUME MODELING OF SPT-100

BY

ARMAN TEKINALP

THESIS

Submitted in partial fulfillment of the requirements
for the degree of Master of Science in Aerospace Engineering
in the Graduate College of the
University of Illinois at Urbana-Champaign, 2019

Urbana, Illinois

Adviser:

Professor Deborah A. Levin

Abstract

Hall thrusters are a spacecraft propulsion device for orbit maintenance and north-south station keeping. One of the concerns about Hall thrusters is the sputtering of high energy ions which could result in the erosion of sensitive surface coatings used for solar cell elements and thermal control. In this thesis, a 3D DSMC-PIC hybrid kinetic simulation of a well known, stationary plasma thruster SPT-100 plume modeling was performed using a hybrid MPI-GPU AMR code CHAOS. Xe atoms, Xe^{+} and Xe^{+2} ions are modeled using a kinetic approach. Modeling electrons using a kinetic approach is not feasible in today's computational power for a Hall thruster plume. Thus three different models are used to compute the plasma potential. First, Boltzmann and polytropic models are used for electric potential calculations. Current density values obtained from both electron models are compared with previous experimental measurements and simulations in the literature. It was seen that the polytropic model shows better agreement with the experimental measurements than the Boltzmann model and previous studies. In order to implement more detailed models, an electron fluid model is implemented and is solved on an AMR octree grid using the preconditioned conjugate gradient method. Current density comparisons of the electron fluid model with the experimental measurements showed a worse comparison than the polytropic model for the selected parameters. The implemented electron fluid model is then compared with ion energy distributions from flight measurements and previous simulations and showed good agreement for the chosen parameters. In order to investigate the influence of solar panel voltage on a spacecraft plume, simulations using the electron fluid and the polytropic models were compared. It was seen that the spatial distribution of ions in the core plume and in the backflow region are similar for both electron models. Finally, sputtering calculations were performed and it was seen that the energies of ions that hit the solar panel are smaller than the threshold energy of alu-

minum, and so that there would be insignificant sputtering. This is because neutralized particles in the vicinity of the solar panel create a shield that protects the solar panel from the high energy CEX ions.

To my parents and my brother, for their love and support.

Table of Contents

List of Tables

List of Figures

List of Abbreviations

DSMC	direct simulation Monte Carlo
PIC	particle in cell
AMR	adaptive mesh refinement
CHAOS	Cuda-based hybrid approach for octree simulations
CEX	charge exchange collision
$FNUM$	number of real molecules which constitute a DSMC particle
MEX	momentum exchange collision
RPA	retarding potential analyzer

$\vec{B}$	magnetic field
C	space dependent coefficient
C_i	ionization rate
Δt	timestep
$\vec{E}$	electric field
E	relative energy of collision pair
ϵ_i	ionization energy
ε_0	permittivity of free-space
F	primary variable
γ	specific heat ratio or adiabatic constant
$\vec{J}$	current density
k	Boltzmann's constant

κ	electron conductivity
λ_D	Debye length
m	mass
n	number density
ν	collision frequency
q	elementary charge
p	pressure
ϕ	plasma potential
σ	collision cross-section
σ	electric conductivity
S	source term
T_e	electron temperature
θ	divergence angle
$\vec{v}_e$	electron velocity
v_{rel}	relative velocity
v_{th}^e	thermal velocity of electrons

Chapter 1

Introduction

Hall thrusters are a common spacecraft propulsion device for orbit maintenance and north-south station keeping. One of the concerns about Hall thrusters is the effect of the thruster plume on the spacecraft life [6]. The sputtering of high energy ions can cause erosion of sensitive surface coatings used for solar cell elements and thermal control. Although previously there have been ground-based facility tests, these could not replicate the space environment, due to so-called facility effects [7]. Thus, in order to understand the effect of charge exchange (CEX) ions, Hall thruster plumes are modeled.

Previously there have been 3D simulations of the SPT-100 thruster in vacuum conditions to investigate the effect of CEX ions on spacecraft. Researchers have used hybrid PIC-DSMC codes assuming isothermal (Boltzmann) [8] or isentropic (polytropic) [9] models for electrons or hybrid PIC-MCC codes assuming isothermal closure [10] for electrons. Boyd [5] has performed a 2D axisymmetric simulation of a SPT-100 thruster in a vacuum together with its cathode using a more detailed electron model than previous Boltzmann and polytropic models. However, the 2D axisymmetric assumption no longer holds, when there is a solar panel in the domain. Thus, it is important to develop 3D codes with detailed electron models to predict spacecraft-plume interactions.

Researchers have used 3D hybrid DSMC-PIC codes to model plume spacecraft interaction without modeling electrons as particles. Since the plasma potential has to be solved in the presence of a charged surface i.e. solar panel, and electrons are not modeled as particles, it is not possible to directly compute the electron number density term in Poisson's equation. One approach is to decompose the total potential into two parts and calculate the imposed external potential due to charged surfaces by solving the Laplace equation and then superimpose the plasma potential which is calculated from the Boltzmann relation [3, 11]. Another approach is to solve for the charged

surface and plasma potential together by solving Poisson's equation [12]. However, since the electrons are not particles, the electron number density term in the Poisson's equation is computed by inverting the Boltzmann relation. So the electron number density becomes the function of the plasma potential. A drawback of this method is that there is no need to solve expansive Poisson's equation for the quasi-neutral regions, where the Boltzmann relation can be easily applied to compute the plasma potential. Some researchers proposed to use a switch to overcome this inefficiency [13, 14, 15]. The switch self-consistently determines the quasi-neutral and non-neutral regions in the domain. For the quasi-neutral regions, researchers have used the Boltzmann relation or the polytropic relation and for the non-neutral regions, they have solved the Poisson's equation. However, there is a need for more detailed models other than the Boltzmann model or the polytropic model at quasi-neutral regions. Cichocki et. al. [15] have used a more detailed relation for the plasma potential in quasi-neutral regions, which is derived from the Ohm's Law, for their ion-thruster solar panel interaction modeling work. Nevertheless, they have used the polytropic model for electron temperature. To the best knowledge of authors, there has been no modeling of spacecraft Hall thruster plume interaction using the Poisson like potential equation together with electron energy equation.

In chapter 4 results of a 3D DSMC-PIC hybrid kinetic simulation of a well known, stationary plasma thruster SPT-100 plume is given. In this chapter, Xe atoms, Xe^{+}, and Xe^{+2} ions are modeled using a kinetic approach. For the electrons, since the plasma density of a Hall thruster plume is multiple orders of magnitude higher than mesothermal ion plumes, where the kinetic approach is applicable [16], applying a kinetic approach in a 3D plume calculation is not feasible in today's computational power. Thus, we assumed a quasi-neutral plasma and Boltzmann and polytropic closures are applied for electrons.

In chapter 5, a more detailed model for electrons similar to previous works in literature [17, 18, 19, 20] is implemented. However, different from the previous studies, the electron momentum and energy conservation equations are solved on an AMR octree grid for a 3D simulation using the preconditioned conjugate gradient method in a Particle in Cell (PIC) approach. After calculating the potential from the electron conservation equations, particles are moved on a PIC grid using the calculated electric field. In addition to

the PIC method, the well-known particle based Direct Simulation of Monte Carlo (DSMC) is used to simulate collisions between ions and neutral particles. Different from previous studies [15, 18, 20], species-based time-steps, and weights are used to overcome the inefficiency of using small time-steps for slow particles and artificially increasing the number of computational particles of trace species to realistically simulate the interactions between major and trace species [21]. Simulations are verified by comparing ion energy distributions at different locations with flight measurements [3, 4] and previous simulations [3, 5]. Simulation results of the electron fluid model are compared with the polytropic model results in the presence of a solar panel inside the domain. Finally, sputtering calculations of the solar panel is given for the electron fluid and the polytropic model.

Chapter 2

Collision and Plasma Models

2.1 Collision Models

The collisions between neutrals and ions that are modeled in this work are:

$$Xe(p_1) + Xe(p_2) \rightarrow Xe(p_1{}') + Xe(p_2{}') \tag{2.1}$$

$$Xe^{+}(p_1) + Xe(p_2) \rightarrow Xe^{+}(p_1{}') + Xe(p_2{}') \tag{2.2}$$

$$Xe^{+2}(p_1) + Xe(p_2) \rightarrow Xe^{+2}(p_1{}') + Xe(p_2{}') \tag{2.3}$$

$$Xe^{+}_{fast}(p_1) + Xe_{slow}(p_2) \rightarrow Xe_{fast}(p_1) + Xe^{+}_{slow}(p_2) \tag{2.4}$$

$$Xe^{+2}_{fast}(p_1) + Xe_{slow}(p_2) \rightarrow Xe_{fast}(p_1) + Xe^{+2}_{slow}(p_2) \tag{2.5}$$

where p_1 and p_2 are the pre-collisional momentum and $p_1{}'$ and $p_2{}'$ are the post-collisional momentum. For Xe-Xe collisions only momentum exchange reactions (MEX) are modeled using a collision cross-section [21] given by:

$$\sigma_{Xe-Xe} = \frac{2.117 \times 10^{-18}}{v_{rel}^{0.24}} \mathrm{m}^2 \tag{2.6}$$

where v_{rel} is the relative velocity between the selected collision pair.

In this study, it is assumed that ions and neutrals undergo only symmetric charge exchange (CEX) reactions. Since it has been shown previously that, symmetric charge exchange reactions have a one order of magnitude larger cross-section compared to asymmetric charge exchange reactions $\left(Xe^{+2}(p_1) + Xe(p_2) \rightarrow Xe^{+}(p_1{}') + Xe^{+}(p_2{}')\right)$ [22] . The symmetric

CEX collision cross-sections calculated by Miller et. al. are given below [23]:

$$\sigma^{CEX}_{Xe-Xe^{+}} = (87.3 - 13.6\log_{10}(E)) \times 10^{-20}\mathrm{m}^2 \tag{2.7}$$

$$\sigma^{CEX}_{Xe-Xe^{+2}} = (45.7 - 8.9\log_{10}(E)) \times 10^{-20}\mathrm{m}^2 \tag{2.8}$$

where E is the relative energy of the selected collision pair in the laboratory frame in eV. Since CEX reactions are long-range interactions, the charge is transferred between the two species and their velocities remain the same [6]. In previous work, it has been shown that ion-neutral collisions could result in pure charge exchange or momentum exchange collisions [15]. The singly charged ion-neutral MEX collision cross-section is given in [21] as Eq. 2.9. For doubly charged ions the MEX collision cross-section is chosen to be same as CEX collision cross-section for ions [24, 25, 26], since Boyd and Dressler, showed that, majority of CEX interactions occur at low scattering angles, at which the CEX and MEX cross-sections are the same [6]. MEX collision cross-section for doubly charged ions given as Eq. (2.10).

$$\sigma^{MEX}_{Xe-Xe^{+}} = (213.04 - 30.94\log_{10}(E))) \times 10^{-20}\mathrm{m}^2 \tag{2.9}$$

$$\sigma^{MEX}_{Xe-Xe^{+2}} = (45.7 - 8.9\log_{10}(E))) \times 10^{-20}\mathrm{m}^2 \tag{2.10}$$

2.2 Plasma Models

A Boltzmann relationship assuming a constant electron temperature was used to calculate the electric potential, previously used in Hall [1] and ion [21] thruster plume simulations, as given by

$$\phi = \phi_o + \frac{kT_e}{q}\ln\left(\frac{n_e}{n_o}\right) \tag{2.11}$$

where, ϕ_o is the reference potential, k is the Boltzmann's constant, T_e is the reference electron temperature, n_e is the electron number density and n_o is the reference plasma density. However, it has been reported that at the thruster exit the electron temperature is as high as 10 eV and in the far field,

it becomes 1-2 eV [6]. Moreover, the magnetic field of the Hall thruster due to permanent and electromagnets can leak into the plume region [6]. Based on the measurements taken by Kim [2], VanGilder [1] proposed an isentropic expansion model assumes that the electron number density decays as r^{-2} and the electron temperature scales as ${n_e}^{\gamma-1}$, where r is the radial distance from thruster axis [1]. Furthermore, Boyd and Dressler [6] proposed a more detailed approach assuming a polytropic expansion for electrons, which relates electron temperature and number density;

$$\frac{p}{p_o} = \left(\frac{n}{n_o}\right)^{\gamma} = \left(\frac{T}{T_o}\right)^{\frac{\gamma}{\gamma-1}} \tag{2.12}$$

where γ is the specific heat ratio or adiabatic exponent. Assuming that electrons are collisionless and unmagnetized and substituting the above equation into the conservation of electron momentum equation, one can obtain:

$$\phi = \phi_o - \frac{kT_e}{q}\frac{\gamma}{\gamma-1}\left[\left(\frac{n_e}{n_o}\right)^{\gamma-1} - 1\right] \tag{2.13}$$

In previous studies, Boyd and Dressler [6] assumed γ as 5/3, because Xe is a monatomic species. However, although this theoretical value is reasonable for a collisional gas plume in local thermodynamic equilibrium, Hall thruster plumes are nearly a collisionless plasma so expecting local thermal equilibrium is not physical. In addition to that, because of the additional degrees of freedom due to ionization, the adiabatic exponent has to be smaller than 5/3 [27]. Moreover, for a collisionless plasma with confined electrons, γ becomes 1 which is the isothermal limit also known as constant electron temperature limit. So for a partially confined plasma, the limits of the adiabatic exponent become $1 < \gamma < 5/3$. Thus, in order to decide the value of γ, Giono et. al. [28] measured the SPT-100 Hall thruster plume, electron number density, and temperature at three different mass flow rates and discharge voltages and found that the adiabatic exponent is lower than 5/3 for three operating points with $\gamma = 1.16 - 1.27$. In light of this information, the adiabatic exponent was chosen as 1.3, similar to Ref [9]. Since the polytropic model requires experimental measurements of electron temperature and number density to obtain the adiabatic exponent and also depending on the thruster operating point and thruster configuration [28] adiabatic exponent varies, a model independent of experimental data is required. Furthermore, adiabatic expo-

nent varies inside the plume as a function of position as shown by Nakles et. al. [29]. So assuming a single adiabatic exponent value is not correct. Thus, a more detailed model known as the electron fluid model has to be implemented.

The electron fluid model consists of three conservation equations, i.e. mass, momentum, and energy conservation. The electron mass conservation equation can be written as [18]

$$\frac{\partial n_e}{\partial t} + \nabla \cdot (n_e \vec{v}_e) = n_e n_n C_i \tag{2.14}$$

where n_e is the number density of electrons which can be obtained from ion number density assuming quasi-neutrality, $\vec{v}_e$ is the velocity of electrons, n_n is the number density of neutrals and C_i is the ionization rate term. For a quasi-neutral plasma, electron number density can be calculated using the below equation,

$$n_e = \sum_i Z_i n_i \tag{2.15}$$

where n is the ion number density and Z is the charge of the ion. Assuming a steady state flow and introducing a stream function $\nabla\psi = n_e\vec{v_e}$, the electron continuity equation can be transformed into a Poisson like equation, as given by

$$\nabla^2\psi = n_e n_n C_i \tag{2.16}$$

The ionization rate term can be calculated for an electron Maxwellian distribution for the range of electron temperatures relevant to Hall thruster [30] and is given below as,

$$C_i = \sigma_i v_{th}^e \left(1 + \frac{T_e \varepsilon_i}{(T_e + \varepsilon_i)^2}\right) \exp\left(-\frac{\varepsilon_i}{T_e}\right) \tag{2.17}$$

where T_e is the electron temperature in electron volts, ϵ_i is the ionization energy of xenon (12.1eV) [1] , $\sigma_i = 5 \times 10^{-20}$ m^2 is the reference cross-section and v_{th}^e is the thermal velocity of the electrons, as given by

$$v_{th}^e = \sqrt{\frac{8qT_e}{m\pi}} \tag{2.18}$$

The general form of Ohm's law derived from the electron momentum equa-

tion can be written as

$$\vec{E} = \frac{\vec{J}}{\sigma} - \vec{v}_e \times \vec{B} - \frac{1}{n_e q}\vec{\nabla} P_e \tag{2.19}$$

where $\vec{E}$ is the electric field, σ is the electric conductivity, $\vec{J}$ is the total current density, $\vec{B}$ is the magnetic field, q is the elementary charge and P_e is the electron pressure. If we assume that the total magnetic field $\vec{B}$ is zero, which decays rapidly after the thruster exit, and the ideal gas equation for electron pressure ($P_e = n_e q T_e$) holds, we obtain the total current density given below as,

$$\vec{J} = \sigma \vec{E} + \sigma \left(\nabla T_e + T_e \nabla \ln n_e \right) \tag{2.20}$$

where T_e is again the electron temperature in electron volts. Finally assuming current conservation

$$\nabla \cdot \vec{J} = 0 \tag{2.21}$$

we obtain a Poisson like equation for the electric potential given below

$$\nabla \cdot (\sigma \nabla \phi) = \nabla \cdot \sigma \left(\nabla T_e + T_e \nabla \ln n_e \right) \tag{2.22}$$

where ϕ is the electric potential. The electric conductivity, σ, is defined as,

$$\sigma = \frac{n_e q^2}{m_e \nu_e} \tag{2.23}$$

where ν_e is the total electron collision frequency between neutrals and ions ($\nu_e = \nu_{ei} + \nu_{en}$). The electron ion collision frequency can be written as [31]

$$\nu_{ei} = \frac{n_e q^4 \ln \Lambda}{2\pi \varepsilon_0^2 m_e^2 v_e^3} = \frac{n_e q^4 \ln \Lambda}{2\pi \varepsilon_0^2 m_e^2 (3 k T_e^K / m_e)^{3/2}} \tag{2.24}$$

where the Coulomb logarithm

$$\ln \Lambda = \ln \left(n_e \lambda_D^3 \right) \tag{2.25}$$

is depended on the electron Debye length

$$\lambda_D = \sqrt{\frac{\varepsilon_0 k T_e^K}{n_e q^2}} \tag{2.26}$$

where ϵ_0 is the permittivity of free-space and T_e^K is the electron temperature in Kelvin.

The electron-neutral collision frequency can be written as

$$\nu_{en} = n_n \sigma_{en} v_{th}^e \tag{2.27}$$

where σ_{en} is the electron neutral collision cross-section and taken as $10 \times 10^{-20}\text{m}^{-2}$ [32].

The electron energy equation can be written following [33] as:

$$\frac{D}{Dt}\left(\frac{3}{2} n_e k T_e^K\right) + p_e \nabla \cdot \vec{v}_e = \nabla \cdot \left(\kappa_e \nabla T_e^K\right) + \vec{J}_e \cdot \vec{E} - \sum_h \left[3 \frac{m_e}{m_h} \nu_{eh} n_e k \left(T_e^K - T_h^K\right)\right] - n_e n_n \varepsilon_i q C_i \tag{2.28}$$

where κ_e is the electron thermal conductivity, $\vec{J}_e \cdot \vec{E}$ is the Ohmic heating due to the electric field, m_e and m_h are the mass of the electron and heavy particle, ν_{eh} is the collision frequency between the electron and the heavy particle, T_h^K is the temperature of the particle in Kelvin and, ϵ_i is the first ionization energy of Xenon (12.1 eV [1]). Assuming that the electron energy equation reaches steady-state, we obtain

$$\frac{3}{2} n_e \left(\vec{v}_e \cdot \nabla\right) k T_e^K + p_e \nabla \cdot \vec{v}_e = \nabla \cdot \left(\kappa_e \nabla T_e^K\right) + \vec{J}_e \cdot \vec{E} - \sum_h \left[3 \frac{m_e}{m_h} \nu_{eh} n_e k \left(T_e^K - T_h^K\right)\right] - n_e n_n \varepsilon_i q C_i \tag{2.29}$$

Roy [34] noted that Ohmic term, $\vec{J}_e \cdot \vec{E}$ and convective terms, $\frac{3}{2} n_e (\vec{v}_e \cdot \nabla) k T_e^K + p_e \nabla \cdot \vec{v}_e$ are small compared to conductive terms, $\nabla \cdot \left(\kappa_e \nabla T_e^K\right)$. It was also noted by Mikellides [19] and Roy [34] that the contribution of energy transfer due to collisions between electron and heavy species to the total electron energy is small because the mass of heavy species is multiple orders of magnitude larger than the electrons. Thus we can neglect the term $3 \frac{m_e}{m_h} v_{eh} n_e k \left(T_e^K - T_h^K\right)$, where the subscript h represents heavy species, which

simplifies to,

$$\nabla \cdot \left(\kappa_e \nabla T_e^K\right) = n_e n_n \varepsilon_i q C_i \tag{2.30}$$

similar to the energy equation given in Ref. [20], where κ_e electron thermal conductivity defined as

$$\kappa_e = \frac{2.4}{1 + \frac{\nu_{ei}}{\sqrt{2}\nu_e}} \frac{k^2 n_e T_e^K}{m_e \nu_e} \tag{2.31}$$

Chapter 3

Numerical Implementation and Verification

3.1 Numerical Implementation

In this section, the numerical approach used in the DSMC module for heavy particle collisions and the PIC module for calculation of the electric field in the Cuda-based hybrid approach for octree simulations (CHAOS) is discussed. Particle movement in the DSMC/PIC modules is independent of the grid. Thus, the DSMC and PIC methods can be decoupled by using different grids. Using two separate grids is beneficial in order to resolve the dominant length scales for DSMC and PIC, which are the local mean-free path and local Debye lengths, respectively. CHAOS uses an adaptive mesh refinement (AMR) approach to refine cells in the domain depending on the dominant length scales. It has been known that at the thruster exit and in the sheath regions the Debye length is orders of magnitude smaller than the far-field regions. Thus, using a uniform mesh would result in an unnecessary number of cells. CHAOS uses a three-dimensional hierarchical tree structure known as an octree to store such an AMR grid. A flow chart of CHAOS showing the order in which DSMC and PIC modules are used is given in Fig. 3.1. Initializing particles (Initialize Particles) in the domain and applying boundary conditions (B.C. particles) to the particles are explained in sections 4.1 and 5.1. A detailed discussion about octree construction, distribution, load balancing, and particle mapping is given in [35, 16]. As the flowchart shows, the two grids constructed for the DSMC and PIC modules are known as a collision forest of octrees (C-FOT) and an electric forest of octrees (E-FOT). Both the C-FOT and E-FOT are refined and undergo division until the independent refinement criteria are met, creating leaf nodes from the roots in the refinement process. Leaf nodes correspond to the computational cells in a uniform grid. The electron fluid module in the PIC module of CHAOS

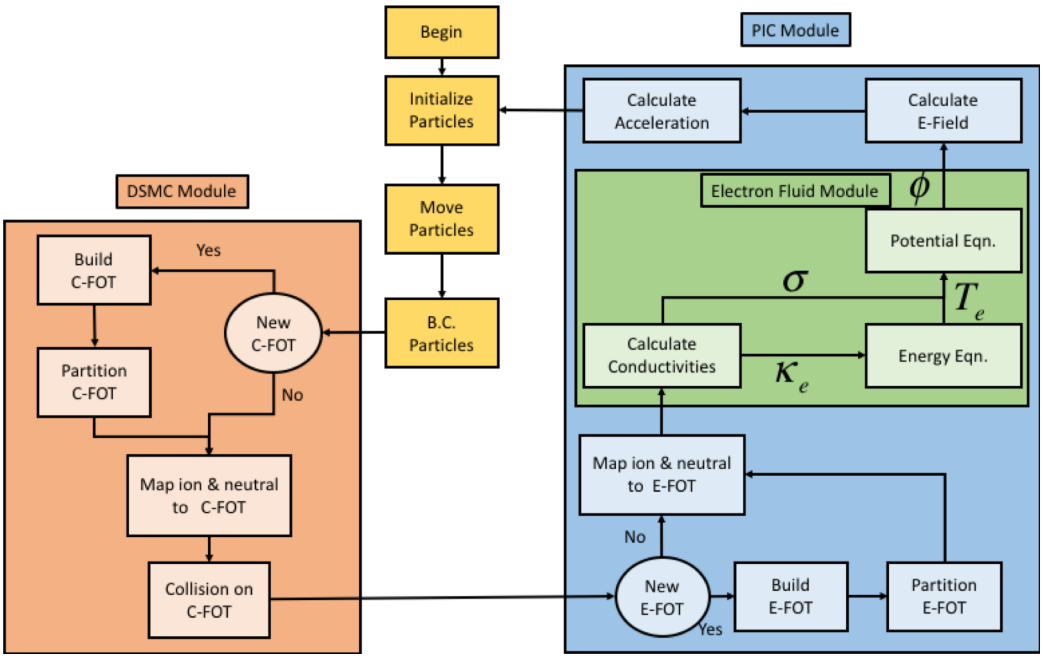

Figure 3.1: CHAOS flow-chart of DSMC/PIC modules. Particles refer to ions and neutrals.

first takes the ion and neutral species number densities in each leaf node and computes the electric conductivity (σ) and the thermal conductivity (κ_e). Using the electron energy equation (Eq. 2.30) the electron temperature in each leaf node is then computed using the Poisson solver with the user assigned thermal boundary conditions and the computed thermal conductivity. The final step in the electron fluid module is to calculate the plasma potential using the electron potential equation (Eq. 2.22). The electron potential equation takes the computed electron temperature and electric conductivity (σ) to compute the plasma potential using the Poisson solver with the user assigned electric boundary conditions. Functions and kernels used by the electron fluid module are given in Appendix A.

The electron continuity, momentum and energy conservation equations, Eqs. 2.16, 2.22, 2.30 become Poisson like equations which can be generalized as

$$\nabla \cdot (C(x,y,z)\,\nabla F(x,y,z)) = -S(x,y,z) \tag{3.1}$$

where $C(x,y,z)$ is the spatially dependent coefficient, i.e. the electric conductivity (σ) in Eq. 2.22 and in Eq. 2.30 the thermal conductivity (κ_e),

$F(x,y,z)$ is the primary variable, i.e. ϕ or Te whose spatial distribution we want to solve for, and $S(x,y,z)$ is the source term. For the electron continuity equation $C(x,y,z) = 1$ and Eq. 3.1 reduces to $\nabla^2 F(x,y,z) = -S(x,y,z)$.

The Poisson like equation given in Eq. 3.1 can be written on a 2:1 E-FOT using a cell centered finite volume approach and divergence theorem [19, 16].

$$\oint_S \left(C(x,y,z)\,\nabla F(x,y,z)\right)\cdot d\vec{S} = -\int_V S(x,y,z)\,dV \tag{3.2}$$

where, the integral is over the surface S and the control volume V is the E-FOT leaf node. The above equation can be discretized for the i^{th} octree cell or leaf node of the three-dimensional E-FOT as

$$\sum_{k=0}^{k<N_{fi}} \left(C_{ik}(x,y,z)\,\nabla F(x,y,z)\right) dS_{ik} = -S_i(x,y,z)\,dV_i \tag{3.3}$$

where, N_{fi}, is the number of face neighbors of the i^{th} leaf node, dS_{ik} is the face area shared between leaf node i and its k^{th} face neighbor, C_{ik} is the face value of the variable coefficient, i.e. electric or thermal conductivity, S_i is the leaf centered source term, and dV_i is the leaf node volume. Unlike a uniform grid cell that can have only one face neighbor for every face, in a 2:1 octree, a leaf node can have maximum of 4 neighbors for each of the six faces, i.e. a maximum of 24 neighbors (maximum value of $N_{fi} = 24$). The gradient, ∇F_{ik}, at the interface between leaf node i and its k^{th} face neighbor, leaf node j, is approximated using the central difference scheme,

$$\nabla F_{ik} = \frac{F_j(k) - F_i}{dx_{ij}},\ k \in \{0 - N_{fi}\} \tag{3.4}$$

where, F_i and $F_j(k)$ are the leaf-centered values for leaf node i and its k^{th} face neighbor, leaf node j, respectively, and dx_{ij} is the perpendicular distance between the centroid of leaf node i and j across shared face. The C_{ik} variable coefficient, i.e. the conductivity σ in Eq. (2.22) and κ_e in Eq. 2.30, has to be evaluated at the leaf node face. Using the leaf node cell centered and neighbor cell centered values. C_{ik} can be calculated using two averaging techniques. The first is arithmetic averaging,

$$C_{ik} = \frac{C_i + C_k}{2} \tag{3.5}$$

and the second method is based on harmonic averaging. Using the definition of harmonic averaging between neighboring cells [36] we obtain,

$$C_{ik} = dx_{ik} \left(\int_{x_i}^{x_k} C^{-1}(x, y, z) dx \right)^{-1} \tag{3.6}$$

Assuming C to be constant on each cell, this integral can be evaluated to give,

$$C_{ik} = dx_{i,k} \left(\frac{dx_i}{2C_i} + \frac{dx_k}{2C_k} \right)^{-1} \tag{3.7}$$

where dx is the leaf node dimension. Harmonic averaging becomes important when there are jumps by a few orders of magnitude in the conductivity. Thus, we have used harmonic averaging in this work. For example, the discretized form of Eq. 3.3 for leaf node 0 shown in Fig. 3.2, using Eq. 3.4 can be written as,

$$C_{01} \frac{F_1 - F_0}{dx_{01}} dS_{01} + C_{03} \frac{F_3 - F_0}{dx_{03}} dS_{03} + C_{05} \frac{F_5 - F_0}{dy_{05}} dS_{05} = -S_0 dV_0 \tag{3.8}$$

where, all the F, S_0 and V_0 are leaf-centred values; dx_{01} and dx_{03} are the perpendicular x-distances between the centroids of leaf node 0 and its right face neighbors 1 and 3 respectively; dy_{05} is the perpendicular y-distance between the centroids of leaf node 0 and its bottom face neighbor 5; and, dS_{0j} is the face shared area between leaf node 0 and its face neighbor leaf node j. For this example it is assumed that a homogeneous Neumann boundary condition is applied on the domain boundaries adjacent to leaf node 0, i.e. $dF_{\text{DominBndry}} = 0$. Grouping the coefficients of F_0 and its face neighbors F_j,

$$A_{00} F_0 - \sum_{j=0}^{j<N_{f0}} (A_{0j} F_j) = S_0 dV_0 \tag{3.9}$$

where, $A_{00} = \sum_{j=0}^{j<N_{f0}} (A_{0j})$ and $A_{0j} = C_{0j} \frac{dS_{0j}}{dx_{0j}}$ forms the non-zero coefficients of row 0 for the $N \times N$ sparse matrix, where N is total number of leaf

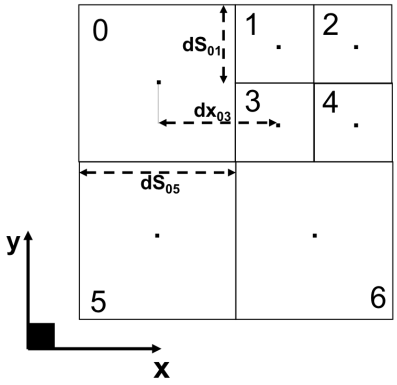

Figure 3.2: 2D quad-tree for domain decomposition illustration.

nodes in the domain. A more detalied discussion about the storage and communication of the elements of the A matrix among processors using GPUs can be found in [16].

Using the harmonic averaging technique to compute the conductivity (C) in Eq. 3.1 has an advantage over directly using the cell centered value for conductivity, because when the system of equations are combined and written in $Ax = b$ form, the A matrix becomes a symmetric, positive definite matrix, which can be solved using the preconjugate gradient method (PCG). If the cell centered values for the conductivity (C) were used, the A matrix would be non-symmetric and other methods such as the biconjugate gradient method would have to be used. The linearized system is solved using the PCG method given in [16].

3.2 Averaging verification

In this section, we initialize a domain with a known charge distribution to test the convergence of electric potential equation (Eq. 2.22) derived from Ohm's law with respect to an analytical solution. For this study we initialize a $(0.1 \times 0.1 \times 0.1)$ m domain with a linearly varying ion number density, such that $n_i = n_0 (z/L)$, where n_i is the ion number density at a given location (x, y, z), $n_0 = 1 \times 10^{15}/\text{m}^3$ and L is the dimension of the domain, i.e. 0.1 m. In this study particles are not moved and DSMC computations are not performed, because we are interested in the solution of the electric plasma equation (Eq. 2.22) in PIC module. A Dirichlet boundary of $\phi = 0$V is

applied at $z = 0.1$m boundary and the gradient of the plasma potential at all boundaries are set to zero for all remaining boundaries. We assume quasi-neutrality and equate the number density of ions to electrons in that cell, i.e., $n_i = n_e$. Also we assume a polytropic cooling for the electron temperature and calculate the electron temperature using the relation below,

$$T_e = T_{e_{ref}} \left(\frac{n_e}{n_{e_{ref}}} \right)^{\gamma - 1} \tag{3.10}$$

where T_e is the electron temperature, $T_{e_{ref}} = 2$eV is the reference electron temperature, n_e is the electron number density, $n_{e_{ref}} = 10^{13}/\mathrm{m}^3$ is the reference electron number density and $\gamma = 1.3$ is the adiabatic constant. The analytical expression for the plasma potential along the z-direction for the stationary charge density, after applying the boundary conditions and polytropic electron temperature model is

$$\phi(z) = \frac{\gamma}{\gamma - 1} T_{e_{ref}} \left(\frac{n_e}{n_{e_{ref}}} \right)^{\gamma - 1} \left(\left(\frac{z}{L} \right)^{\gamma - 1} - 1 \right) \tag{3.11}$$

In Fig. 3.3a comparison of analytic solution with harmonic averaging (Eq. 3.7) and arithmetic averaging (Eq. 3.5) methods are given for the solution of electric potential equation (Eq. 2.22). As can be seen, the harmonic averaging gives a better comparison compared to the arithmetic averaging method. The discrepancies between analytical and harmonic averaging at $z = 0$ m are because leaf nodes have a finite dimension and we use the cell center values of electron number density and temperature to compute the potential. Also, the plasma potential contour plot at the mid-plane of the harmonic averaging solution is given in Fig. 3.3c.

We have also tested our Poisson solver for a test case without computational macro-particles. We assigned an electron (and therefore ion) number density to every leaf node based on its center z-coordinate using the linearly varying electron number density relation, i.e. $n_i = n_0 (z/L)$. In Fig. 3.3b comparison of the arithmetic, harmonic, and analytic solutions for a simulation without computational macro-particles is given along with the plasma potential contours in Fig. 3.3d. It can be seen from the figure that, both arithmetic and harmonic averaging methods match perfectly with the analytical solution. The reason we do not see a perfect match between arithmetic, harmonic and analytical solution, for the test case with computational

macro-particles, i.e. Fig.3.3a-c, is that at the first time-step we initialize a uniform grid to randomly generate computational macro-particles in the leaf nodes. After macro-particles are generated, the uniform grid is erased and the octree-grid is constructed. During the octree-grid refinement step, leaf nodes are refined based on the Debye length which is related to the number of macro-particles. After the refinement step is completed, sometimes in the new leaf nodes the number of particles can be different from its neighbors which have the same z-coordinate. This is because, at the computational macro-particle initialization step, we randomly created particles in each leaf node. Thus, after the octree refinement step, the ion number density of particles can be different for leaf-nodes that have the same z-coordinate and this affects the electric potential calculation and causing the small discrepancies seen in Fig. 3.3a, when the harmonic averaging method is used, we obtain better agreement with the analytic solution. The reason for this agreement is because harmonic averaging is a better smoothing operation than arithmetic averaging. Thus, for the remainder of the simulation results shown in this work we are going to use the harmonic averaging to calculate conductivity values.

3.3 Energy equation solution verification

In this section the implemented energy equation (Eq. 2.30) is verified by comparison with the bvp4c boundary value solver module of MATLAB. Similar to the test case in section 3.2, we consider a $(0.1 \times 0.1 \times 0.1)$ m domain with a linearly varying ion number density, i.e. $n_i = n_0 \, (z/L)$, where n_i is the ion number density at a given location (x, y, z), $n_0 = 1 \times 10^{15}/\mathrm{m}^3$ and L is the dimension of the domain, i.e. 0.1 m in this case. The gradient of the electron temperature was set to zero on all of the domain boundaries, except at $z = 0$ and $z = 0.1$m, where in these boundaries electron temperature was set to $20,000$K and $80,000$K, respectively. In this section ionization was not considered, but the effects of ionization on the electron temperature is discussed in section 3.4.

The MATLAB bvp4c boundary value solver for ordinary differential equations is used to obtain a reference result for comparison. A 1D solution is obtained using the MATLAB program, since the change of electron temper-

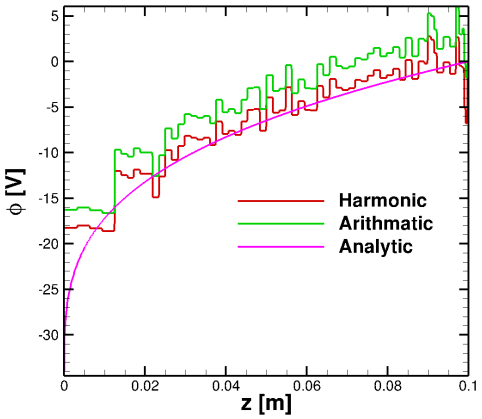

a) Plasma potential comparison with computational particles.

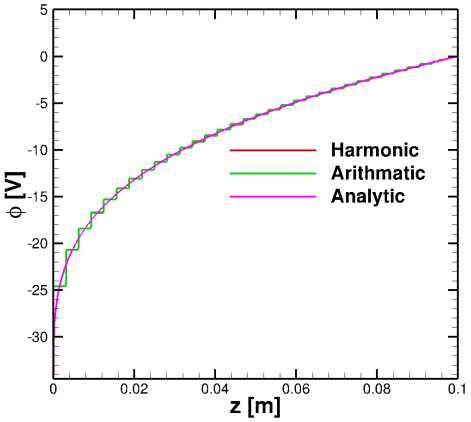

b) Plasma potential comparison without computational particles.

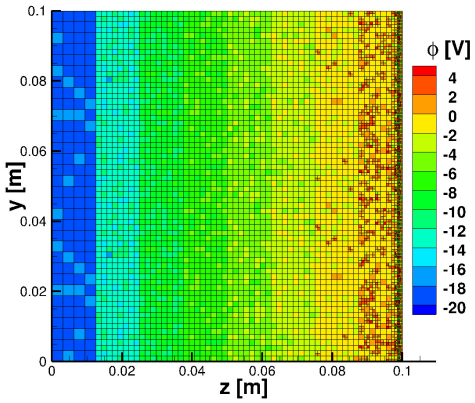

c) Mid-plane plasma potential contour plot with computational particles.

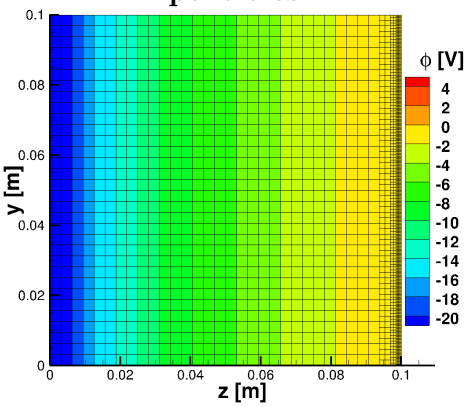

d) Mid-plane plasma potential contour plot without computational particles.

Figure 3.3: Test case for averaging method and plasma potential equation (Eq. 2.22) verification.

ature is only in the z-direction. First, we write the energy equation in Eq. 2.30 as a 1D equation given below,

$$\frac{d}{dz}\left(\kappa_e \frac{dT_e^K}{dz}\right) = n_e n_n \varepsilon_i q C_i \tag{3.12}$$

After taking the derrivatives with respect to z and doing some mathematical manupulations we obtain,

$$\frac{d^2T_e^K}{dz^2} = -\frac{1}{\kappa_e}\frac{d\kappa_e}{dz}\frac{dT_e^K}{dz} + \frac{1}{\kappa_e} n_e n_n \varepsilon_i q C_i \tag{3.13}$$

where both κ_e and T_e^K are function of z. Now we need to write κ_e as a function of T_e^K. First assuming $\ln\Lambda \approx 10$ [37] and writing the constants as a one term, C_1, the electron ion collision frequency given in Eq. 2.24 turns into

$$\nu_e = \nu_{ei} = C_1 n_e / \left(T_e^K\right)^{3/2} \tag{3.14}$$

where n_e and T_e^K are functions of z. Assuming there are no neutrals in the domain and setting the total collision frequency to the electron-ion collision frequency and writing constants as one term, C_2, in the electron thermal conductivity relation given in Eq. 2.31, we obtain

$$\kappa_e = C_2 n_e T_e^K / \nu_{ei} \tag{3.15}$$

Now subsituting Eq. 3.14 into Eq. 3.15, we obtain a relation for thermal conductivity as a function of electron temperature T_e^K only given by,

$$\kappa_e = C_3 \left(T_e^K\right)^{5/2} \tag{3.16}$$

which is similar to the expression given in [38] when electron-ion collisions are dominant. After substituting Eq. 3.16 into Eq. 3.13 without ionization ($C_i = 0$), we obtain a 1D energy equation,

$$\frac{d^2T_e^K}{dz^2} = -\frac{5}{2}\frac{1}{T_e^K}\left(\frac{dT_e^K}{dz}\right)^2 \tag{3.17}$$

which is only function of electron temperature. In Fig. 3.4a comparison of electron temperature solution using CHAOS and MATLAB bvp4c is given and it can be seen that there is good agreement between the two solutions.

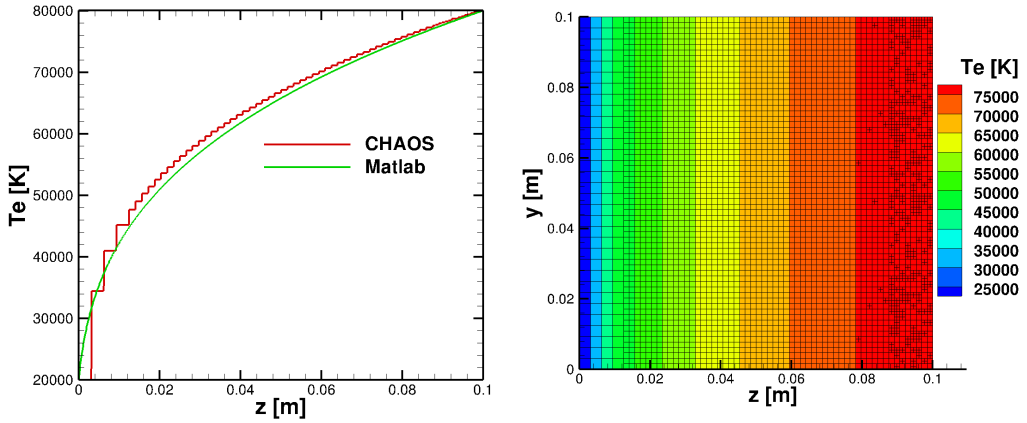

a) Comparison CHAOS vs MATLAB solution

b) Electron temperature plot at midplane

Figure 3.4: Test case results for energy equation solution confirmation.

Also, the electron temperature distribution in the domain as a contour plot is given in Fig. 3.4b. This agreement between two solutions concludes that, the energy equation given in Eq. 2.30 solved correctly without ionization.

3.4 Effect of ionization on electron temperature

In this section the effect of ionization on the electron temperature is investigated using a 1D test case. Taccogna [38] explained that electron thermal conductivity scales as $\kappa_e \propto \left(T_e{}^K\right)^{5/2}$ if the electron temperature is smaller than 2 eV, where electron-ion collision effects are higher. For electron temperatures greater than 2 eV, where electron-neutral collision effects are higher, scales as $\kappa_e \propto \left(T_e{}^K\right)^{1/2}$ [38]. Assuming electron temperatures greater than 2 eV and taking into account electron-neutral collisions, the energy equation given below is obtained,

$$\frac{d^2T_e^K}{dz^2} = -\frac{1}{2}\frac{1}{T_e^K}\left(\frac{dT_e^K}{dz}\right)^2 + \frac{1}{\kappa_e} n_e n_n \varepsilon_i q C_i \tag{3.18}$$

Setting conditions similar to the test case discussed in section 3.3 with ionization and setting neutral number density equal to electron number density, we did four different simulations to see the effect of ionization. Comparison plots with and without ionization are given in Fig. 3.5. It can be seen that

for electron temperatures above 4 eV and neutral number densities above $1 \times 10^{18}/\mathrm{m}^3$, ionization effects becomes important and electron temperature decreases. Similarly, after implementing the electron energy equation (Eq. 2.30) with ionization terms in CHAOS, thruster simulations were done and the effect of ionization on electron temperature was not been seen for the conitions given in Table 5.1-5.2. Furthermore one more test case was done to check our implementation with ionization terms. Similar to the test case in section 3.3, we consider a $(0.1 \times 0.1 \times 0.1)$ m domain with a linearly varying ion number density, i.e. $n_i = n_0 \, (z/L)$, where n_i is the ion number density at a given location (x, y, z), $n_0 = 5 \times 10^{19}/\mathrm{m}^3$ and L is the dimension of the domain, i.e. 0.1 m in this case. The neutral number density was set equal to the ion number density. The gradient of the electron temperature was set to zero on all of the domain boundaries, except at $z = 0$ and $z = 0.1$m, where in these boundaries the electron temperature was set to $80,000$K and $100,000$K, respectively. In Fig. 3.6 the electron temperature distribution with and without ionization terms and percentage difference is given. It can be seen that, the electron impact ionization reduces the electron temperature, however, the effect of ionization on electron temperature is not larger than 3%. In other words, for plume simulations which are at low number density and cold electron temperatures ionization can be neglected. Similarly, Boyd noted that ionization effects are not important for the plume modeling of the SPT-100 thruster conditions [18, 5]

3.5 Specular wall boundary implementation

In previous works [6, 20, 26] Hall thruster modeling was performed using axisymmetric codes because of the existing symmetry of the plume with respect to the thruster centerline. Even the researchers modeling Hall thrusters with a cathode, have used an axisymmetric assumption by stating that electrons from the cathode move very fast due to their light mass and equilibrate with the flow immediately [5, 26]. In this work, we model a quarter of the thruster in a 3D simulation assuming that the flow is symmetric around the z-axis. In Fig. 3.7a the number density of Xe^+ ions for a quarter of the thruster simulation is shown. In this simulation, the walls at $x = 0$ m and $y = 0$ m are specular or symmetric and the rest of the boundary conditions are outflow.

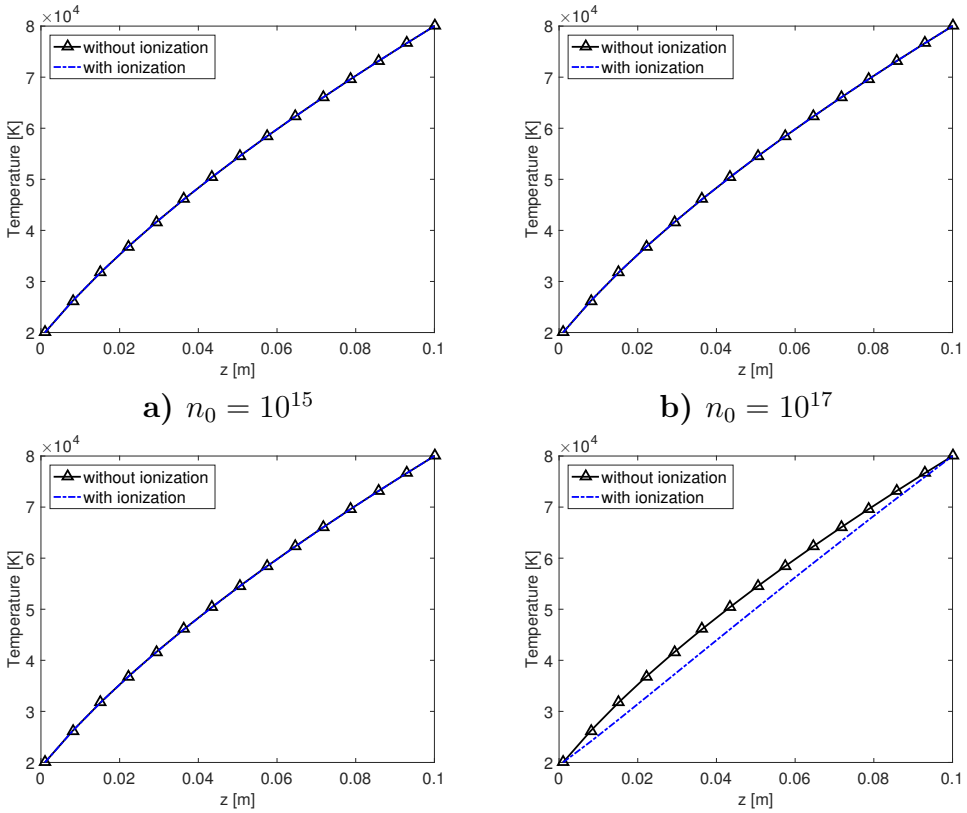

a) $n_0 = 10^{15}$ **b)** $n_0 = 10^{17}$

c) $n_0 = 10^{18}$ **d)** $n_0 = 10^{19}$

Figure 3.5: Test case for ionization at different electron number density.

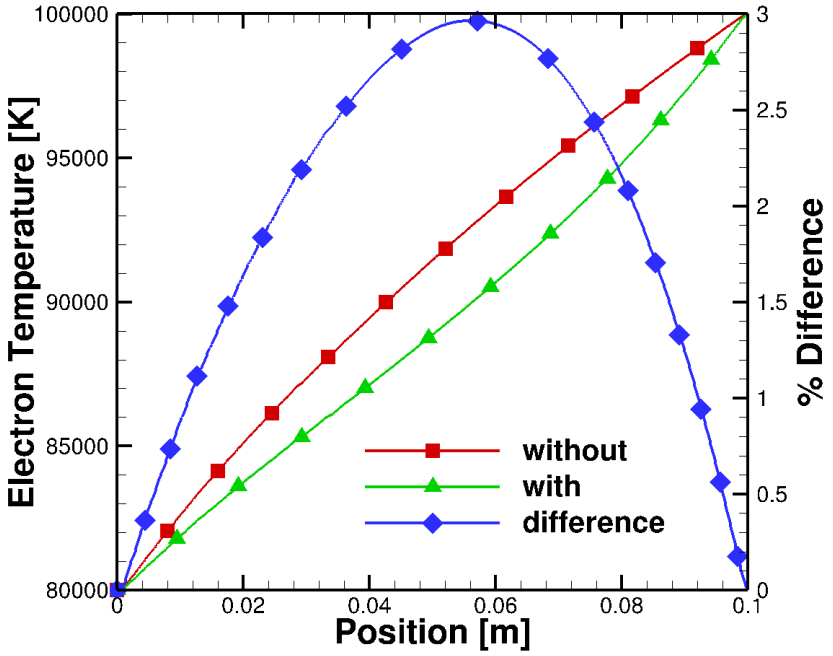

Figure 3.6: Comparison of electron temperature with and without ionization.

The thruster center is located at ($x = 0$ m, $y = 0$ m, $z = 0.1875$ m). In order to show that the implemented specular wall boundaries are working correctly, we compared a simulation with all outflow boundaries simulation in which the thruster center is located at ($x = 0.5$ m, $x = 0.5$ m, $z = 0.1875$ m). The thruster exit condition used in these simulation are given in Table 4.1. A 3D domain view of the Xe^+ ion number density contour plot for the outflow wall boundary simulation is given in Fig. 3.7b. These two simulations are called quarter thruster simulation and full thruster simulation in the rest of the paper. Quarter and full thruster simulations ran until 40000 timesteps to fill the domain particles and at the 40000^{th} timestep collisions and the electric field were turned on when collisions and the electric field acceleration were modeled. Sampling was done for 2000 additional timesteps. In Fig. 3.8 number density and axial velocity comparison contour plots for both simulations are given for neutral and ions species. In this first set of simulations, there were no MEX and CEX collisions between particles and the electric field acceleration was not applied to charged species. As can be seen from the contour plots in Fig. 3.8 agreement between the quarter and the full thruster simulation is perfect. In the second set of simulations for specular wall boundary

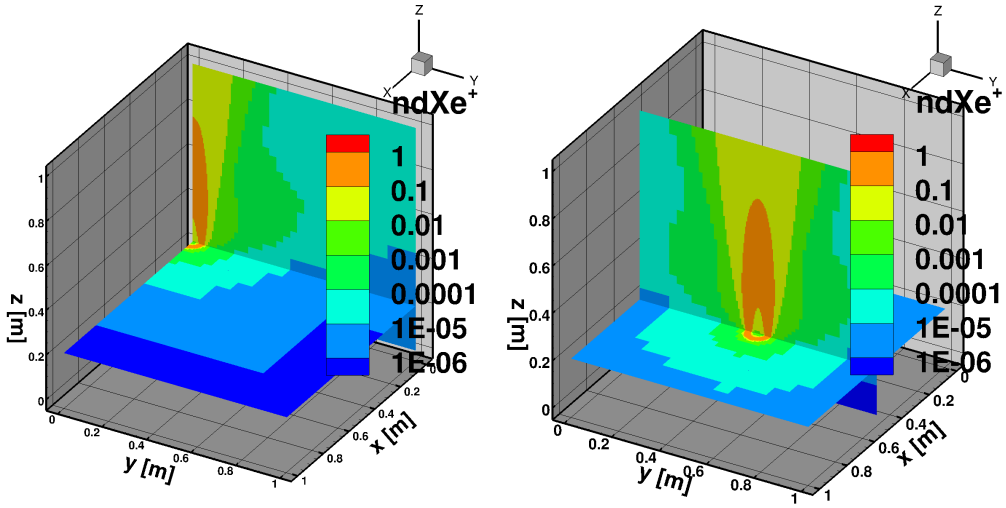

a) Quarter Thruster Simulation **b) Full Thruster Simulation**

Figure 3.7: Number density of Xe^+ comparisons in 3D domain view.

verification, both collisions and electric field acceleration are included in the simulation and number density and axial velocity contour plots are given in Fig. 3.9. As can be seen, neutral and ion number density and axial velocity of species show good agreement. Results for this test case can be improved increasing the number of samples and noise will be removed. Finally, in Fig. 3.10 electric potential contour plots are given, which is calculated using a polytropic model (Eq. 2.13) for plasma potential. Plasma potential shows a good agreement between the quarter and the full thruster simulations. Thus, it is concluded that implemented specular wall boundaries work well and full thruster modeling is not necessary for this work.

3.6 Domain size study for the electron fluid approach

In this section, three different domain sizes at space conditions are simulated using the electron fluid approach and compared to show the effect of domain size on our simulations. For the plasma potential Eq. 2.22 and for electron temperature Eq. 2.30 are solved. Boyd [5] noted that for the SPT-100 thruster at space conditions electron impact ionization is small due to the low electron temperatures and he also concluded that electron thermal conductivity is the primary property that affects the electron temperature.

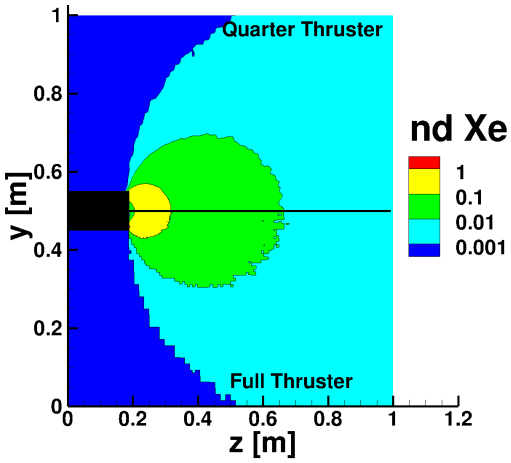

a) Number Density Xe normalized with $5.76 \times 10^{17}/m3$

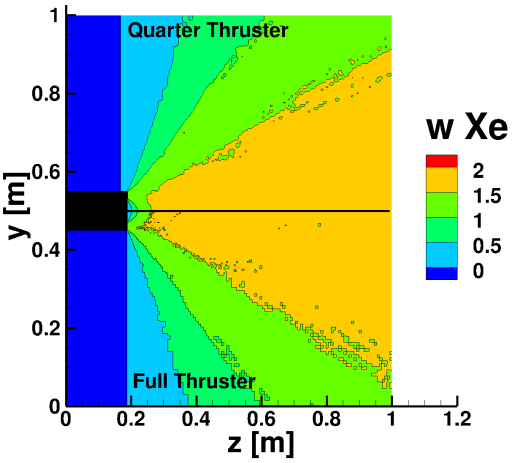

b) Axial Velocity Xe normalized with $325m/s$

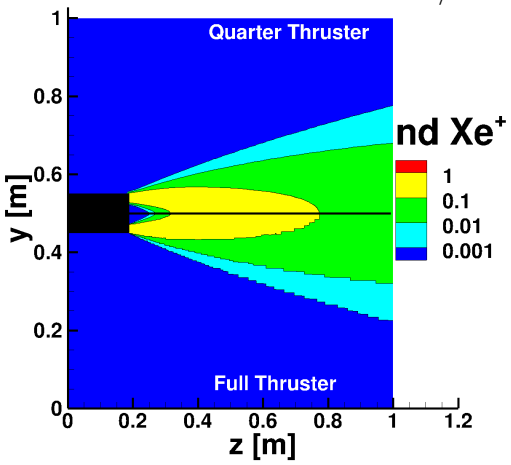

c) Number Density Xe^{+} normalized with $2.54 \times 10^{17}/m3$

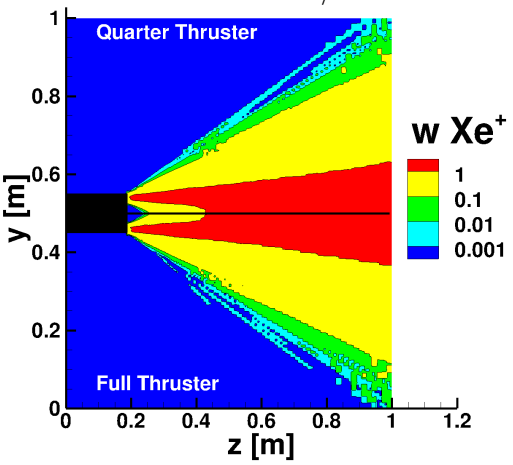

d) Axial Velocity Xe^{+} normalized with $16800m/s$

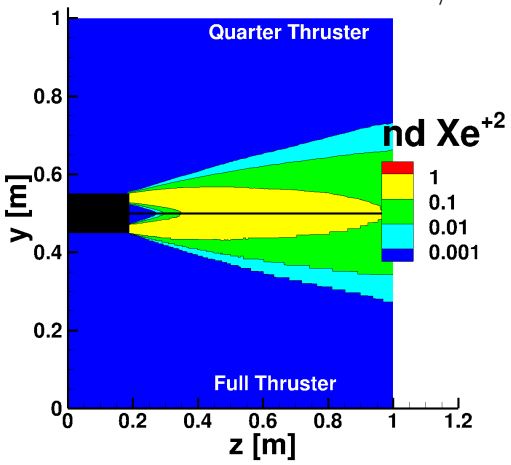

e) Number Density Xe^{+2} normalized with $0.28 \times 10^{17}/m3$

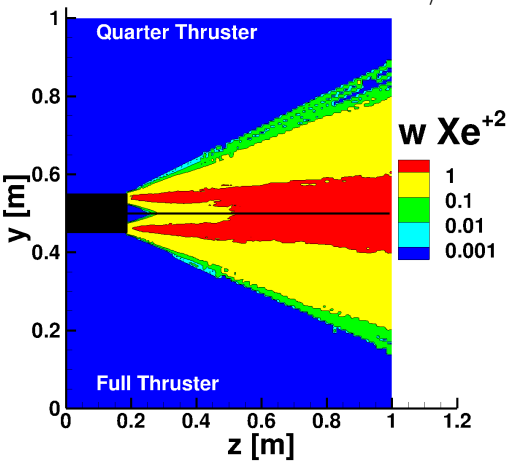

f) Axial Velocity Xe^{+2} normalized with $23800m/s$

Figure 3.8: Number density and axial velocity without collisions and electric field acceleration.

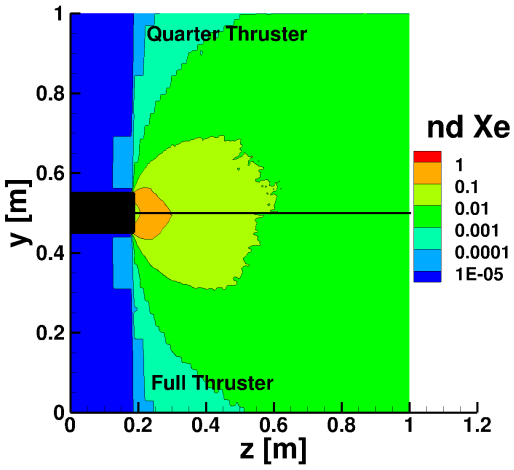

a) Number density Xe normalized with $5.76 \times 10^{17}/m3$

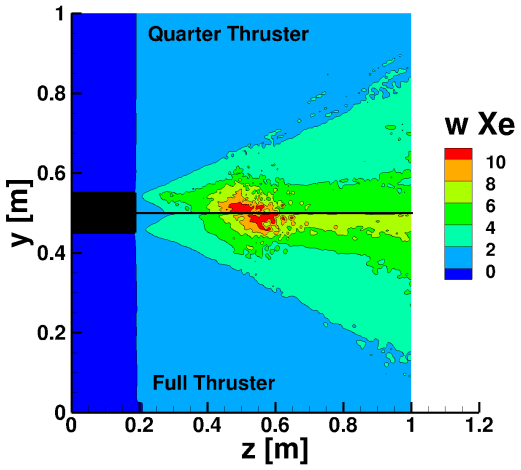

b) Axial Velocity Xe normalized with $325m/s$

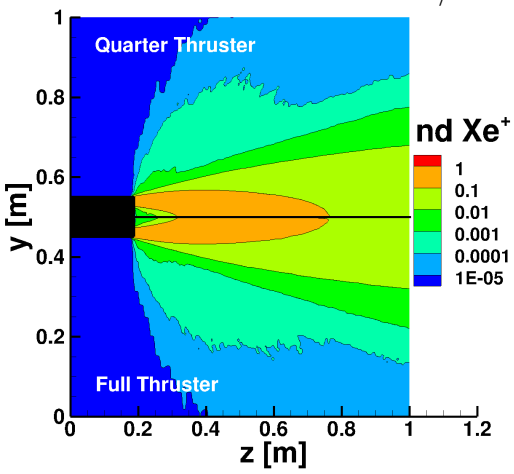

c) Number Density Xe^{+} normalized with $2.54 \times 10^{17}/m3$

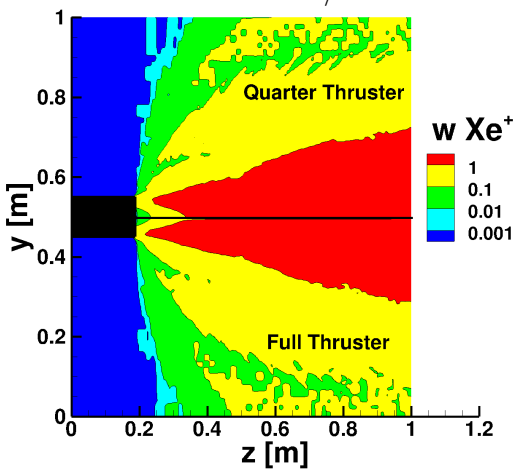

d) Axial Velocity Xe^{+} normalized with $16800m/s$

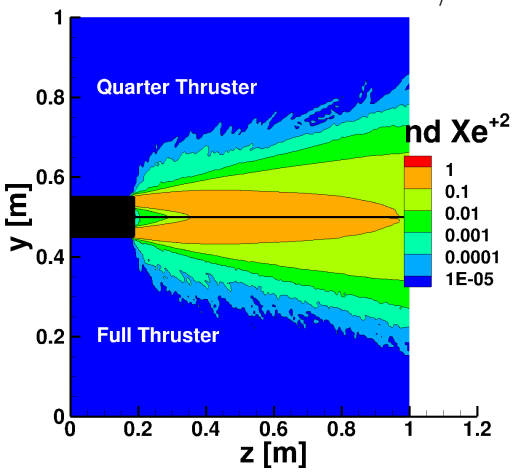

e) Number Density Xe^{+2} normalized with $0.28 \times 10^{17}/m3$

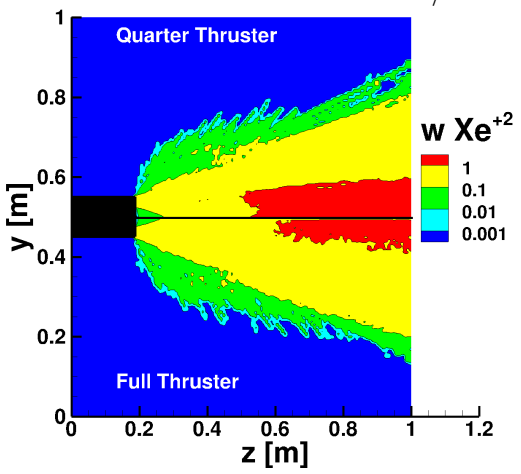

f) Axial Velocity Xe^{+2} normalized with $23800m/s$

Figure 3.9: Number density and axial velocity with collisions and electric field acceleration.

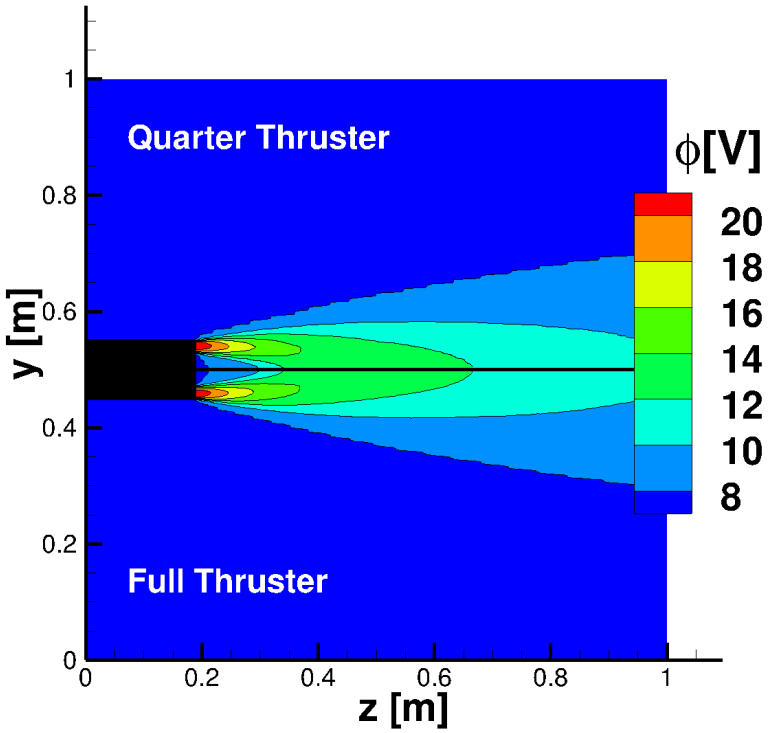

Figure 3.10: Plasma potential comparison of quarter and full thruster.

Thus, in our simulations, we neglected ionization and set the right-hand side of Eq. 2.30 to zero.

Simulations performed for a quarter thruster and two boundary walls at $x = 0$ m and $y = 0$ m are set to specular and rest of the boundary walls are set to outflow. The thruster center is located at $x = 0$ m, $y = 0$ m, $z = 0.1875$ m. The Poisson solver boundary conditions for space are also required at the edges of the domain. The electron fluid equations (Eqs. 2.16, 2.22, 2.30) require Dirichlet or Neumann boundary conditions defined at domain edges. The gradient of the plasma potential at all the boundaries was set to zero, except at $x = x_{max}$ and $y = y_{max}$ which were set to -5 V [5]. Similarly, the electron temperature gradient was set to zero at all boundaries, except at $x = x_{max}$ and $y = y_{max}$ which were set to 0.2 eV [5]. The thruster wall potential was chosen as 10 V, and, along the thruster walls, a fixed electron temperature of 1 eV and at the thruster exit an electron temperature of 4 eV were set.

The simulations were run for 96,000 timesteps. Free plume expansion is done until the 60,000 timestep and then the DSMC and PIC calculations

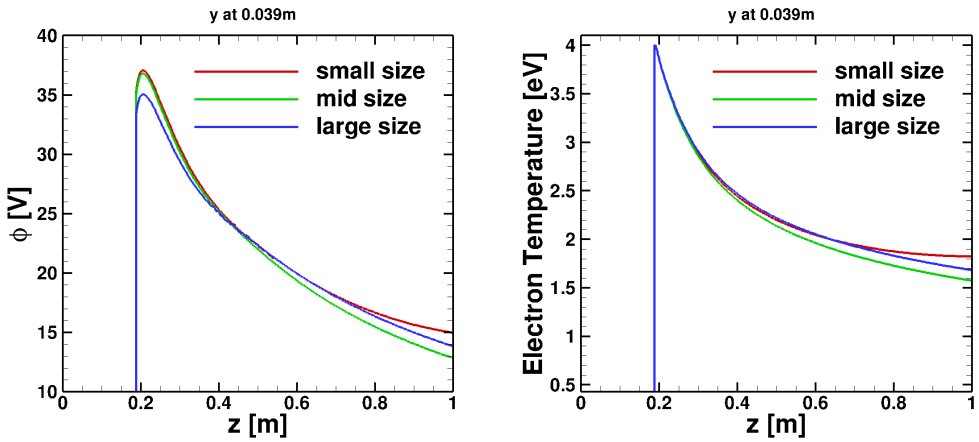

a) ϕ comparison y at 0.039m b) Te comparison y at 0.039m

Figure 3.11: Plasma potential and electron temperature line plots y at 0.039m for three different sizes of domains.

are started and both DSMC and PIC octrees were regenerated 5 times until sampling started at the 65,000 timestep. Thruster exit conditions used in this study are given in Table. 4.1. We have modeled three different domain sizes. The first one is a 1x1x1 m^3 domain referred to as a small-size domain, the second one is 2x2x2 m^3 domain referred to as a mid-size domain and the third one is 4x4x4 m^3 domain referred to as a large-size domain. The effect of changing domain size on plasma potential and electron temperature can be seen in Fig. 3.11a and Fig. 3.11b respectively, which are probed at the location with maximum mass flux, i.e. ($y = 0.039$ m), along the plume axis. It can be seen that plasma potential and electron temperature values are close to each other for all domain sizes. The largest difference for the plasma potential between different domains is 10% and for electron temperature, it is 5%.

It has been observed that neutrals and beam ions show similar spatial distributions the three domain sizes. However, It was observed that the only charge exchange ion spatial distribution is different between the small and mid-size and large size domains, but the CEX ions spatial distribution are similar between mid and large size domain. Thus in chapter 5, we reported results for the mid-size domain.

Chapter 4

Simulation of SPT-100 Thruster plume with Boltzmann and polytropic models

4.1 Thruster Exit and Boundary Conditions

The thruster exit conditions used are similar to VanGilder [1] for plume simulations of a SPT-100 Hall thruster. Number density, axial velocity and temperatures of the species at the thruster exit are given in Table 4.1. Since there is a large difference between the ion and neutral axial velocities, use of the same time step for both species would be inefficient. Therefore, a particle weighting algorithm with a species specified time-step is used [21]. The species weights and time-steps used in this work are provided in Table 4.1. For the Xe neutral particles, a Gaussian distribution with uniform bulk velocity is assumed and the thermal component of velocity is sampled from a half-Maxwellian distribution. For the Xe^{+} and Xe^{+2} ions, a Gaussian particle distribution at the exit is assumed. Unlike the neutral particles, it is assumed that the ions leave the thruster with a divergence angle (θ) which is a function of r, as given in Eq. (4.1).

$$\theta(r) = 2\theta_m \frac{r - \bar{r}}{r_{out} - r_{in}} \tag{4.1}$$

where $\bar{r} = \frac{1}{2}(r_{out} + r_{in})$ is the position halfway between the inner (r_{in}) and the outer (r_{out}) part of the annulus, with a thermal velocity sampled from a Half-Maxwellian distribution.The parameters used in the simulations are presented in Table 4.2. The simulation domain is a $1m^3$ cube shape domain and all walls are assumed as outflow boundary condition. Side and front views of the computational domain are given in the Figure 4.1 with the thruster exit, is located at $(x, y, z) = (0.5, 0.5, 0.1875$ m). In the following figures in this chapter, the dimensions are normalized by thruster diameter ($D = 0.1$ m).

The simulations were run for 300,000 timesteps. Free plume expansion

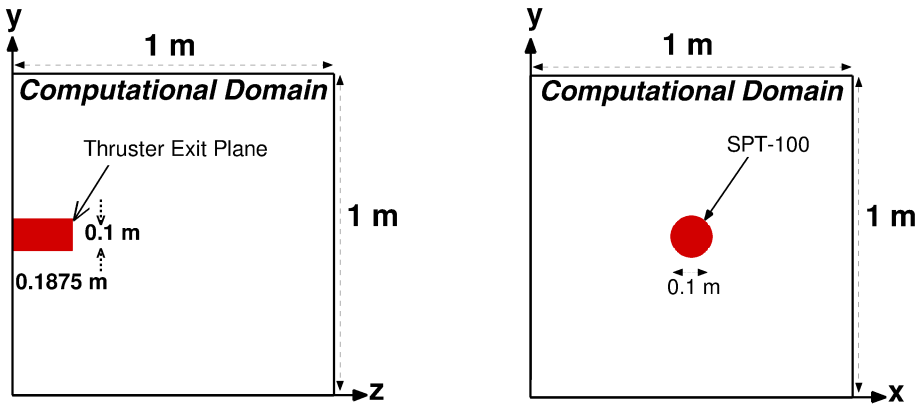

a) y-z plane **b) x-y plane**

Figure 4.1: Computational domain.

is done until 60,000$^{\text{th}}$ timestep and then the DSMC and PIC calculations are started and both C-octree and E-octree were regenerated 3 times until sampling started at 100,000$^{\text{th}}$ timestep.

Table 4.1: Thruster exit plume conditions.

	Xe	**Xe^{+}**	**Xe^{+2}**
n($\times 10^{17}$ m^{-3})	5.76	2.54	0.28
U(m/s)	325	16800	23800
T(K)	1000	46418	46418
θ_m(deg)	0	10	10
FNUM	1.5×10^8	1.5×10^8	1.5×10^8
Weight	1.0	0.2	0.025
Timestep Δt [s]	2.5×10^{-7}	5×10^{-8}	6.25×10^{-9}

Table 4.2: Simulation parameters.

Parameter	**Value**
r_{out}(m)	0.05
r_{in}(m)	0.028
Thruster Lenght (m)	0.1875
ϕ_o (V)	10
n_o (m^{-3})	6.5×10^{15}
T$_e$(eV)	3

4.2 Results and Discussion

Electric potential comparisons of the polytropic (adiabatic) and Boltzmann (isothermal) models are given in Figure 4.2. The polytropic model predicts higher electric potential values close to the thruster exit. In addition to that, the Boltzmann model predicts a longer and radially confined electric potential. Unlike the Boltzmann model, the polytropic model predicts a shorter and radially expanded potential profile. The reason for the differences between the two models is that the polytropic model considers electron cooling, as electrons and ions expand away from the thruster.

The number density distributions of neutrals and ions are given in Figure 4.3 for both Polytropic and Boltzmann models. Neutral number density distributions show small differences as can be seen in Figure 4.3a. Singly and doubly charged ion distributions, given in Figure 4.3b and 4.3c for both models, show spatial trends similar to the electric potential distribution i.e., a radially expanded profile for the polytropic model and radially confined profile for the Boltzmann model. Singly and doubly charge exchanged ions number density distributions follow the same distribution profiles as beam ions (see Figures 4.3d, 4.3e).

Axial velocity (Z-velocity) profiles of the neutrals and the ions are given in Figure 4.4 for both the polytropic and Boltzmann models. Both models predict similar axial velocity profiles for the neutrals in the near field, but, in the far field, the Boltzmann model predicts velocities as high as 7000 m/s close to the thruster axis. The number of CEX ions created closer to the thruster axis is higher in the Boltzmann model in the near field (refer to Figs. 4.3d and 4.3e). Similarly, fast neutrals are created in the same regions as the CEX ions. Since fast neutrals have large axial velocity they will travel straight instead of expanding radially. Thus, the average neutral velocity in the far field close to the thruster axis will increase, whereas, the neutral number density (Fig. 4.3a) is low. Singly and doubly charged ion velocity profiles show again similar profile as electric potential profiles and radially expanded profile for the polytropic model and radially confined for the Boltzmann model as given in the Figure 4.4b and 4.4c. CEX ions velocity profiles show similar profiles as the electric potential, but at the far field, both CEX ion velocity profile for the Boltzmann model shows higher velocities close to the thruster axis. This is because larger electric potential

drop, accelerates ions more in the Boltzmann model. However, since there are very few computational macro particles represents CEX ions, velocity profiles of the $Xe^{+}{}_{CEX}$ and $Xe^{+2}{}_{CEX}$ are noisy, as can be seen in Fig. 4.4d and Fig. 4.4e.

Near field, current density measurements of SPT-100 Hall thruster plume were made previously by Kim [2] at three different axial locations. Following the work of Kim [2], VanGilder [1] simulated an SPT-100 Hall thruster plume using a 2D axisymmetric DSMC/PIC simulation. In order to see the effect of the electron temperature gradient VanGilder [1] compared a variable electron temperature model using a similar relation to Eq. 2.13 and a constant electron temperature model, described in section 2.1. Similarly, in this work, the Boltzmann model (Eq. 2.11) corresponds to a constant electron temperature or isothermal expansion and the polytropic model (Eq. 2.13) corresponds to variable electron temperature or adiabatic expansion. Unlike the previous studies [6, 20], we chose a lower adiabatic exponent value based on measurements of Giono et. al. [28]. Validation of this study was done by comparing the current density results from the previous measurements and simulations, as shown in Figure 4.5. Figure 4.5a shows that at 10 mm from the thruster exit the current density values are close regardless of the model used. At 50 mm (Fig. 4.5b) and 100 mm (Fig. 4.5c) downstream of the thruster, the effect of the electron temperature gradient becomes more significant, and the polytropic (adiabatic expansion) model predicts the experimental results better than the Boltzmann (isothermal expansion) model. The current density agreement in this study at 50 and 100 mm from the thruster exit is better than the previous studies [1]. This is because we assumed a Maxwellian distribution thermal velocity for ions and we used an adiabatic exponent value smaller than the theoretical adiabatic exponent value. However, at the thruster axis ($y/D = 5$) the current density value peaks at 50 and 100 mm from the thruster exit. This peak could not be captured, in this study and in Ref. [1]. As explained by VanGilder [1], this peak at thruster centerline could be due to the effect of magnetic field on the electrons in the near field. Thus, it is required to use more detailed models than the Boltzmann or the polytropic models for the simulation of Hall thruster plumes. In section 5.3, comparison of the electron fluid model implemented in CHAOS is given together with the Boltzmann and the polytropic model results.

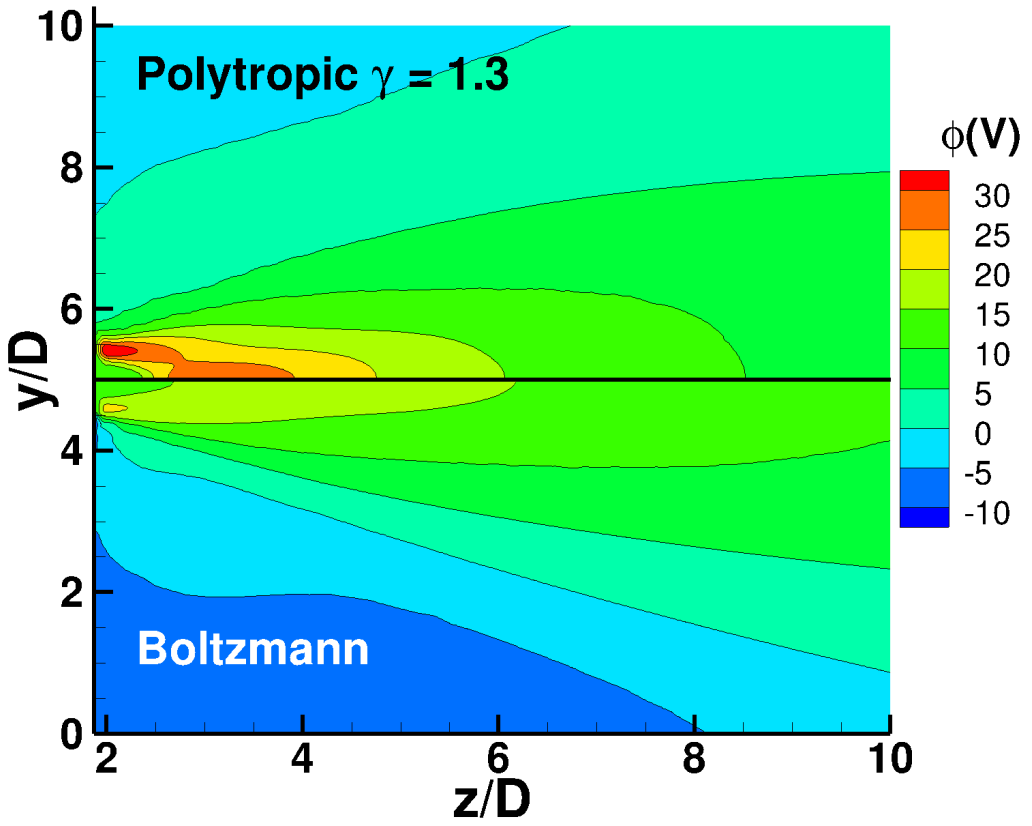

Figure 4.2: Comparison of plasma potential between polytropic and Boltzmann model.

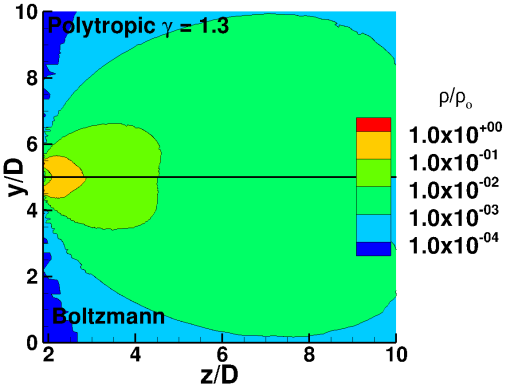

a) Number density Xe normalized with $5.76 \times 10^{17}/m3$

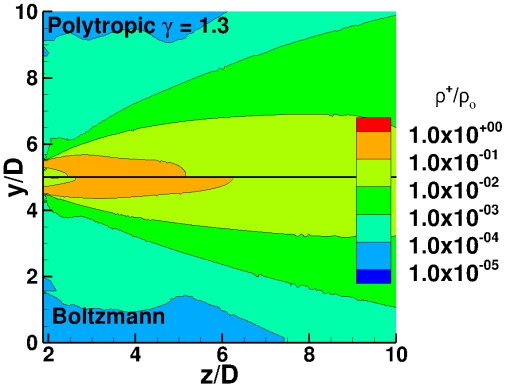

b)Number Density Xe^{+} normalized with $2.54 \times 10^{17}/m3$

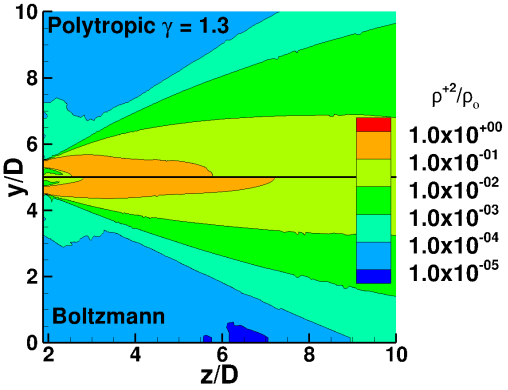

c) Number Density Xe^{+2} normalized with $0.28 \times 10^{17}/m3$

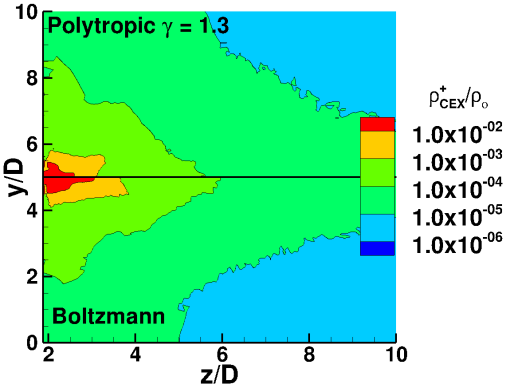

d) Number Density $Xe^{+}{}_{CEX}$ normalized with $2.54 \times 10^{17}/m3$

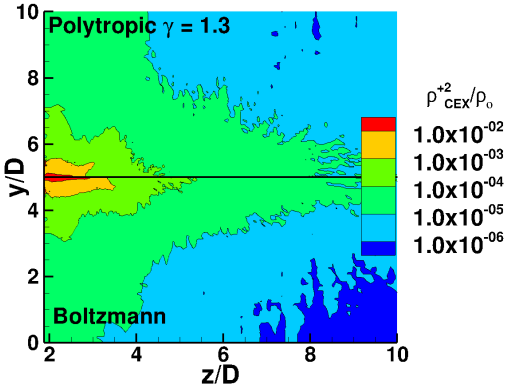

e) Number Density $Xe^{+}2_{CEX}$ normalized with $0.28 \times 10^{17}/m3$

Figure 4.3: Comparison of number density of species between polytropic and Boltzmann model.

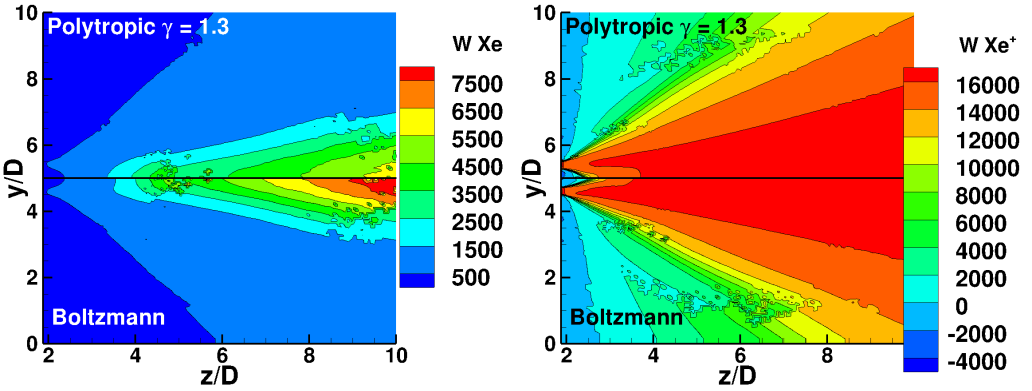

a) Axial Velocity Xe (m/s)

b) Axial Velocity Xe^{+} (m/s)

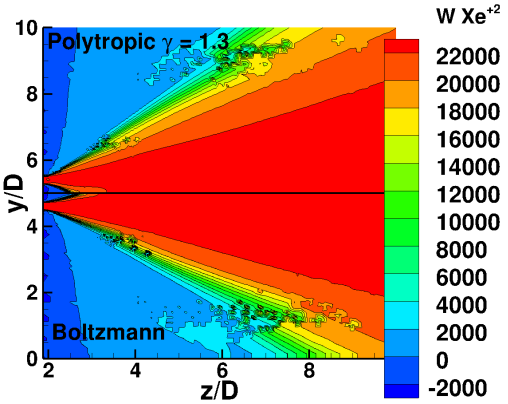

c) Axial Velocity Xe^{+2} (m/s)

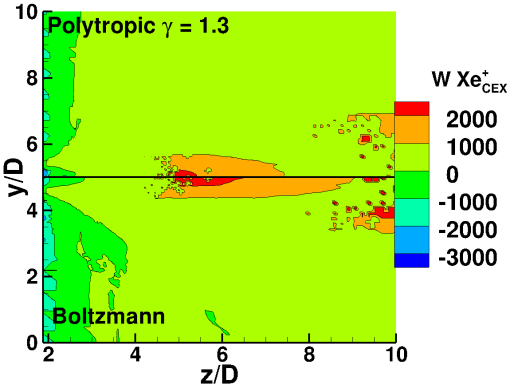

d) Axial Velocity $Xe^{+}{}_{CEX}$ (m/s)

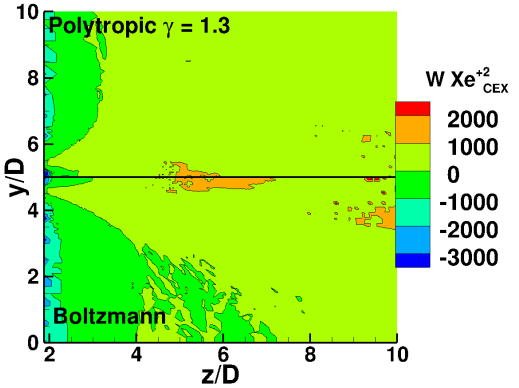

e) $Xe^{+2}{}_{CEX}$ (m/s)

Figure 4.4: Comparison of axial velocity of species between polytropic and Boltzmann model.

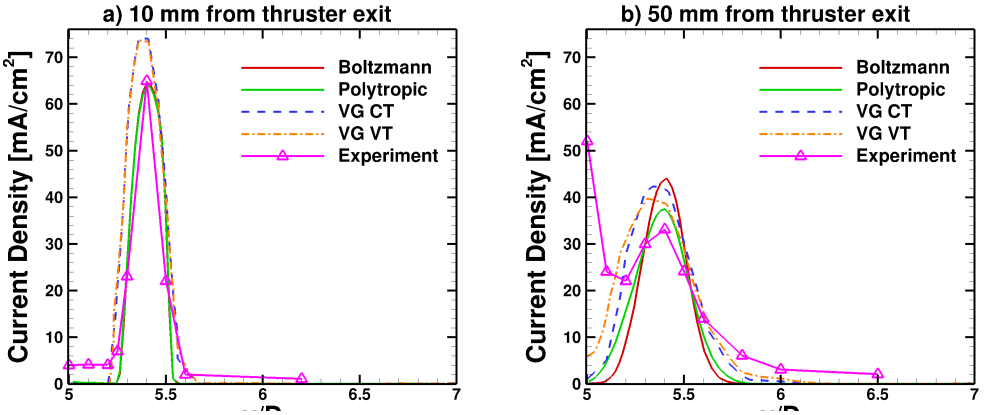

a) 10mm from thruster exit b) 50mm from thruster exit

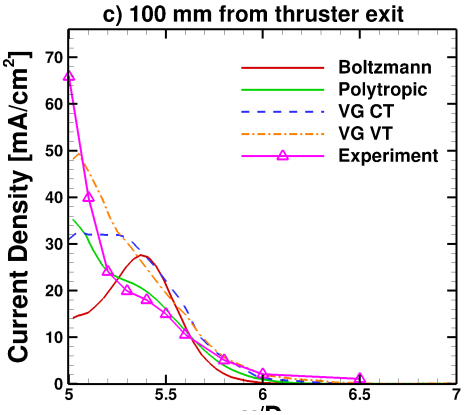

c) 100mm from thruster exit

Figure 4.5: Comparisons of current density from Boltzmann and polytropic model, contant (VG CT) and variable (VG VT) electron temperature simulation by VanGilder [1], experiment by Kim [2].

Chapter 5

Simulation of an SPT-100 Thruster plume with electron fluid and polytropic models in the presence of a solar panel

5.1 Thruster Exit and Boundary Conditions

The thruster exit conditions used are similar to VanGilder [1] for plume simulations of a SPT-100 Hall thruster. Number density, axial velocity and temperatures of the species at the thruster exit are given in Table 5.1. Since there is a large difference between the ion and neutral axial velocities, use of the same time step for both species would be inefficient. Therefore, a particle weighting algorithm with a species specified time-step is used [21]. The species weights and time-steps used in this work are provided in Table 5.1. For the Xe neutral particles, a Gaussian distribution with uniform bulk velocity is assumed and the thermal component of velocity is sampled from a half-Maxwellian distribution. For the Xe^{+} and Xe^{+2} ions, a Gaussian particle distribution at the exit is assumed. Unlike the neutral particles, it is assumed that the ions leave the thruster with a divergence angle (θ) which is a function of r, as given,

$$\theta(r) = 2\theta_m \frac{r - \bar{r}}{r_{out} - r_{in}} \tag{5.1}$$

where $\bar{r} = \frac{1}{2}(r_{out} + r_{in})$ is the position halfway between the inner (r_{in}) and the outer (r_{out}) part of the annulus, with a thermal velocity sampled from a Half-Maxwellian distribution. The parameters used in the simulations are presented in Table 5.2. The simulation domain is a 2m×2m×2m cubic shaped domain. Since for the conditions simulated in this work the problem of interest is symmetric, simulations are performed for a quarter of the thruster and a specular boundary condition is applied at the two boundary walls at $x = 0$ m and $y = 0$ m. The rest of the boundaries are chosen as outflow. In the side and front views of Fig. 5.1, the computational domain is shown with the thruster exit located at ($x = 0$ m, $y = 0$ m, $z = 0.1875$ m). It was

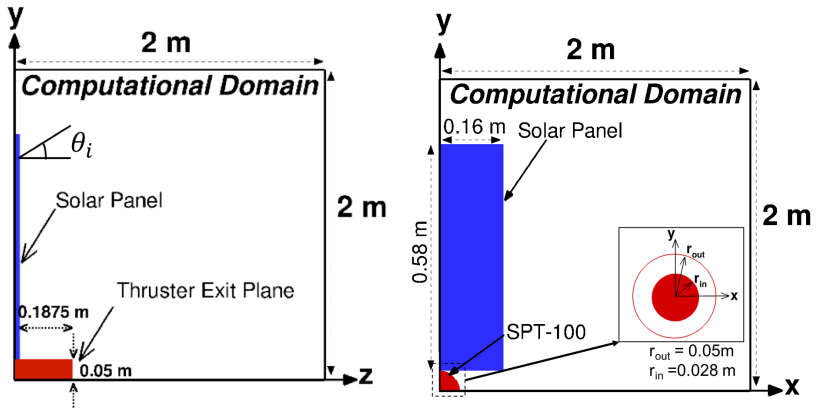

a) y-z plane **b) x-y plane**

Figure 5.1: Computational domain.

observed that very few particles were impacting the thruster walls, so gas surface interactions have no effect on the general structure of the highly diffuse flowfield. Thus, particles impacting to the thruster walls are removed from the domain. However, for the simulations with solar panel, a gas surface interaction algorithm has to be implemented. Since the solar panel has an electric potential, it creates an electric field and attracts ions and some of them impact to the solar panel surface [11]. A diffuse boundary condition is applied to solar panel surface. Impacted ions are neutralized and a new neutral is created and reflected with full accommodation at a solar panel wall temperature at 500 K. Similarly, if an neutral collides with the solar panel wall it is reflected with full accommodation at solar panel wall temperature [39].

For space conditions, unlike the vacuum chamber, there is no finite back pressure and the ionization process due to electron-neutral collisions is small. Also, as explained by Boyd [5] for the SPT-100 thruster electron impact ionization is small due to the low electron temperatures for space conditions making the electron thermal conductivity is the primary property that affects the electron temperature. Although, in our simulations similar to previous studies [5], we have not seen the effect of ionization, we did not neglect the ionization term in Eq. 2.30.

The Poisson solver boundary conditions for space are also required at the edges of the domain. The electron fluid equations (Eqs. 2.22 and 2.30) require Dirichlet or Neumann boundary conditions defined at domain edges.

The gradient of the plasma potential at all the boundaries was set to zero, except at $x = x_{max}$ and $y = y_{max}$ which were plasma potential set to -5 V [5]. Similarly, the electron temperature gradient was set to zero at all boundaries, except at $x = x_{max}$ and $y = y_{max}$ which were set to an electron temperature corresponding to 0.2 eV [5]. The thruster wall potential was chosen as 0 V a fixed electron temperature of 1 eV. At the thruster exit a plasma potential was chosen as 20V and an electron temperature of 4 eV were set.

The Poisson boundary conditions for the solar panel has to be defined as well. Solar panels consists of many solar cells or circuits and in each circuit the electric potential increases. Since it is not computationally feasible to simulate the whole solar panel, only one circuit of the solar panel was simulated. As a reference ADEOS-II [40] satellite was chosen, and it was assumed thruster is grounded at 0 V and it was assumed only a single array circuit linearly decreasing potential from 0 V to -40 V along the solar panel. For the electron temperature equation (Eq. 2.30), electron temperature on the solar panel has to be defined. Assuming that in the backflow region the energy of electrons is small, a constant electron temperature of 0.8 eV was used.

Similar to previous studies [3, 39] for polytropic model simulations, we decompose the imposed solar panel potential and plasma potential. In order to compute the imposed solar panel potential in the domain we solved Laplace equation,

$$\nabla^2 \phi_{ext} = 0 \tag{5.2}$$

when the E-octree is regenerated and superimposed the plasma potential ϕ_p computed using the Eq. 2.13 to compute the total electric potential,

$$\phi_{total} = \phi_p + \phi_{ext} \tag{5.3}$$

In this study the plasma sheath is neglected because it is small compared to cell size. Since the backflow typical plasma number densities are around $2 \times 10^{12} \mathrm{m}^{-3}$. Assuming cold electrons in the backflow region of $T_e = 0.05\mathrm{eV}$ the local Debye length will be 1mm. As a rule of thumb we can assume the plasma sheath is 4 times the Debye length i.e. 4mm [41]. In the backflow, the cell length is around 3cm so that the quasi-neutrality assumption is satisfied. Thus, the cell size is an order of magnitude larger than plasma

sheath thickness. Furthermore, the potential drop in plasma sheath can be calculated using thin sheath approximation,

$$\phi_s = -T_e \ln\left(\sqrt{\frac{T_i m_e}{T_e m_i}}\right) \tag{5.4}$$

where, T_e and T_i electron and ion temperature in electron volts and m_e and m_i are electron and ion mass [42]. Choosing an ion temperature as 0.05 eV, we can compute the potential drop in the sheath as 0.3 V. This potential drop is negligible considering that total potenital drop an ion experience is around 60 V [43], between thruster exit and solar panel as can be seen in Fig. 5.9. Also as discussed in Sec. 5.7, for the computed ion energies in the vicinity of the solar panel, the potential drop in the sheath would not cause an important effect on sputtering characteristics of the solar panel. Thus, in this study the plasma sheath is not simulated, because of its is small thickness and low potential drop.

The simulations were run for 300,000 timesteps. Free plume expansion is done until the 60,000$^{\text{th}}$ timestep and then the DSMC and PIC calculations are started and both the C-octree and the E-octree were regenerated 5 times until sampling started at the 100,000$^{\text{th}}$ timestep.

Table 5.1: Thruster exit plume conditions.

	Xe	**Xe$^+$**	**Xe^{+2}**
n($\times 10^{17}$ m^{-3})	5.76	2.54	0.28
U(m/s)	325	17800	25800
T(K)	1000	11605	11605
θ_m(deg)	0	10	10
FNUM	1.5×10^8	1.5×10^8	1.5×10^8
Weight	1.0	0.2	0.025
Timestep Δt [s]	2.5×10^{-7}	5×10^{-8}	6.25×10^{-9}

5.2 Surface Sputtering Model

CEX ions created at the thruster exit, move to the backflow region due to the attraction of solar panels. One of the sputtering model in the literature is the Eckstein sputtering yield model, which is mostly based on experiments.

Table 5.2: Simulation parameters.

Parameter	**Value**
r_{out}(m)	0.05
r_{in}(m)	0.028
Thruster Lenght (m)	0.1875
ϕ_o (V)	20
n_o (m^{-3})	6.5×10^{15}
T_e(eV)	3.5

Unlike the Eckstein equation which depends on three parameters for proper curve fitting, the Bohdansky equation depends on only one scaling factor [44]. Bohdansky equation [45] is given by,

$$Y\left(E_i\right) = Q s_n\left(\varepsilon\right)\left(1 - \left(\frac{E_{th}}{E_i}\right)^{2/3}\right)\left(1 - \left(\frac{E_{th}}{E_i}\right)\right)^2 \tag{5.5}$$

where, E_i is incidence energy of ions, $s_n(\epsilon)$ is nuclear stopping power of the interaction, ϵ is the reduced ion energy, Q is scaling factor and E_{th} threshold energy, which depends on surface and projectile material properties. For xenon aluminum pair, $Q = 19.36$ and $E_{th} = 28.67$ eV. In this study, the xenon aluminum pair is used in the sputtering yield calculations because aluminum has a lower sputtering yield than glass.

The importance of ion incidence angle on sputtering yield was shown by Yamamura [46] and effect of ion incidence angle can be added by using a prefactor. For different angles of incidence, the relative sputtering yield can be computed by,

$$x = 1/\cos\left(\theta_i\right) \tag{5.6}$$

$$\Sigma = f\cos\left(\theta_{opt}\right) \tag{5.7}$$

$$\frac{Y\left(E,\theta_i\right)}{Y\left(E,0\right)} = x^f e^{\Sigma(x-1)} \tag{5.8}$$

where the ratio of $Y(E,\theta_i)/Y(E,0)$ is the prefactor and $Y(E,\theta_i)$ is the sputtering yield at incidence angle of θ_i and $Y(E,0)$ is the sputtering yield at an incidence angle zero, i.e. normal to the surface. Incidence angle or angle of incidence θ_i is showed in Fig.5.1a and it the angle between particle

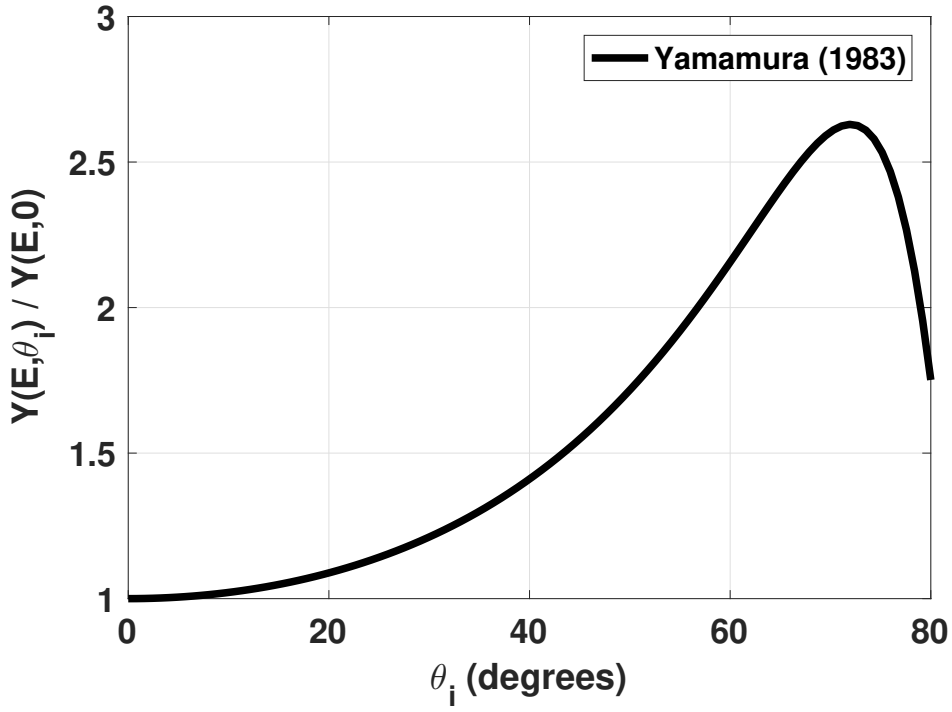

Figure 5.2: Angular variation of Yamamura prefactor.

incidence velocity vector and the solar panel normal. For the aluminium fit parameters $f = 2$ and $\theta_{opt} = 72.4°$, as calculated by Yamamura [46]. The prefactor changes between 0 and 2.6 for the cases of interest, as given in Fig. 5.2. Surface recession(m/s) rate can be calculated by,

$$S = \frac{f_{Xe_{ion}} Y\left(E, \theta_i\right)}{n_T} \tag{5.9}$$

where, $f_{Xe_{ion}}$ is the flux of ions incident at the surface ion per m^2 per second, $Y(E, \theta_i)$ is the sputtering yield in ion per atoms and n_T is the number density of the target element, i.e. for aluminum 6.08×10^{28}(atoms/m^3).

5.3 Current density comparisons

In this section, near field current density calculations of SPT-100 Hall thruster done by using the electron fluid, the polytropic and the Boltzmann model is compared with previous simulations [1] and measurements [2]. Thruster exit plume conditions used current density study are the same as the ones

given in Table 4.1. Boundary conditions used for the electron fluid model are the same as the ones described in section 5.1 but without the solar panel. Current density comparisons for the three electron models and previous simulations [1] and measurements [2] are given in Fig. 5.3, where polytropic and Boltzmann model results are from Fig. 4.5. At 10 mm from the thruster exit, current density values estimated by the three electron models used are same, as shown in Fig. 5.3a. This is because the thruster exit conditions are same for all three simulations. At 50 mm from the thruster exit, both the electron fluid and the Boltzmann model estimates higher current density values than the polytropic model and experimental measurements [2], as given in Fig. 5.3b. Finally, at 100 mm from the thruster exit, current density values estimated by the electron fluid and the Boltzmann model are given in Fig. 5.3c and both electron models estimated almost the same current density profile, except at the thruster centerline ($y = 0$ m) where current density value estimated by the electron fluid model is higher. Although the current density estimated by the polytropic model at 50 and 100 mm from the thruster exit is closer to the experimental measurements [2], for different thruster exit potential and electron temperatures using as an input for the electron fluid model, we might estimate better results. In addition to that as it is discussed in section 5.6 the electron fluid model estimates more gradual potential drop than the polytropic model so it might estimate ion distribution and energies better than the polytropic model outside the core plume region. However, for the current density comparison given in this section, the polytropic model shows better agreement than both the electron fluid and the Boltzmann model.

5.4 Ion energy distribution sensitivity study

In this section, sensitivity tests were done to see the effect of thruster exit plasma potential and thruster exit electron temperature on ion energy distributions outside the beam region at a high angular position. Ion energy distributions obtained for different conditions are compared with the ESA SMART 1 [3] mission ion energy distribution measurements. For this study the thruster exit and boundary conditions given in section 5.1 are used, except the thruster exit plume conditions. Thruster exit plume conditions used

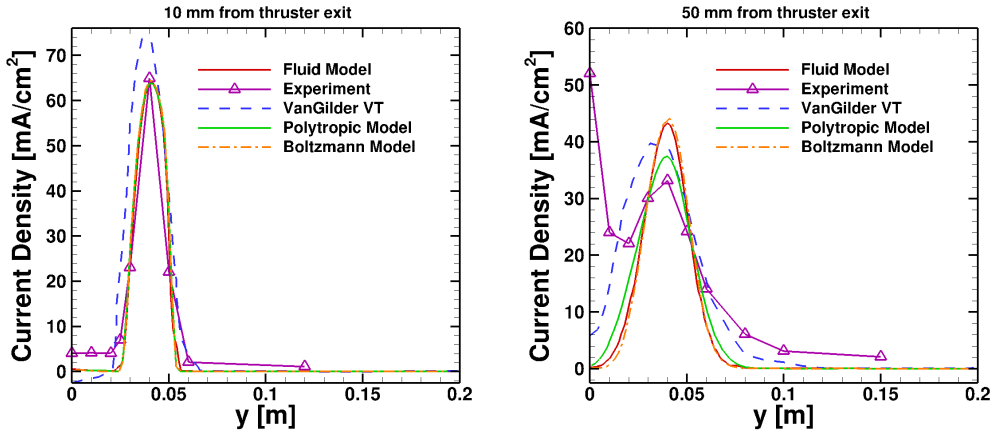

a) 10mm from thruster exit b) 50mm from thruster exit

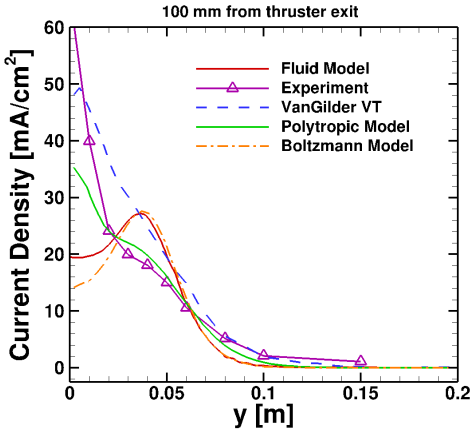

c) 100mm from thruster exit

Figure 5.3: Comparisons of current density from electron fluid, Boltzmann and polytropic model, contant (VG CT) and variable (VG VT) electron temperature simulation by VanGilder [1], experiment by Kim [2].

in sensitivity study are same as the ones given in Table 4.1.

In Fig. 5.4, normalized distribution of ion energy at 0.57 m and 85° are given for different thruster exit electron temperatures at constant 20 V thruster exit plasma potential. As can be seen from Fig. 5.4 the spread of the ion energy curve increases and the second peak width and height increases as the thruster exit electron temperature increases. The second peak width and height of the curve is more sensitive to the thruster exit electron temperature.

As a second test, the effect of thruster exit plasma potential, on the ion energy distribution is investigated. For a constant thruster exit electron temperature different thruster exit plasma potential simulation results of ion energy distributions are given in Fig. 5.5 with SMART 1 [3] measurement. As can be seen from Fig. 5.5, the width of the ion energy distribution is almost constant and is not affected by the thruster exit plasma potential. However, the peak of the ion energy distribution shifts to higher ion energies as the thruster exit plasma potential increases. Thus, the ion energy distribution spread depends on thruster exit electron temperature and the peak position depends on the thruster exit plasma potential.

5.5 Ion energy distribution comparison with experiments

In this section, the ion energy distribution obtained at different locations in the flow field are compared with space measurements and previous simulations. The first comparison of ion energy distribution at 3.8m from the thruster exit and 8° from the thruster centerline is given in Fig. 5.6. Express measurements [4] were taken in space and are reported as a bar graph with the center of the bar representing the measured data. The simulation of Boyd [5] is also given for comparison. Our simulation result shows good agreement with the Express measurements [4] and Boyd's [5] simulation. The width of the ion energy curve is around 50 for both simulations. The comparison shows that thruster exit conditions for ions are set properly.

In Fig. 5.7 the ion energy distribution at 1.4m from the thruster exit and 77° from the thruster centerline is compared with the Express data [4] and Boyd simulation [5]. At these high angles from the thruster centerline, low

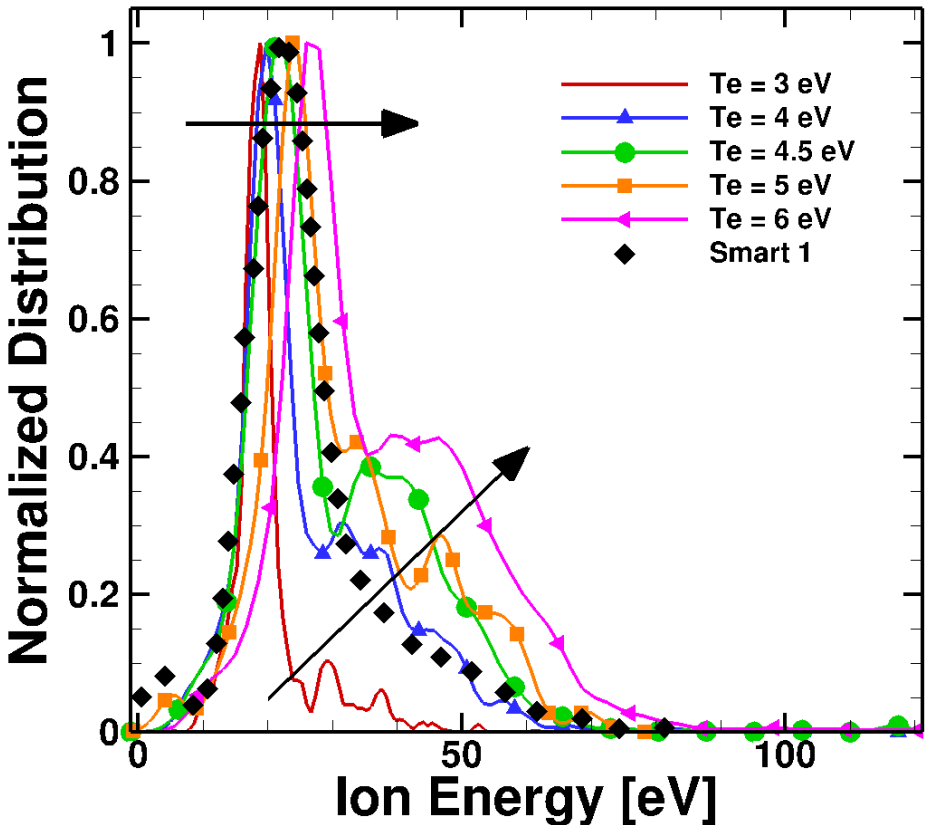

Figure 5.4: Effect of thruster exit electron temperature on ion energy distribution at 0.57 m 85° ($\phi_{exit} = 20$V) [3].

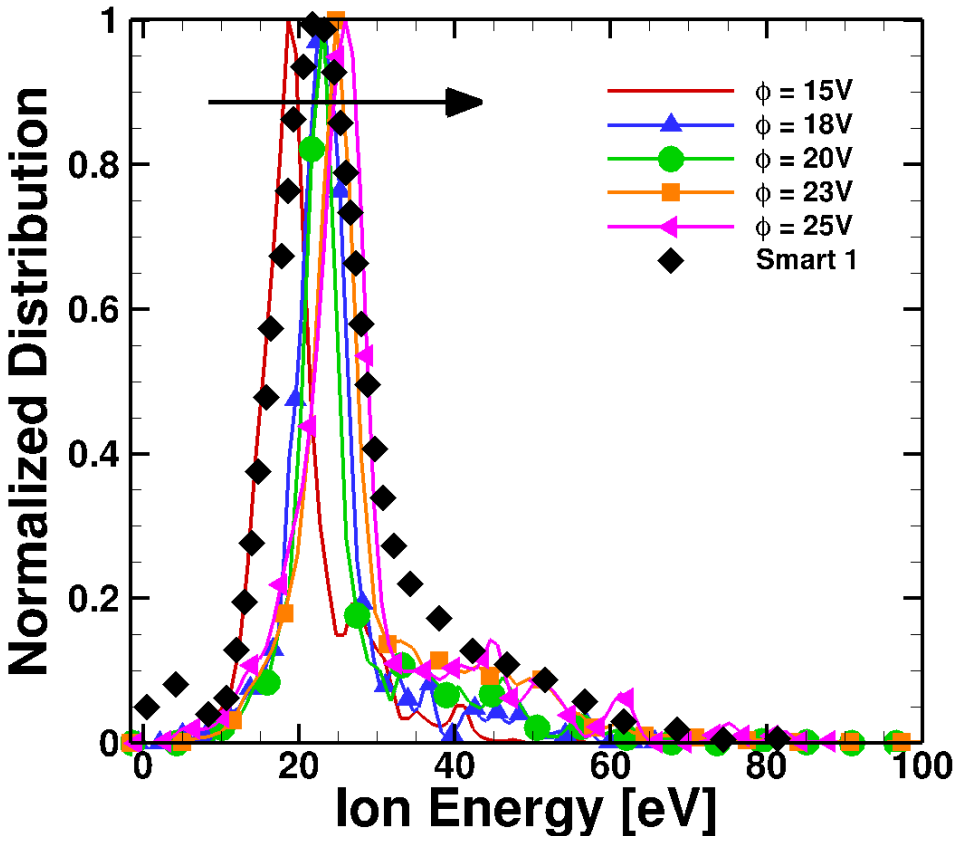

Figure 5.5: Effect of thruster exit plasma potential on ion energy distribution at 0.57 m 85° ($T_{exit} = 3$eV) [3].

energy ions are expected, but the Express data shows high ion energies with as much as 260 eV. Our simulation and simulation of Boyd could not capture these high energies. However, our simulation shows a good agreement with the simulation of Boyd [5] and Express data [4] at low ion energies.

Finally, in Fig. 5.8 the ion energy distribution at 0.57m from the thruster exit and 85° from the thruster centerline is compared with the SMART 1 data and the simulation of Tajmar [3]. Again, these high angles only CEX ions are expected and unlike the Express data at 77°, ion energy data of SMART 1 does not have ion energies as high as 260ev, but there are still some ions at energies in excess of 60 eV. The raw data of SMART 1 had to be shifted between 11-18.5 eV because the floating potential of the retarding potential analyzer (RPA) was not known. In their earlier study Tajmar et. al.[47] shifted the measured ion energy distribution by 18 eV to match with their simulation. Following this study, Boyd [5] simulated the flow field and showed a good match with shifted, postprocessed SMART 1 data presented in [47]. In their final work, Tajmar et. al. shifted the raw data of SMART 1 ion energy distribution by 22.5 V in order to match with their simulation [3]. There has not been any simulations following the revised SMART 1 data in the literature, other than simulation of Tajmar [3]. Our simulation could capture the ion energy peak but it poorly captured the width of the ion energy distribution. We have seen that in section 5.4, the width of the ion energy distribution depends on the thruster exit electron temperature. Choosing a higher thruster exit electron temperature might result in a better agreement with both SMART 1 data and simulation of Tajmar [3]. However, this will result in disagreements of ion energy distributions with the Express data given in Fig. 5.6-5.7. Considering the difficulties of ion energy measurements in space and uncertainties, our simulation show a reasonable agreement with both sets of measurements and previous simulations.

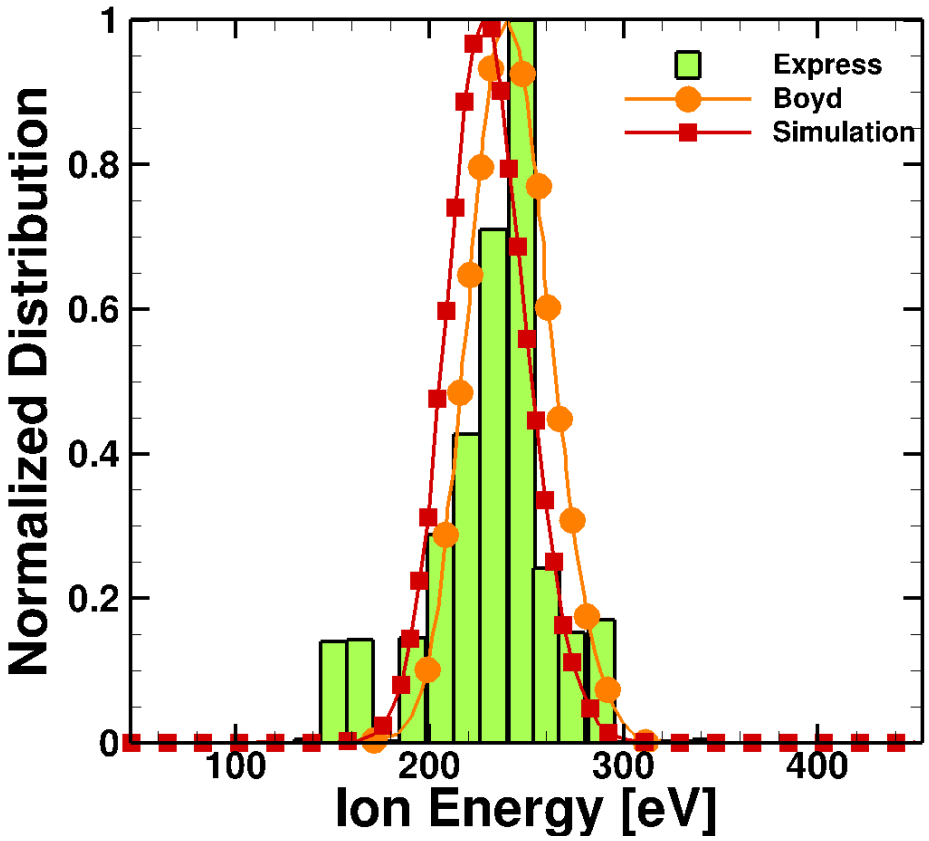

Figure 5.6: Comparison of ion energy distribution at 3.8m, 8° with Express [4], Boyd [5] and this work.

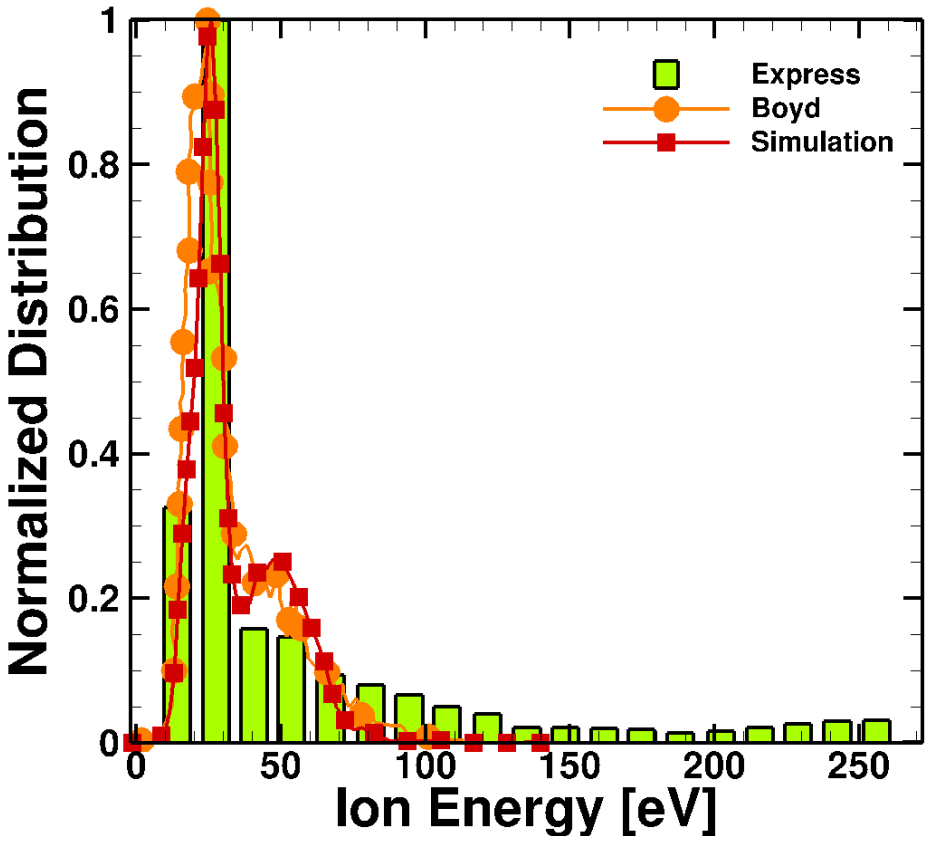

Figure 5.7: Comparison of ion energy distribution at 1.4m, 77° with Express [4], Boyd [5] and this work.

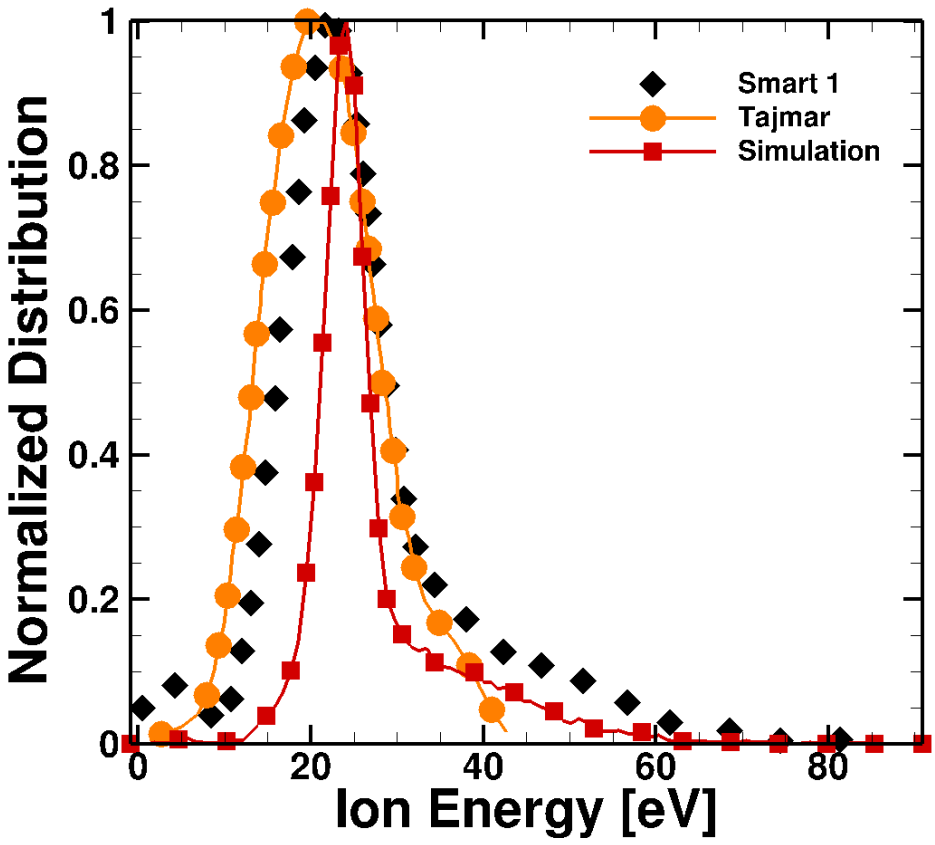

Figure 5.8: Comparison of ion energy distribution at 0.57m, 85° with SMART 1 [3], Tajmar [3] and this work. SMART-1 data shifted by 22.5 eV.

5.6 Comparison of plume flowfields

In this section the electron fluid and the polytropic model solutions are compared in the presence of a solar panel with a spanwise potential gradient. The electron fluid model solves the electric potential (Eq. 2.22) and electron temperature (Eq. 2.30) equations and polytropic model solves Eq. 2.13. The boundary conditions and thruster exit conditions given in section 5.1 were used. In Fig. 5.9 the plasma potential solution for the two electron models are given. Unlike the electron fluid model, the polytropic model estimates a more rapid plasma potential drop radially outside the plume region. This is because when the number density of ions decreases the RHS of Eq. 2.13 becomes negative and the plasma potential goes to negative values. On the other hand, since the electron fluid model solves Poisson like equations, it estimates a more gradual potential drop than the polytropic model. The larger potential drop results in larger radial electric field values for the polytropic model compared to the electron fluid model as can be seen in Fig. 5.10.

In Fig. 5.10 the thruster outer and inner wall y locations are shown as dashed lines. Since Hall thrusters are annular ion source devices, we see a negative electric field below the thruster inner wall because there are fewer ions present at the centerline of the thruster. Thus, the plasma potential is lower at that location and the radial electric field is towards the negative y-direction. Similarly, above the thruster outer wall, there is a lower plasma potential and the radial electric field is in the positive y-direction. Since the radial electric field estimated by the polytropic model is larger, we expect more ions to move radially and be attracted by the solar panel in the backflow region. The axial electric field in the backflow region is shown in Fig. 5.11. Both models predict an almost linear change in the axial electric field. This linear variation is due to the linear electric potential gradient imposed by the solar panel in the domain.

Normalized number density distribution of Xe^{+} and Xe^{+2} ions are given in Figs. 5.12-5.13. In the core plume region, the spatial distribution of both Xe^{+} and Xe^{+2} are similar for both models. Similarly, spatial distribution of ions are similar for both electron models at the backflow region. These ions are CEX ions created in the core plume region that move to the backflow region. Since the CEX ions have lower axial velocity than the beam ions, they are attracted by the radial electric field and move to the backflow region. In

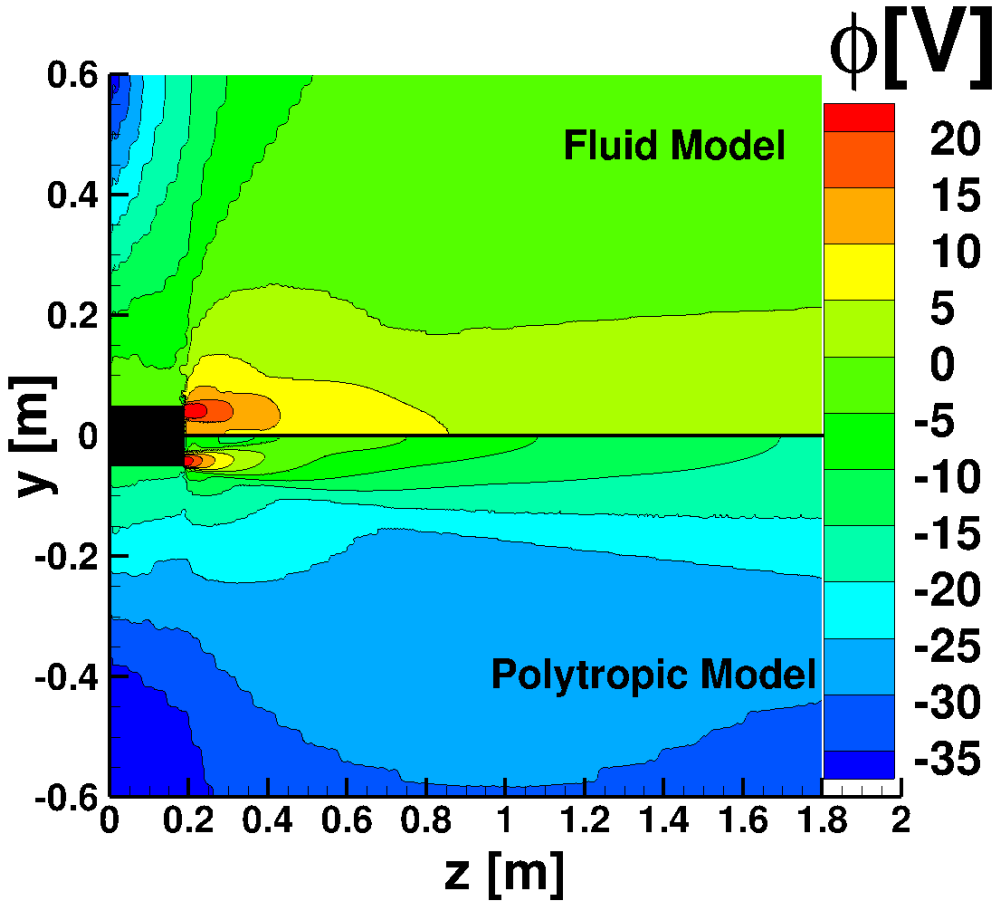

Figure 5.9: Comparison of plasma potential between the electron fluid and the polytropic models in the presence of solar panel with a spanwise potential gradient.

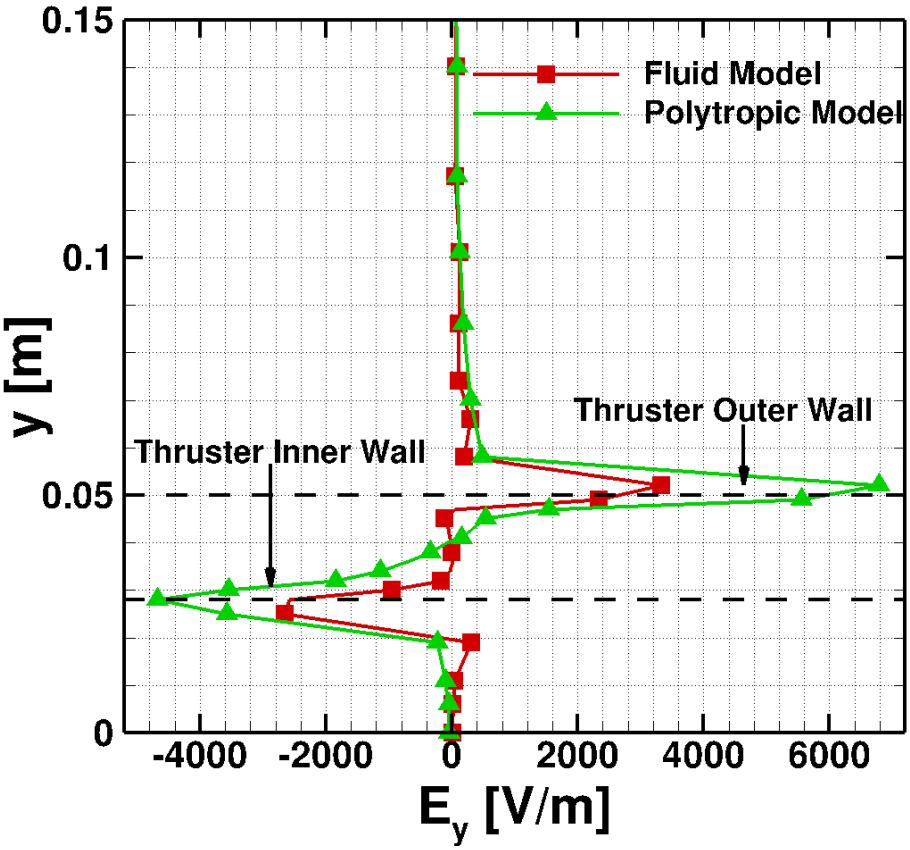

Figure 5.10: Comparison of radial electric field at $z = 0.19$ m between the electron fluid and the polytropic model.

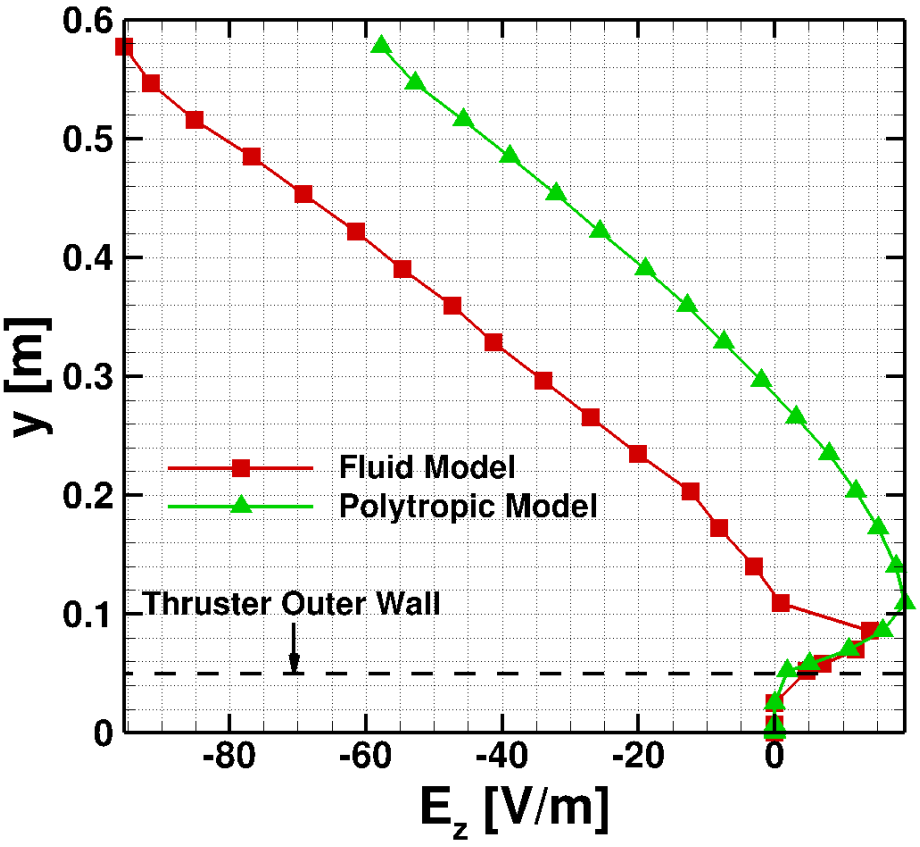

Figure 5.11: Comparison of axial electric field at $z = 0.10$ m between the electron fluid and the polytropic model.

Figs. 5.14-5.15 the ion axial velocity spatial distributions are given. The core plume region ion velocities are similar for the electron fluid and polytropic models. Streamlines for both ions show that in the backflow region, ions are moving towards to the edge of the solar panel which has the most negative potential. The CEX ion distribution is given in Fig. 5.16-5.17. As expected the largest CEX population is in the core plume region close to the thruster exit where they are created. The CEX ions then move to the backflow region due to the radial electric field. The relative population of CEX to all ions are given in Fig. 5.18 and in Fig. 5.19 for Xe^{+} and Xe^{+2} respectively. It can be seen from the figure that the CEX ions are dominant outside of the core plume region and in the backflow region. Since there is very little number of ${Xe^{+2}}_{CEX}$ partilces in the backflow region, there is noise in figures showing ${Xe^{+2}}_{CEX}$ population in the backflow. This noise can only be eliminated by decreasing FNUM, which requires more memory for the computation.

Trajectories of CEX ions moved to backflow region can be seen from the CEX ions streamlines, given in Fig. 5.18-5.19. For the electron fluid model, CEX ions hit the solar panel more steeply compared to the Polytropic model, as can be seen in Fig. 5.18. This is because for the electron fluid model the axial electric field is larger than the polytropic model, as shown in Fig. 5.11. In addition to that for the electron fluid model the radial electric field is smaller than the polytropic model, as shown in Fig. 5.10, in consequently ions can move parallel to solar panel. This behaviour can also be seen from angle of incidence results for the electron fluid and the polytropic model for the probes closest (i.e. probes 1,4,7) to the solar panel as given in Fig. 5.21. Probes closest to the solar panel estimate higher angle of incidence for the polytropic model than the electron fluid model.

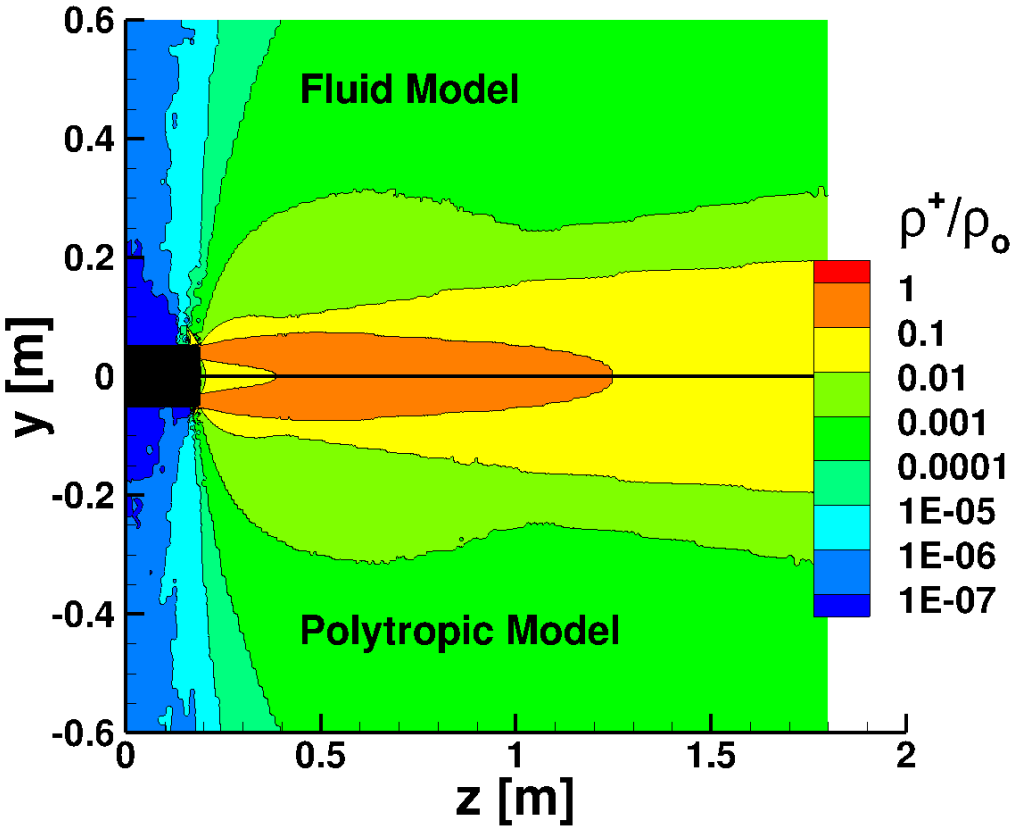

Figure 5.12: Comparison of normalized number density of Xe^+ ($\rho_0 = 2.54 \times 10^{17}\mathbf{m}^{-3}$).

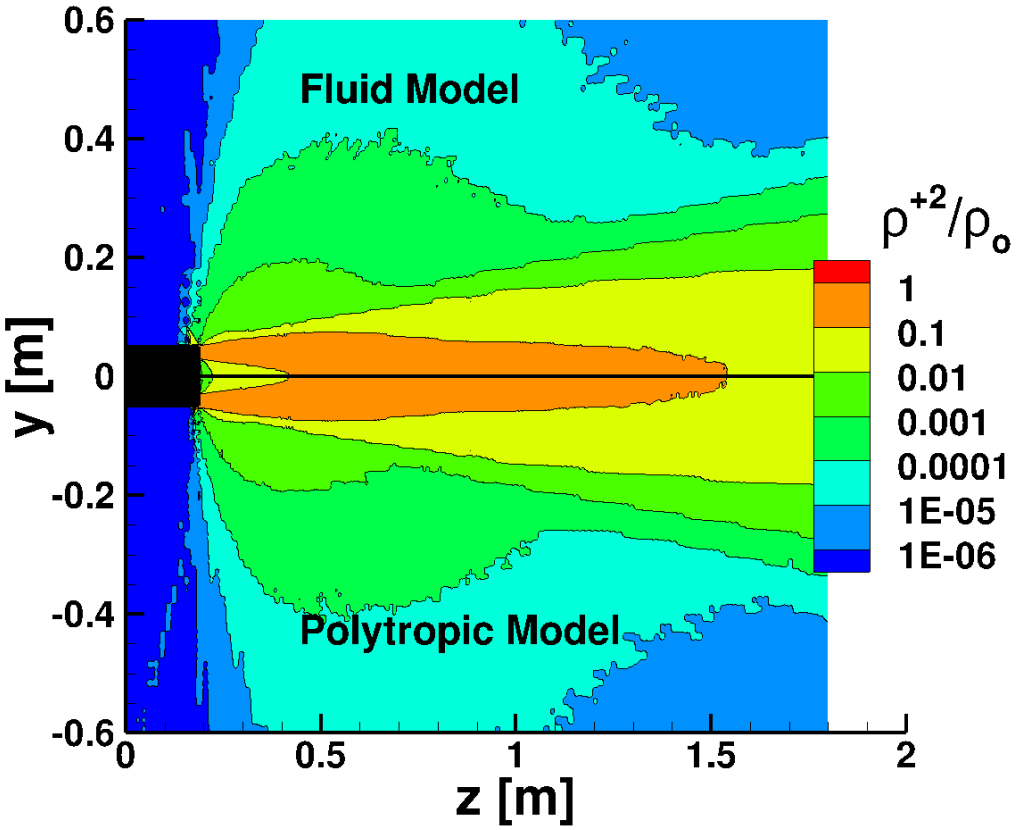

Figure 5.13: Comparison of normalized number density of Xe^{+2} ($\rho_0 = 0.28 \times 10^{17}\mathbf{m}^{-3}$).

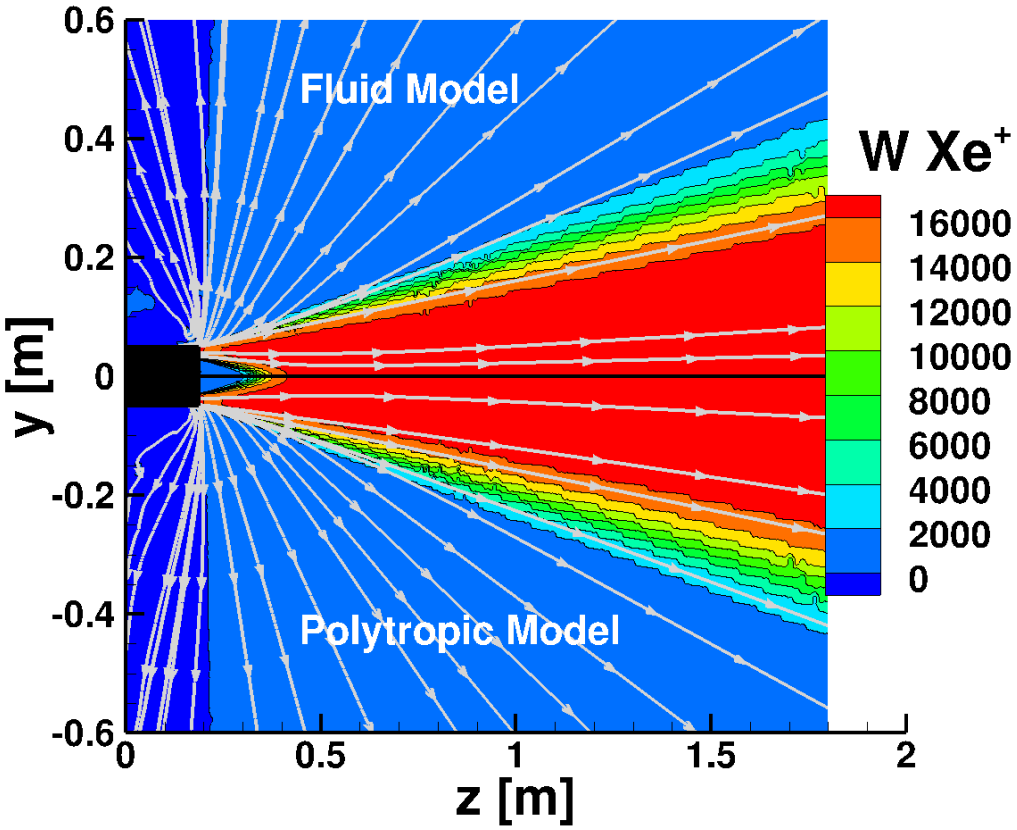

Figure 5.14: Comparison of axial velocity [m/s] of Xe^+ with streamlines of Xe^+.

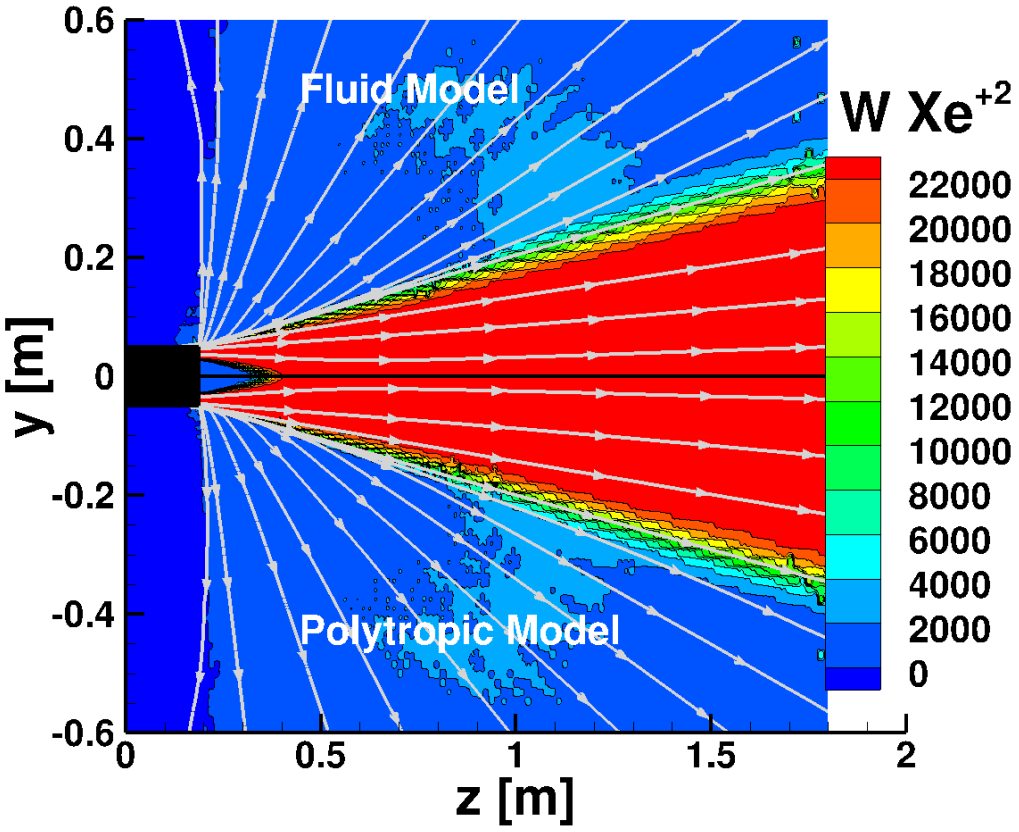

Figure 5.15: Comparison of axial velocity [m/s] of Xe^{+2} with streamlines of Xe^{+2}.

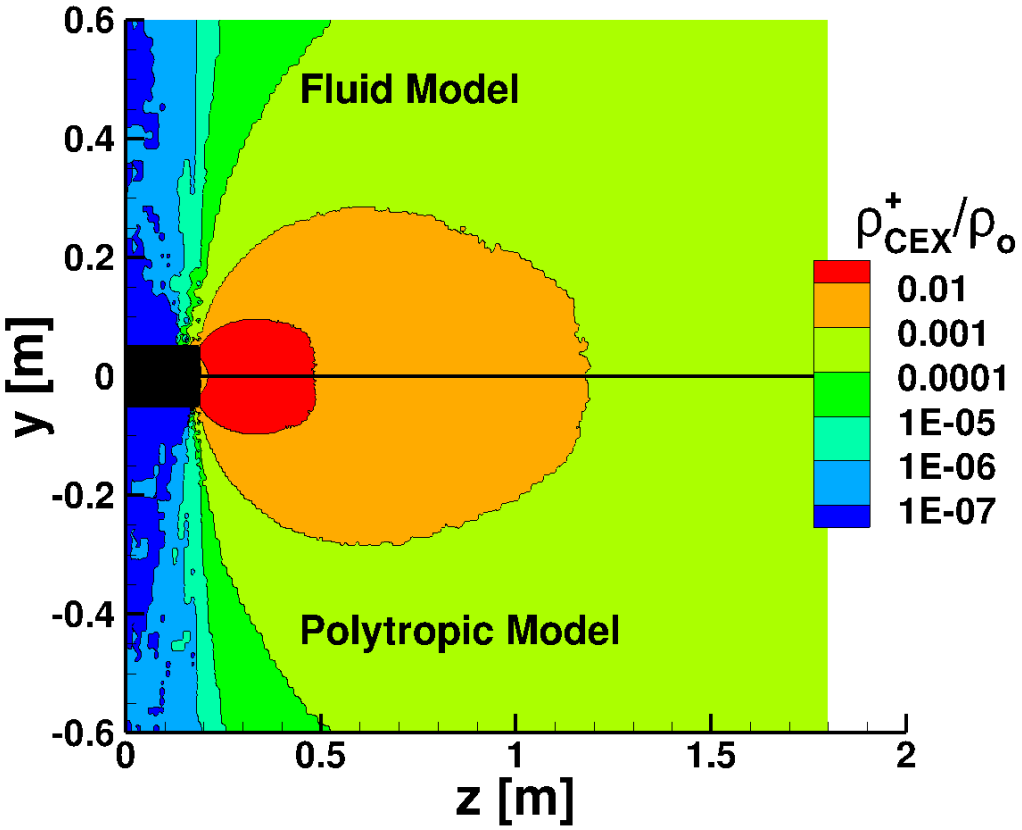

Figure 5.16: Comparison of normalized number density of $\mathbf{Xe^+_{CEX}}$ ($\rho_0 = 2.54 \times 10^{17}\mathbf{m}^{-3}$).

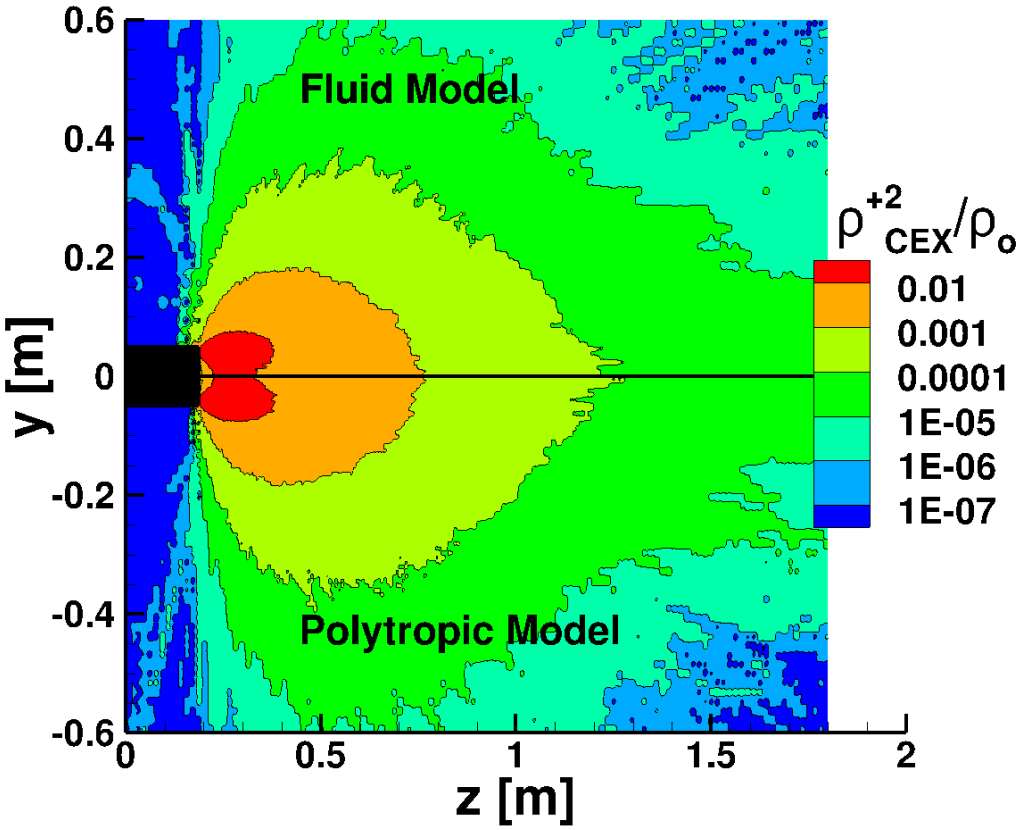

Figure 5.17: Comparison of normalized number density of $\mathbf{Xe^{+2}_{CEX}}$ ($\rho_0 = 0.28 \times 10^{17}\mathbf{m^{-3}}$).

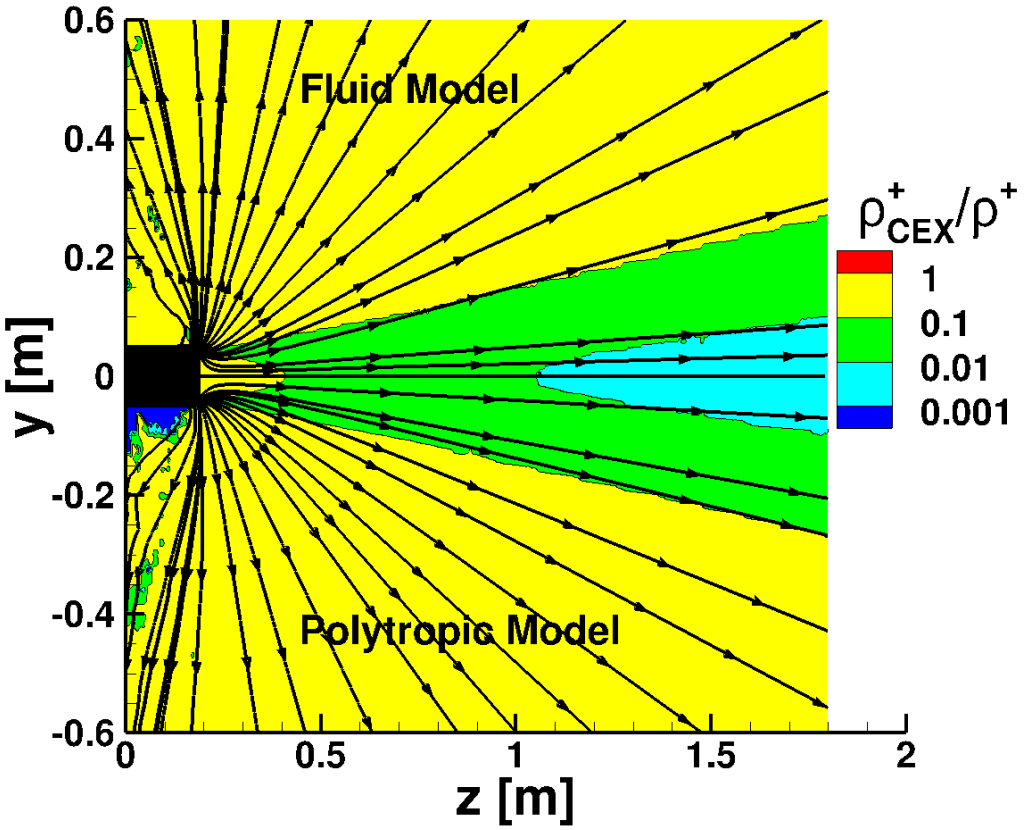

Figure 5.18: Number density ratio of Xe^+_{CEX} to Xe^+ with streamlines of Xe^+_{CEX}.

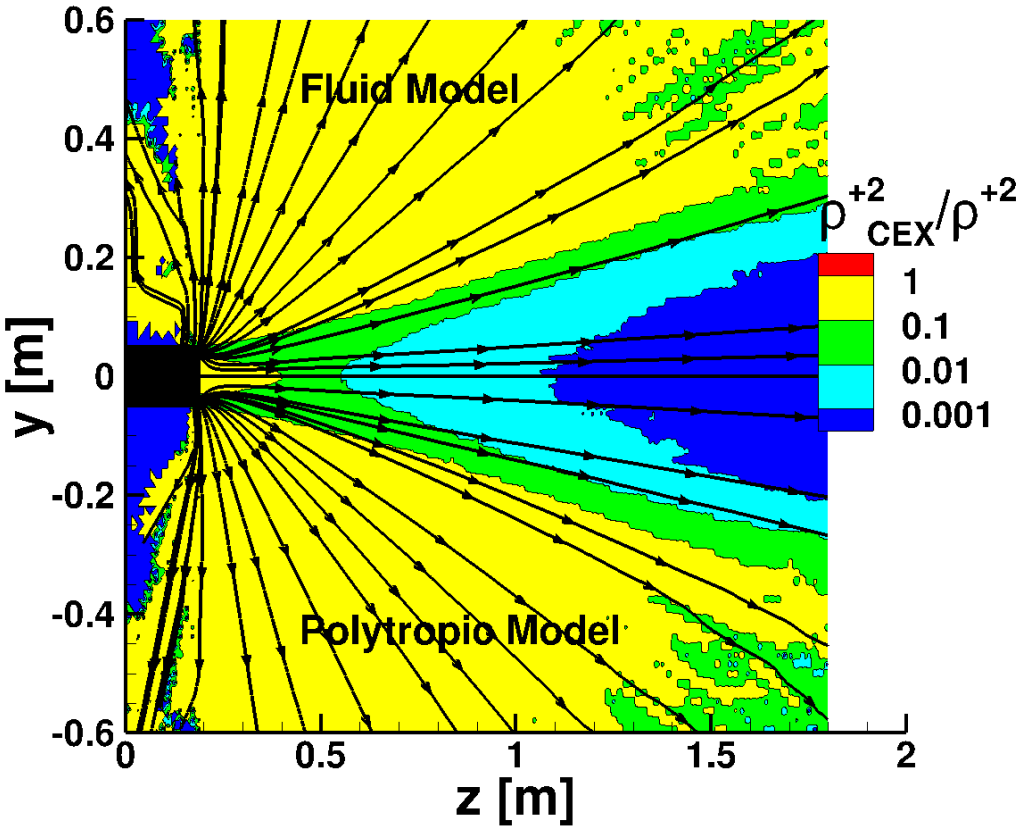

Figure 5.19: Number density ratio of $Xe^{+2}{}_{CEX}$ to Xe^{+2} with streamlines of $Xe^{+2}{}_{CEX}$.

5.7 Sputtering Calculations

Sputtering calculations for the electron fluid and the polytropic model are given in this section. Ion energy and incidence angles are collected at 9 different regions using computational probes in the backflow region. The computational probe locations are given in Table. 5.3. Probe data is collected for 10,000 timesteps after sampling for macro properties is completed from time step 300,001 to 310,000 and every 100^{th} time step ion energy and velocity are collected. Ion energy distributions measured by computational probes using the electron fluid and the polytropic model are given in Fig. 5.20. Probes that have the same x and y coordinates are given in a single figure. Probes 1,4,7 are the closest probes to the solar panel and probes 3,6,9 are the farthest probes from the solar panel. Ion energy distribution computed by using the electron fluid and the polytropic model is similar. It can also be seen from the normalized ion energy distributions that probes closest to the solar panel (i.e. probes 1,4,7) have smaller ion energies than the ones that are farthest (i.e. probes 3,6,9). This is counter-intuitive because cells closest to the solar panel have the lowest electric potential, Fig. 5.9, and a CEX ion created at the thruster exit would experience an approximately energy drop of 60 eV when it moves from the thruster exit to the solar panel surface. However, normalized ion energy distributions taken at positions closest to the solar panel show that the highest population of ions have energies of 5eV. In order to understand why ions hitting the solar panel have such lower energies, we have looked at the angle of incidence of ions at different locations measured by the computational probes. The normalized distribution of the angle of incidence of ions is given in Fig. 5.21 for the electron fluid and the polytropic model. Angle of incidence is the angle between particle incidence velocity vector and the solar panel normal. The angle of incidence data from different probes gives an idea of how the trajectory of ions change between the thruster exit and solar panel. Probes farthest (i.e. probes 3,6,9) from the solar panel show an angle of incidence around 90 degrees, which means that ions are moving parallel to the solar panel span. As expected CEX ions created at the thruster exit first move radially outward (i.e. in the y-direction) from the thruster parallel to solar panel span. Then, because of the attraction of the solar panel, ions turn and move towards the solar panel. This can be seen also in Fig. 5.21, where probes closest (i.e. probes 1,4,7)

to the solar panel have smaller angle of incidence than the ones farthest (i.e. probes 3,6,9). Also, ions turn towards the solar panel because they gain a negative z velocity as can be seen in Fig. 5.22 for both electron models, when they are approaching the solar panel due to the negative electric field. From farthest probe location (i.e. probes 3,6,9) to the closest probe location (i.e. probes 1,4,7) to the solar panel, the axial velocity of ions increases in the negative direction. However, even though the velocity of ions increases as they approach the solar panel surface, the ion energies obtained from the computational probes show a decrease in ion energy as ions approach the solar panel surface. This process can be explained by Xe-Xe^+ CEX and MEX reactions.

Numerical simulation of Hall thruster plume and spacecraft interactions are investigated by researchers, because of the interest of erosion of spacecraft charged surfaces or spacecraft charging. Roussel et. al. [48] investigated the erosion of solar panel coverglass and interconnects using a Monte-Carlo and particle in cell method. They provide the erosion rates of the solar panel coverglass and interconnects. However, in their models, they did not consider the neutralization of ions that hit the solar panel surface. Tajmar et. al. [10] also investigated the Hall thruster plume and spacecraft interaction using MCC and PIC code, and they stated that the peak value of CEX ions was around 20 eV, which is below the threshold energy of aluminum ($E_{th} = 28.67$ eV). Korkut and Levin [39] showed in their modeling of backflow of ion thruster plumes that when a gas-surface interaction model was used ion velocities in the vicinity of the solar panel decreased and created a deceleration zone in front of the solar panel. Gas-surface interactions create new slow-moving neutrals in the vicinity of the solar panel and these new neutrals accumulate in the backflow region because of their small thermal velocity. These new neutrals created at the backflow region due to neutralization, undergo subsequent CEX reactions with the ions incoming from the thruster exit. Thus new CEX ions created in the backflow region have lower energies. This phenomenon can be seen in Fig. 5.23 where ratio of Xe neutrals created due to CEX reaction to the total Xe neutrals. As can be seen from the streamlines of Xe given in Fig. 5.23, created neutrals on the surface of the solar panel due to neutralization move towards the positive z-direction and go into CEX reaction with the incoming ions and create a region of dominant CEX neutrals in the vicinity of the solar panel. The ratio

of Xe_{CEX}/Xe equals to 1, means that in that region most of the neutrals are created as a result of CEX reaction. In addition to that, there is a dominant region of Xe_{CEX} neutrals in the core plume region close to thruster centerline. These are the fast-moving Xe_{CEX} neutrals created at the thruster exit and they have been seen without the solar panel in domain as well. For the backflow region, it was not possible to explain this phenomenon by looking at the CEX ion distribution, because ions incoming from the thruster exit to the backflow region are also CEX ions. So, new CEX ions created at the backflow region cannot be understood from the CEX ion distributions.

To sum up, for a steady-state simulation because of the gas-surface interaction model applied there is a neutral accumulation at the vicinity of the solar panel and due to the Xe-Xe^+ CEX reactions, incoming ions from the thruster exit loose their energy and impinge on the solar panel with such small energies that sputtering cannot happen. Reflected neutrals from the solar panel create a shield for the incoming ions.

Table 5.3: Computational probe locations (x = 0.0 - 0.17 m).

	z coordinates [m]		
y coordinates [m]	**0.0 - 0.05**	**0.10 - 0.15**	**0.15 - 0.20**
0.15 - 0.30	1	2	3
0.30 - 0.45	4	5	6
0.45 - 0.60	7	8	9

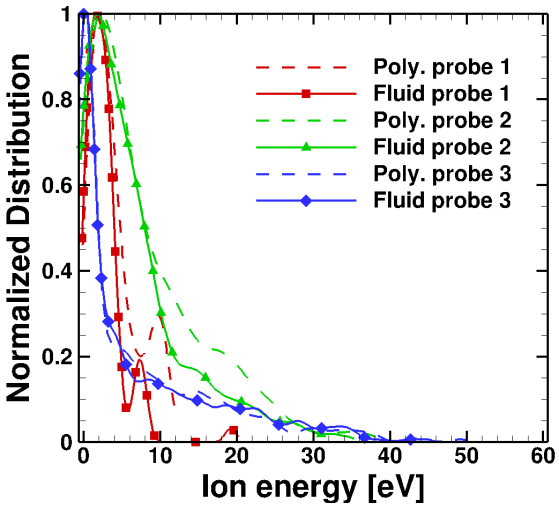

a) Probes 1, 2, 3

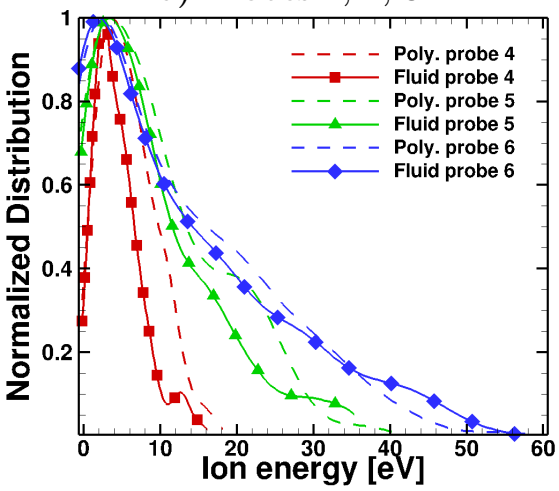

b) Probes 4, 5, 6

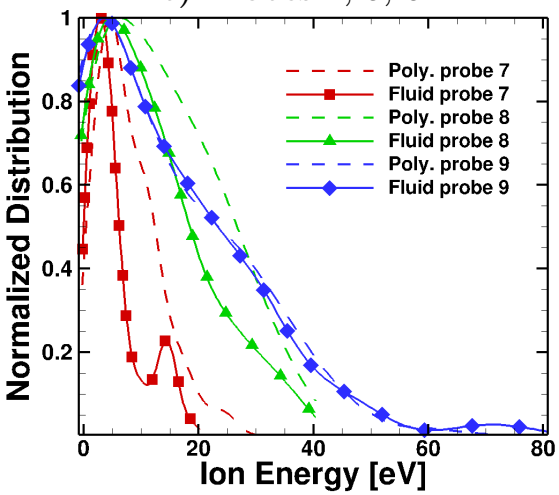

c) Probes 7, 8, 9

Figure 5.20: Ion energy distributions at different locations using the polytropic and the electron fluid model.

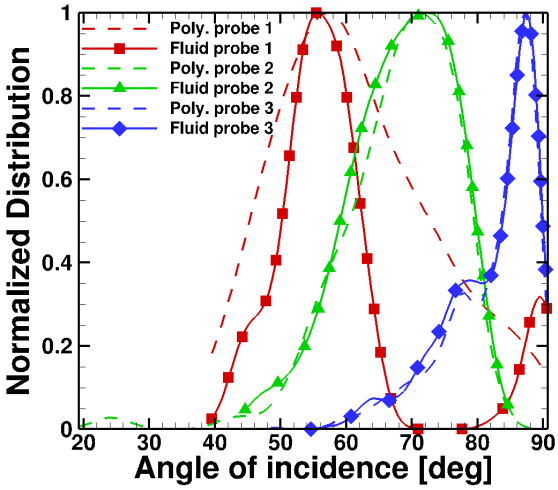

a) Probes 1, 2, 3

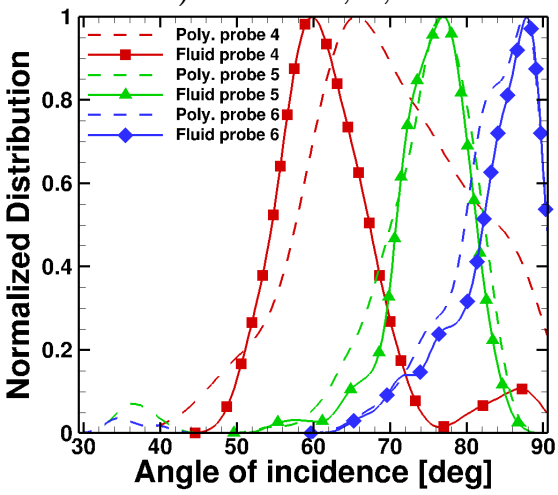

b) Probes 4, 5, 6

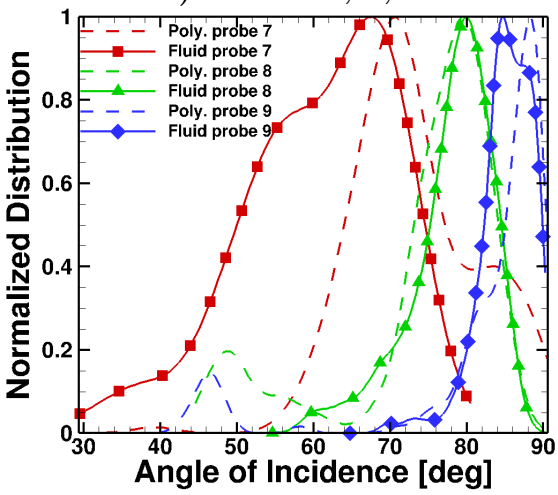

c) Probes 7, 8, 9

Figure 5.21: Angle of incidence distributions at different locations using the polytropic and the electron fluid model.

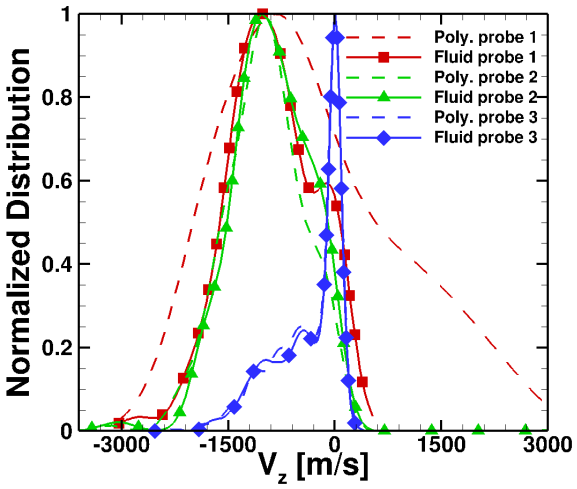

a) Probes 1, 2, 3

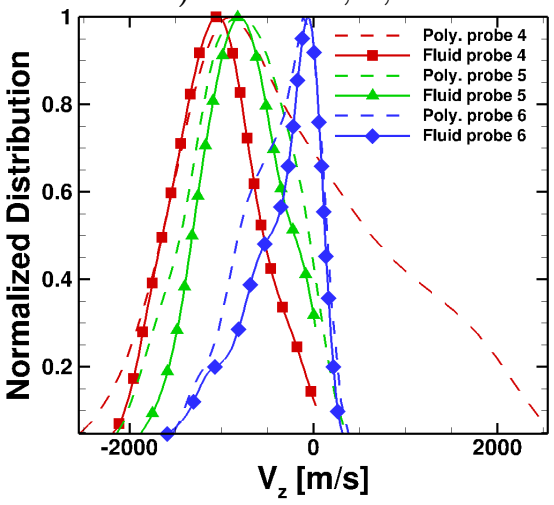

b) Probes 4, 5, 6

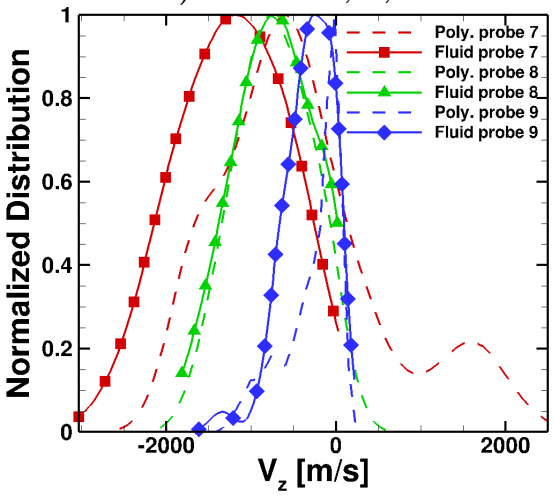

c) Probes 7, 8, 9

Figure 5.22: Axial velocity distributions at different locations using the polytropic and the electron fluid model.

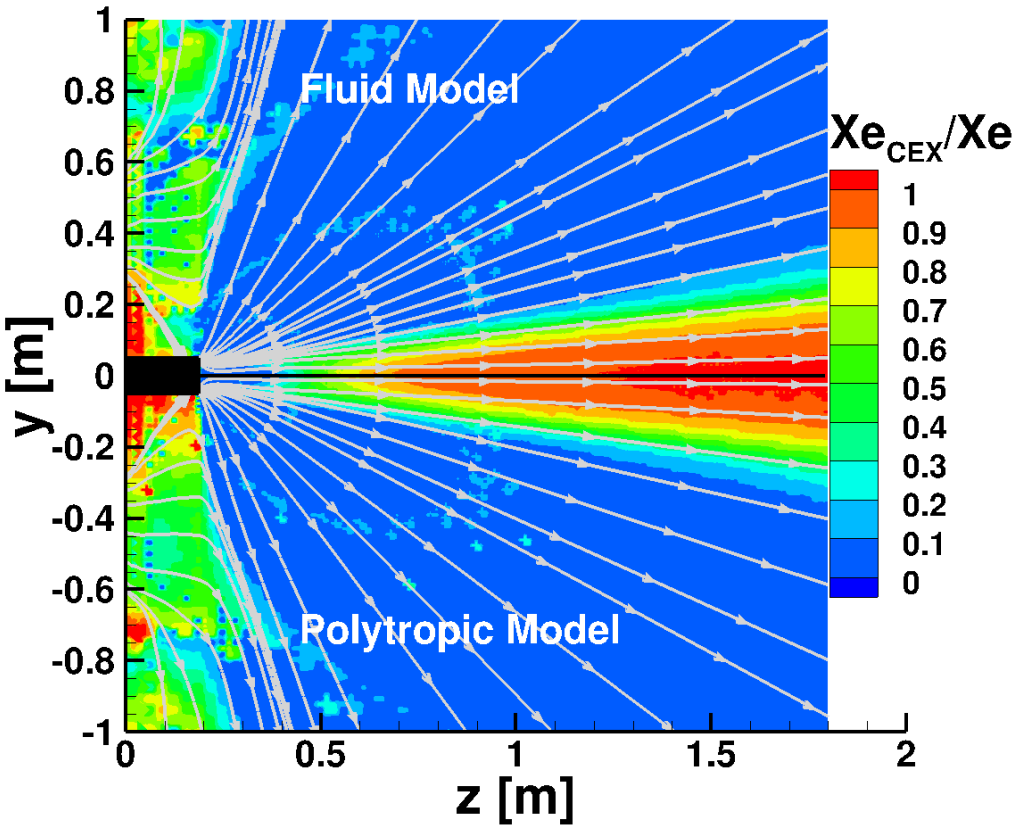

Figure 5.23: Ratio of Xe_{CEX}/Xe with streamlines of Xe.

Chapter 6

Summary and Conclusions

In this thesis, a 3D DSMC-PIC hybrid kinetic simulation of a well known, stationary plasma thruster SPT-100 was done using hybrid MPI-GPU AMR code CHAOS. Xe atoms, Xe^{+} and Xe^{+2} ions are modeled using a kinetic approach. DSMC method is used to model the MEX and CEX reactions between neutrals and ions. Since the ion and neutral particle axial velocities are two orders of magnitude different a species-based time-steps and weight are used to overcome the inefficiency of using small time-steps for slow particles and also artificially increasing the number of computational particles of trace species to realistically simulate the interactions between major and trace species. Modeling electrons using a kinetic approach is not feasible in today's computational power for a Hall thruster plume. Thus three different models are used to compute the plasma potential.

First, Boltzmann and polytropic closures are used for electric potential calculations. Simulation results of both electron closures are compared. The electric potential calculated using both models showed different profiles. The polytropic model predicted radially expanded profile and Boltzmann model predicted radially confined profile. Although neutral number density results of both models predicted similar profiles, axial velocity predictions in the far field and close to thruster axis showed differences which can be related to the number of fast neutral created close to thruster axis in the far field. Finally, calculated current density results are compared with experimental measurements [2] and simulation results [1] in the literature. It can be concluded that in the far field electron temperature gradient effect becomes more dominant and using polytropic models with adiabatic exponent values lower than theoretical value shows better agreements with experimental results [2]. Although, the near field region has a higher collision rate and electron temperature, as the plume propagates collision rate almost drops to a collisionless flow [28], which drives the adiabatic exponent to a smaller value than

the theoretical one. Since, the adiabatic exponent is a function of thruster operating point and configuration [28], as well as it spatially varies inside the plume [29], for Hall thruster plume simulations we need more detailed models which are derived from the electron fluid equations.

Electron momentum and energy equations are implemented in CHAOS and they are solved to find the plasma potential on an AMR octree grid for a 3D simulation using the preconditioned conjugate gradient method in a Particle in Cell (PIC) approach. First, the current density values at near field obtained using the electron fluid model are compared with the Boltzmann and the polytropic model and previous experimental measurements [2] and simulations [1]. It has been seen that current density values obtained by using the electron fluid and the Boltzmann model are similar and showed a worse comparison with experimental measurements [2] than the polytropic model. In order to improve the current density results of the electron fluid model, different thruster exit potentials and electron temperatures can be tried and best match with the experimental measurements can be found. In order to investigate the dependency of thruster exit electron temperature and thruster exit potential on our simulations with the electron fluid model, a sensitivity study is done. Ion energy distributions are compared for different thruster exit electron temperatures and it has been seen that the width of the distribution depends on the thruster exit electron temperature. Also, it has been seen that the peak energy of ion energy distribution depends on the thruster exit potential. Following the sensitivity study, verification test cases for the electron fluid model is done. Ion energy distribution at 3 different locations are compared with Express [4] and SMART-1 [3] flight measurements and simulations of Boyd [5] and Tajmar [3]. Our simulations showed a very good agreement for ion energy distributions between Express flight measurement and simulation of Boyd at two different points, for the selected parameters. However, our simulation results show disagreements at one point for the ion energy comparisons with SMART-1 spacecraft flight data and previous simulations [3], for the chosen parameters.

Following the verification of the electron fluid model, a 3D simulation with a solar panel in the domain is done for both polytropic and electron fluid model. Effect of the solar panel for electric potential is added to the domain by solving the Laplace equation and superimposing with the plasma potential computed by the polytropic model. For the electron fluid model, cells that

belong to the solar panel are assigned as Dirichlet boundary. Since the solar panel is a surface in the domain, the gas-surface interaction model is also considered and ions hit the solar panel are neutralized and reflected back into the domain.

Plasma potential estimated by the polytropic and electron fluid model is different than each other. The electron fluid model estimated a more gradual potential drop than the polytropic model. Spatial distribution of beam and CEX ions for both models showed similar profiles for both electron models. It can be concluded that in terms of the spatial distribution of ions in the core plume and in the backflow region both models estimated similar profiles and there is no need to use the electron fluid model. Trajectories of CEX ions also show a difference between the electron fluid model and the polytropic model. For the electron fluid model, CEX ions move more steeply than the polytropic model. This is because the axial electric field estimated by the electron fluid model is larger than the polytropic model in the backflow region.

Finally, sputtering calculations for the electron fluid and the polytropic model showed an interesting phenomenon. Because of the neutrals created due to the neutralization of ions that hit to the solar panel, a neutral population is created at the vicinity of the solar panel. CEX ions coming from the thruster exit to the solar panel surface go into one more CEX reaction with these neutrals and as a result ions with small energies are created. These new small energy ions hit the solar panel, but since their energy is smaller than the threshold energy of aluminum, sputtering cannot happen. Thus at steady-state, reflected neutrals from the solar panel creates a shield region.

As future work, it will be interesting to consider the neglected terms in electron momentum and energy equations, such as magnetic field effects, Ohmic heating, and convective effects. Also, it will be interesting to revisit the gas-surface interaction model, so that every ion hit the solar panel is not neutralized.

Appendix A New modules implemented in CHAOS

In this section, functions and kernels used in implemented electron fluid model of CHAOS are explained. In this documentation, functions and kernels are explained briefly and for more detailed information about the general structure of CHAOS and PCG solver reader has to refer to ref. [35, 16]. Directory of the electron fluid model version and polytropic model version of the CHAOS code can be found in directories given below.

- Fluid code: MyPC_Documentation/CHAOS_electron_fluid_model/src/
- Polytropic code: MyPC_Documentation/CHAOS_electron_polytropic_model/src/

Main function to call routines to solve Poisson like plasma potential (Eq. 2.22) and electron energy (Eq. 2.30) equations is *ComputePoisson* function given in List. A.1. Plasma potential and electron energy equations are turned into the form given in Eq. 3.3 and plasma potential and electron temperature are solved using PCG solver. *ComputePoisson* function can be found under the file *electromagnetics/electromagnetics.cpp*. Every time new octree-regenerated, first *CalculateElectricPotential* function is called to compute electric potential using the polytropic model in each cell, in order to find the initial guess of electric potential to use in Poisson solver. If octree is not regenerated in that time-step, ϕ value from the previous time-step is used. *CalculateEPressure* function given in List. A.2 is used to compute the electric conductivity (σ_e) and the thermal conductivity (κ_e) values in each E-Octree leaf node and it is under the file *electromagnetics/def_electromagnetics.cu*. Conductivity values are computed in GPUs so *Kernel_CalculateEPressure* is called and each GPU thread computes conductivity values of each E-Octree leaf node. Conductivity values are computed based on Eq. 3.6. Also, ionization term in the electron energy equation, which becomes the source term of Eq. 3.3, is computed in this Kernel as well. After conductivity values

are computed RHS of the plasma potential (Eq. 2.22) equation is computed using *GenerateRHS* function, given in List. A.4 and located under the file *electromagnetics/def_electromagnetics.cu*. Kernel used to compute the RHS of plasma potential equation is called *Kernel_RHSVec* and located under the file *electromagnetics/def_electromagnetics.cu*. Part of the kernel is given in List. A.5. LHS of plasma potential and electron energy equations, which becomes the Eq. 3.3, are computed by *GenerateLinearMatrixMomentumEq* function, given in List. A.6. This function calls two Kernels in GPUs to compute the LHS of Poisson like equations. These kernels are *Kernel_MomentumEquation* and *Kernel_EnergyEquation* for LHS of the plasma potential (Eq. 2.22) and electron energy (Eq. 2.30) equation, when they are in the form of Eq. 3.3, respectively. Since both of the kernels have same structure only *Kernel_MomentumEquation* given in List. A.7 and both kernels are located under the file name *electromagnetics/def_electromagnetics.cu*. After, LHS of Poisson like equations is computed, using the PCG solver first electron temperature T_e is solved and then plasma potential ϕ is solved in each E-Octree leaf node.

```
void ComputePoisson(......)
{
   if(octree_regenerated=true)
   {
     CalculateEletricPotential(......); // Use polytropic model at octree-
    generation step
   }

   CalculateEPressure(......); // Compute conductivities

   GenerateRHS(......); // Generate RHS of plasma potential equation

   GenerateLinearMatrixMomentumEq(......); // Generate LHS of plasma
    potential and electron temperature equation

   PCGSolver_Te(......); // Solve electron temperature

   PCGSolver(......); // Solve plasma potential
}
```

Listing A.1: Solve Eqs. 2.22-2.30

```
void CalculateEPressure(......)
{
   double *dev_nue = cpu_gpu_comm->_dev_nue; // Total electron collision
    frequecy
   double *dev_sigmae = cpu_gpu_comm->_dev_sigmae; // Electric conductivity
   double *dev_nuen = cpu_gpu_comm->_dev_nuen; // Electron-Neutral collision
     frequency
   double *dev_nuei = cpu_gpu_comm->_dev_nuei; // Electron-Ion collision
    frequency
   double *dev_Te = cpu_gpu_comm->_dev_Te; // Electron temperature
   double *dev_ne = cpu_gpu_comm->_dev_ne; // Electron number density
   double *dev_Ke = cpu_gpu_comm->_dev_Ke; // Thermal Conductivity of
    Electrons in terms of natural log
   double *dev_RHSVecTe = cpu_gpu_comm->_dev_RHSVecTe; // Electron energy
    equation  RHS

   Kernel_CalculateEPressure<<<...>>>(.....);
   cudaDeviceSynchronize();
   cudaCheckErrors(" kernel calculate electron pressure ");
}
```

Listing A.2: Compute σ_e and κ_e

```
__global__ void Kernel_CalculateEPressure(.....)
{
    if(tid<numLeafNodes)
    {
/* Electron Collision frequncy is calculated. For now only neutral and
    electron collision */
/* are calculated. Refer Keider, Boyd, Bellis 2001 */
       double sigma_en = 10E-20; // electron neutral collision cross-section
     [m-2]
       double PI = 3.141592653589793;
       double me = 9.10938356E-31; // mass of electron [kg]
       ve_thermal = sqrt(double(double(8*elementary_charge*Te_temp_eV)/
    double(me*PI))); // Thermal velocity of electrons
       nu_en   =  double(ND_neutral * sigma_en * ve_thermal); // Collision
    frequency electron atom
/* Electron Collision frequncy is calculated. Ion  and electron collision*/
/* are calculated. Refer Y. Choi PhD. Theises UMICH, 2008*/
       double permittivity_freespace = 8.85418782 * 1.0E-12;
       double l_debye = sqrt((permittivity_freespace*k*Te_temp_K)/(ND_el*
    elementary_charge*elementary_charge));
       double ln_gamma = log( ND_el * pow(l_debye,3) );
       double nu_ei = (ND_el * pow(elementary_charge,4) * ln_gamma)/(2*PI*
    pow(permittivity_freespace,2)*sqrt(me)*pow((3*k*Te_temp_K),1.5));
       double nue_temp = nu_ei + nu_en; // electron-ion and electron-atom
    collision frequencies
       mu_en = double(elementary_charge / (me*nue_temp)) ; // electron
    mobility
       sigmae[tid] = mu_en * ND_el * elementary_charge; // electron
    conductivity
// Ionization Xe + e- => Xe+ + 2e-  and RHS of electron momentum equation
// Ionization cross-section is from E. Ahedo et. al.  2001 Physics of Plasma
// RHS form is from Ph.D. theisis of M. Choi UMICH, Eq. 2.18
       double sigmai0 = 5E-20; // Reference cross-section m2
       double ce = sqrt(double(8*Te_temp_eV*elementary_charge)/(PI*me)); //
    Electron thermal velocity m/s
       double Ei = 12.1; // Ionization energy of Xe in eV
       double Ci = ce*sigmai0*(1.0 + double((Te_temp_eV*Ei)/pow(Te_temp_eV+
    Ei,2)))*exp(-1*Ei/Te_temp_eV); // Ionization rate m3/s
// Thermal Conductivity of Electrons  ///
// Boyd & Yim 2004 Journal of Applied Physics Volume 95 Number 9 //
// Equation 12b //
       Ke[tid] = double(2.4/(1.0+nu_ei/(sqrt(2.0)*nue_temp))) * double((k*k*
    ND_el*Te_temp_K)/(me*nue_temp)); // Watt/m.eV
       RHSVecTe[tid] = -1*ND_el * ND_neutral * Ci * 12.1 * elementary_charge
    *volumeOfLeaf[tid]; // Ionization energy sink term 12.1 eV ionization
    energy of xenon
    }
}
```

Listing A.3: Kernel_CalculateEPressure

```
void GenerateRHS(.....)
{
   double *dev_RHSVec = cpu_gpu_comm->_dev_RHSVec;
   double *dev_sigmae = cpu_gpu_comm->_dev_sigmae;
   double *dev_Te = cpu_gpu_comm->_dev_Te;
   double *dev_ne = cpu_gpu_comm->_dev_ne;
   double *dev_Ke = cpu_gpu_comm->_dev_Ke;

   Kernel_RHSVec<<<....>>>(.....);
   cudaDeviceSynchronize();
   cudaCheckErrors(" enlist nbr id wrt data array ");
}
```

Listing A.4: Compute RHS of Poisson like plasma potential equation

```
__global__ void Kernel_RHSVec(.....)
{
   if(tid<totalLeafNodes)
   {
      int HeadInArray = headFaceNbrIdInList[tid*6] + tid;
      int counter = 0;
      double MyVol = volumeOfLeaf[tid];
      double dx = cbrt(MyVol);
      double area = dx*dx;
      double My_sigmae = sigmae[tid];
      double My_Te = Te[tid];
      double My_ne = ne[tid];
      double Nbr_sigmae, Nbr_Te, Nbr_ne;
      for(int i_face=0;i_face<3;i_face++)
      {
        if(DomBndryFaceFlag[tid*6+i_face]==0)
        {
          for(int i=0;i<NumFaceNbrs[tid*6+i_face];i++)
          {
           double delta = 0.5 * (dx + Nbr_dx);
           double f_sigmae = delta * double ( (2.0* My_sigmae * Nbr_sigmae)
    /(My_sigmae*Nbr_dx+Nbr_sigmae*dx));
           double f_Te = delta * double ( (2.0* My_Te * Nbr_Te)/(My_Te*
    Nbr_dx+Nbr_Te*dx))*kb/elementary_charge;
           double d_Te = (Nbr_Te - My_Te)*kb/elementary_charge ;
           double d_lnne = log(Nbr_ne) - log(My_ne);
           double Nbr_coeff = 1.0 * (flux_area)/ ( delta ) * f_sigmae * (
    d_Te +  f_Te * d_lnne);
           CoEff_sum += Nbr_coeff;
          }
        }
      }
      ....
      ....
      ....
      RHSVec[tid] = -1.0 * CoEff_sum ;
   }
}
```

Listing A.5: Kernel_RHSVec

```
void GenerateLinearMatrixMomentumEq(.....)
{
   double *dev_sigmae = cpu_gpu_comm->_dev_sigmae; // Electric Conductivity
   double *dev_Ke = cpu_gpu_comm->_dev_Ke; // Thermal Conductivity

   // Compute LHS of Plasma Potential Equation //
   Kernel_MomentumEquation<<<...>>>(.....);
   cudaDeviceSynchronize();
   cudaCheckErrors(" enlist nbr id wrt data array ");

   // Compute LHS of Electron Energy Equation //
   Kernel_EnergyEquation<<<...>>>(.....);
   cudaDeviceSynchronize();
   cudaCheckErrors(" enlist nbr id wrt data array ");
}
```

Listing A.6: Compute LHS of Eq. 3.3

```
__global__ void Kernel_MomentumEquation(.....)
{
   if(tid<totalLeafNodes)
   {
      int HeadInArray = headFaceNbrIdInList[tid*6] + tid;
      int counter = 0;
      double MyVol = volumeOfLeaf[tid];
      double dx = cbrt(MyVol);
      double area = dx*dx;
      double Mysigmae = sigmae[tid];
      double CoEff_sum = 0.0;
      double Nbr_sigmae;

      for(int i_face=0;i_face<3;i_face++)
      {
        if(DomBndryFaceFlag[tid*6+i_face]==0)
        {
          for(int i=0;i<NumFaceNbrs[tid*6+i_face];i++)
          {
            double delta = 0.5 * (dx + Nbr_dx);
            double f_sigmae = 2.0 * double((Mysigmae * Nbr_sigmae)/(Mysigmae
    + Nbr_sigmae)); // Harmonic Averaging
            double Nbr_coeff = -1.0 * (flux_area)/ ( delta ) * f_sigmae;
            Matrix[HeadInArray+counter] = Nbr_coeff;
            CoEff_sum += Nbr_coeff;
            counter++;
          }
        }
      }
      ....
      ....
      ....
      Matrix[HeadInArray+counter] = CoEff_sum * (-1.0);
   }
}
```

Listing A.7: Kernel_MomentumEquation

Appendix B Directory of layout files

In this section, layout file directories of the figures in this thesis are given.

- Fig. 3.3a => MyPC_Documentation/Averaging_method_verification_files/
  octree_ref_varying_Te_mapions_proof/Comparision_harmonic_arithmatic_analytic.lay
- Fig. 3.3b => MyPC_Documentation/Averaging_method_verification_files/
  octree_ref_forced_numden_linearly_proof/
  ESolution4_arithmatic_harmonic_avg_analytic_comparison_ne_based_on_location_of_octree.lay
- Fig. 3.3c => MyPC_Documentation/Averaging_method_verification_files/
  octree_ref_varying_Te_mapions_proof/ ESolution4_arithmatic_midplane_NDel_1e13.lay
- Fig. 3.3d => MyPC_Documentation/Averaging_method_verification_files/
  octree_ref_forced_numden_linearly_proof/
  ESolution4_arithmatic_avg_ne_calculated_based_on_loc.lay
- Fig. 3.4 = > MyPC_Documentation/Energy_equation_verification_files/
  zmin_20000K_zmax_80000K_poisson_Ke/
  ESolution_with_particles_zmin20000K_zmax80000K_midplane.lay
- Fig. 3.6 = > MyPC_Documentation/Effect_of_Ionization_verification_files/
  Domain01m3_linearly_init/
  Comparison_Nd_5E19_with_without_ionization_Te_8_10_eV_smoothed.lay
- Fig. 3.7a = > MyPC_Documentation/Specular_wall_verification/specular_start/
  withoutPIC/ESolutionFile54000_withoutPIC_quarterthruster_normalized.lay
- Fig. 3.7b = > MyPC_Documentation/Specular_wall_verification/specular_start/
  withoutPIC/ESolutionFile54000_withoutPIC_fullthruster_normalized.lay
- Fig. 3.8 = > MyPC_Documentation/Specular_wall_verification/specular_start/
  without_coll_PIC/S_42k_midplane_comparison_quarter_and_full_thruster_normalized_v2.lay
- Fig. 3.9 => MyPC_Documentation/Specular_wall_verification/specular_start/
  withPIC/Solution_polytropic/
  Solution42k_midplane_comparsion_quarter_full_thruster_normalized_v2.lay
- Fig. 3.10 = > MyPC_Documentation/Domain_comparison/Domain_1m3_2m3_4m3_comparison/
  At_96k_sample/ES96k_alongz_y_at_0039m_1m3_2m3_4m3_comparison.lay
- Fig. 4.1 = > MyPC_Documentation/18_05_29_results_for_ICOPS/new_180604/
  18_05_29_results/poly_boltz_comparison_correct_pot_calc/
  Grid_and_geometry_for_ICOPS.lpk

- Fig. 4.2 = > MyPC_Documentation/18_05_29_results_for_ICOPS/new_180604/
  18_05_29_results/poly_boltz_comparison_correct_pot_calc/
  ESolution300k_poly_boltz_comparison.lay

- Fig. 4.3 = > MyPC_Documentation/18_05_29_results_for_ICOPS/new_180604/
  18_05_29_results/poly_boltz_comparison_correct_pot_calc/
  Solution300k_poly_boltz_comparison.lay

- Fig. 4.4 = > MyPC_Documentation/18_05_29_results_for_ICOPS/new_180604/
  18_05_29_results/poly_boltz_comparison_correct_pot_calc/
  Solution300k_poly_boltz_comparison.lay

- Fig. 4.5 = > MyPC_Documentation/18_05_29_results_for_ICOPS/new_180604/
  18_05_29_results/poly_boltz_comparison_correct_pot_calc/
  Linear_current_density_comparison_at_different_locations_poly_boltz_VG__Kim
  _ss_100k_sp_300k.lay

- Fig. 5.1 = > MyPC_Documentation/JointPropulsionConference_2019/
  Grid_and_geometry_for_JPC.lpk

- Fig. 5.3 = > MyPC_Documentation/Current_density_comparison/
  ES_96k_current_density_at_different_z_locations_along_y_comparison_with
  _experirments_with_boltz_and_poly_solutions.lay

- Fig. 5.4 = > MyPC_Documentation/ion_energy_test_cases/comparison/
  Grouped_comparison_results/
  Comparison_ion_energy_Ti_4eV_tetha_10_Smart1_with_group1.lay

- Fig. 5.5 = > MyPC_Documentation/ion_energy_test_cases/comparison/
  Grouped_comparison_results/
  Comparison_ion_energy_Ti_4eV_tetha_10_Smart1_with_group2.lay

- Fig. 5.6 = > MyPC_Documentation/ion_energy_test_cases/ThrusterExitIonEnergy/
  comparison/Ion_energy_comparisons_for_different_exit_conditions.lay

- Fig. 5.7 = > MyPC_Documentation/ion_energy_test_cases/
  Domain2m3D_Ti_4eV_tetha_10_phiE_20V_phiW_0V_Te_3.5eV_new_inlet_cond/
  Comparison_Express_1_4m_77deg_loc_Te_3_5eV_phiE_20V_new_inlet_cond.lay

- Fig. 5.8 = > MyPC_Documentation/ion_energy_test_cases/
  Domain2m3D_Ti_4eV_tetha_10_phiE_20V_phiW_0V_Te_3.5eV_new_inlet_cond/
  Comparison_Smart1_loc_Te_3_5eV_phiE_20V_new_inlet_cond.lay

- Fig. 5.9 = > MyPC_Documentation/solar_panel_fluid_and_polytropic/
  comparison_fluid_poly/ESolution_files/ES_300k_fluid_poly_comparison.lay

- Fig. 5.10 = > MyPC_Documentation/solar_panel_fluid_and_polytropic/
  comparison_fluid_poly/ESolution_files/ES_300k_fluid_poly_comparison.lay

- Fig. 5.11 = > MyPC_Documentation/solar_panel_fluid_and_polytropic/
  comparison_fluid_poly/ESolution_files/ES_300k_fluid_poly_comparison.lay

- Fig. 5.12 => MyPC_Documentation/solar_panel_fluid_and_polytropic/
  comparison_fluid_poly/Solution_files/S_300k_fluid_poly_comparison.lay

- Fig. 5.13 => MyPC_Documentation/solar_panel_fluid_and_polytropic/
  comparison_fluid_poly/Solution_files/S_300k_fluid_poly_comparison.lay

- Fig. 5.14 => MyPC_Documentation/solar_panel_fluid_and_polytropic/comparison_fluid_poly/Solution_files/S_300k_fluid_poly_comparison.lay
- Fig. 5.15 => MyPC_Documentation/solar_panel_fluid_and_polytropic/comparison_fluid_poly/Solution_files/S_300k_fluid_poly_comparison.lay
- Fig. 5.16 => MyPC_Documentation/solar_panel_fluid_and_polytropic/comparison_fluid_poly/Solution_files/S_300k_fluid_poly_comparison.lay
- Fig. 5.17 => MyPC_Documentation/solar_panel_fluid_and_polytropic/comparison_fluid_poly/Solution_files/S_300k_fluid_poly_comparison.lay
- Fig. 5.18 => MyPC_Documentation/solar_panel_fluid_and_polytropic/comparison_fluid_poly/Solution_files/S_300k_fluid_poly_comparison.lay
- Fig. 5.19 => MyPC_Documentation/solar_panel_fluid_and_polytropic/comparison_fluid_poly/Solution_files/S_300k_fluid_poly_comparison.lay
- Fig. 5.20a => MyPC_Documentation/Sputtering/comparison/energy_comparison_at_different_probe_loc_y_0_15_0_30m.lay
- Fig. 5.20b => MyPC_Documentation/Sputtering/comparison/energy_comparison_at_different_probe_loc_y_0_30_0_45m.lay
- Fig. 5.20c => MyPC_Documentation/Sputtering/comparison/energy_comparison_at_different_probe_loc_y_0_45_0_60m.lay
- Fig. 5.21a = > MyPC_Documentation/Sputtering/comparison/angle_of_incidence_comparison_at_different_probe_loc_y_0_15_0_30m.lay
- Fig. 5.21b = > MyPC_Documentation/Sputtering/comparison/angle_of_incidence_comparison_at_different_probe_loc_y_0_30_0_45m.lay
- Fig. 5.21c = > MyPC_Documentation/Sputtering/comparison/angle_of_incidence_comparison_at_different_probe_loc_y_0_45_0_60m.lay
- Fig. 5.22a = > MyPC_Documentation/Sputtering/comparison/vz_comparison_at_different_probe_loc_y_0_15_0_30m.lay
- Fig. 5.22b = > MyPC_Documentation/Sputtering/comparison/vz_comparison_at_different_probe_loc_y_0_30_0_45m.lay
- Fig. 5.22c = > MyPC_Documentation/Sputtering/comparison/vz_comparison_at_different_probe_loc_y_0_45_0_60m.lay
- Fig. 5.23 => MyPC_Documentation/solar_panel_fluid_and_polytropic/comparison_fluid_poly/Solution_files/S_300k_fluid_poly_comparison.lay

References

[1] VanGilder, "Numerical Simulations of the Plumes of Electric Propulsion Thrusters," Ph.D. dissertation, Cornell University, 2000.

[2] S.-w. Kim, "Experimental Investigations of Plasma Parameters and Species-Dependent Ion Energy Distribution In the Plasma Exhaust Plume of a Hall Thruster," Ph.D. dissertation, University of Michigan, 1999.

[3] M. Tajmar, R. Sedmik, and C. Scharlemann, "Numerical Simulation of SMART-1 Hall-Thruster Plasma Interactions," *Journal of Propulsion and Power*, vol. 25, no. 6, pp. 1178–1188, 2009. [Online]. Available: http://arc.aiaa.org/doi/10.2514/1.36654

[4] M. David, J. Robert, and E. Frederick, "Hall Thruster Plume Measurements On-board the Russian Express Satellites," in *27th International Electric Propulsion Conference*, no. December, Pasadena, 2001. [Online]. Available: https://ntrs.nasa.gov/search.jsp?R=20020014412

[5] I. D. Boyd, "Numerical simulation of Hall thruster plasma plumes in space," *IEEE Transactions on Plasma Science*, vol. 34, no. 5 II, pp. 2140–2147, 2006.

[6] I. D. Boyd and R. A. Dressler, "Far field modeling of the plasma plume of a Hall thruster," *Journal of Applied Physics*, vol. 92, no. 4, pp. 1764–1774, 2002.

[7] R. Spektor and W. G. Tighe, "Laser Induced Fluorescence Measurements in a Hall Thruster as a Function of Background Pressure," *52nd AIAA/SAE/ASEE Joint Propulsion Conference*, pp. 1–7, 2016. [Online]. Available: http://arc.aiaa.org/doi/10.2514/6.2016-4624

[8] D. Y. Oh, D. E. Hastings, and C. M. Marrese, "Modeling of stationary plasma thruster-100 thruster plumes and implications for satellite design," *Journal of Propulsion and Power*, vol. 15, no. 2, pp. 345–357, 1999.

[9] F. Taccogna, D. Pagano, F. Scortecci, and A. Garulli, "Three-dimensional plume simulation of multi-channel thruster configuration," *Plasma Sources Science and Technology*, vol. 23, no. 6, p. 065034, 2014. [Online]. Available: http://stacks.iop.org/0963-0252/23/i=6/a=065034?key=crossref.919c577f37ebaabc354e9999be211c35

[10] M. Tajmar, J. González del Amo, and A. Hilgers, "Modeling of Spacecraft - Environment Interactions on SMART-1 Introduction," *Journal of Spacecraft and Rockets*, vol. 38, no. 3, pp. 393–399, 2001.

[11] B. Korkut, D. A. Levin, and O. Tumuklu, "Simulations of Ion Thruster Plumes in Ground Facilities Using Adaptive Mesh Refinement," *Journal of Propulsion and Power*, vol. 33, no. 3, pp. 681–696, 2017. [Online]. Available: https://doi.org/10.2514/1.B35958

[12] J. Wang, D. Brinza, and M. Young, "Three-Dimensional Particle Simulation Modeling of Ion Propulsion Plasma Environment for Deep Space 1," *Journal of Spacecraft and Rockets*, vol. 38, no. 3, pp. 433–440, 2001. [Online]. Available: http://trs-new.jpl.nasa.gov/dspace/handle/2014/15643{%}5Cnhttp://doi.aiaa.org/10.2514/2.3702

[13] M. Santi, S. Cheng, M. Celik, M. Martinez-Sanchez, and J. Peraire, "Further Development and Preliminary Results of the AQUILA Hall Thruster Plume Model," *39th AIAA/ASME/SAE/ASEE Joint Propulsion Conference and Exhibit, Huntsville, Alabama, July 20-23, 2003*, no. July, pp. AIAA–2003–4873, 2003.

[14] L. Brieda and M. Keidar, "Multiscale Modeling of Hall Thrusters," *Iepc*, pp. 1–13, 2013.

[15] F. Cichocki, M. Merino, P. Fajardo, E. Ahedo, S. Propulsion, A. Dom\inguez, F. Cichocki, M. Merino, P. Fajardo, and E. Ahedo, "2D and 3D hybrid PIC-fluid modeling of electric thruster plumes," *35th International Electric Propulsion Conference, paper*, pp. 17–209, 2017.

[16] R. Jambunathan and D. A. Levin, "CHAOS: An octree-based PIC-DSMC code for modeling of electron kinetic properties in a plasma plume using MPI-CUDA parallelization," *Journal of Computational Physics*, vol. 373, pp. 571–604, 2018. [Online]. Available: https://doi.org/10.1016/j.jcp.2018.07.005

[17] M. Mitchner and C. H. Kruger, *Partially Ionized Gases*, 1973, vol. 20.

[18] I. D. Boyd and J. T. Yim, "Modeling of the near field plume of a Hall thruster," *Journal of Applied Physics*, vol. 95, no. 9, pp. 4575–4584, 2004.

[19] I. G. Mikellides and I. Katz, "Numerical simulations of Hall-effect plasma accelerators on a magnetic-field-aligned mesh," *Physical Review E - Statistical, Nonlinear, and Soft Matter Physics*, vol. 86, no. 4, pp. 1–17, 2012.

[20] F. Taccogna, S. Longo, and M. Capitelli, "Particle-in-Cell with Monte Carlo Simulation of SPT-100 Exhaust Plumes," *Journal of Spacecraft and Rockets*, vol. 39, no. 3, pp. 409–419, 2002.

[21] B. Korkut, "Development of a Scalable Gas-Dynamics Solver With Adaptive Mesh Refinement," Ph.D. dissertation, Pennsylvania State University, 2015.

[22] M. Nakano, "Doubly charged ion effect on life prediction accuracy of ion acceleration grid system," *Vacuum*, vol. 88, no. 1, pp. 70–74, 2013. [Online]. Available: http://dx.doi.org/10.1016/j.vacuum.2012.02.027

[23] J. S. Miller, S. H. Pullins, D. J. Levandier, Y. H. Chiu, and R. A. Dressler, "Xenon charge exchange cross sections for electrostatic thruster models," *Journal of Applied Physics*, vol. 91, no. 3, pp. 984–991, 2002.

[24] S. J. Araki and R. E. Wirz, "Ion-neutral collision modeling using classical scattering with spin-orbit free interaction potential," *IEEE Transactions on Plasma Science*, vol. 41, no. 3, pp. 470–480, 2013.

[25] M. K. Scharfe, J. Koo, and G. Azarnia, "DSMC Implementation of Experimentally-Based Xe^{+}+Xe Differential Cross Sections for Electric Propulsion Modeling," in *American Institute of Physics Conference Series*, ser. American Institute of Physics Conference Series, vol. 1333, May 2011, pp. 1085–1090.

[26] M. Choi, I. Boyd, and U. of Michigan, "Numerical Simulation of the Cathode Plume of a Hall Thruster," *50th Joint Propulsion Conference*, pp. 1–12, 2014.

[27] K. Dannenmayer and S. Mazouffre, "Electron flow properties in the far-field plume of a Hall thruster," *Plasma Sources Science and Technology*, vol. 22, no. 3, 2013.

[28] G. Giono, J. T. Gudmundsson, N. Ivchenko, S. Mazouffre, K. Dannenmayer, D. Loubère, L. Popelier, M. Merino, and G. Olentšenko, "Non-Maxwellian electron energy probability functions in the plume of a SPT-100 Hall thruster," *Plasma Sources Science and Technology*, vol. 27, no. 1, 2018.

[29] M. Nakles, L. Brieda, G. Reed, W. Hargus, and R. Spicer, "Experimental and Numerical Examination of the BHT-200 Hall Thruster Plume," *43rd AIAA/ASME/SAE/ASEE Joint Propulsion Conference and Exhibit*, vol. 3, no. July, pp. 3041–3058, 2007. [Online]. Available: http://arc.aiaa.org/doi/abs/10.2514/6.2007-5305

[30] E. Ahedo, P. Martínez-Cerezo, and M. Martínez-Sánchez, "One-dimensional model of the plasma flow in a Hall thruster," *Physics of Plasmas*, vol. 8, no. 6, pp. 3058–3068, 2001.

[31] Y. Choi, I. D. Boyd, A. D. Gallimore, B. E. Gilchrist, and M. Keidar, "Modeling an Anode Layer Hall," 2008.

[32] M. Keidar, I. D. Boyd, and I. I. Beilis, "Plasma flow and plasma-wall transition in Hall thruster channel," *Physics of Plasmas*, vol. 8, no. 12, pp. 5315–5322, 2001.

[33] M. Choi, "Improved Hall Thruster Plume Simulation by Including Magnetic Field Effects by," 2016.

[34] R. S. Roy, "Numerical simulation of ion thruster plume backflow for spacecraft contamination assessment," Ph.D. dissertation, 1995. [Online]. Available: http://hdl.handle.net/1721.1/11397

[35] R. Jambunathan and D. A. Levin, "Advanced parallelization strategies using hybrid MPI-CUDA octree DSMC method for modeling flow through porous media," *Computers and Fluids*, vol. 149, pp. 70–87, 2017. [Online]. Available: http://dx.doi.org/10.1016/j.compfluid.2017.02.020

[36] E. Haber, U. M. Ascher, D. A. Aruliah, and D. W. Oldenburg, "Fast Simulation of 3D Electromagnetic Problems Using Potentials," *Journal of Computational Physics*, vol. 163, no. 1, pp. 150–171, 2000.

[37] D. Book and J. Huba, "Nrl plasma formulary," Naval Research Lab Washingthon DC Plasma Physics Div, Tech. Rep., 2016.

[38] F. Taccogna, "Very-near-field plume simulation of a stationary plasma thruster," *The European Physical Journal Applied Physics*, vol. 28, pp. 113–122, 2004.

[39] B. Korkut and D. A. Levin, "Three-dimensional simulations of backflows from ion thruster plumes using unstructured grid refinement," *Journal of Propulsion and Power*, pp. 264–275, 2016.

[40] H. Maejima, S. Kawakita, H. Kusawake, M. Takahashi, T. Goka, T. Kurosaki, M. Nakamura, K. Toyoda, and M. Cho, "Investigation of Power System Failure of a LEO Satellite," *2nd International Energy Conversion Engineering Conference*, no. August, pp. 1–6, 2004. [Online]. Available: http://arc.aiaa.org/doi/10.2514/6.2004-5657

[41] R. J. Procassini, C. K. Birdsall, and E. C. Morse, "A fully kinetic, self-consistent particle simulation model of the collisionless plasma-sheath region," *Physics of Fluids B*, vol. 2, no. 12, pp. 3191–3205, 1990.

[42] S. J. Araki and A. Barrie, "Electric Propulsion Plume Simulation Coupled with Spacecraft Charging," no. 18333, 2018.

[43] S. T. Lai, *Fundamentals of spacecraft charging: spacecraft interactions with space plasmas*. Princeton University Press, 2011.

[44] J. A. Young, "Ion plume damage in formation flight regimes," Ph.D. dissertation, 2017.

[45] J. Bohdansky, "A universal relation for the sputtering yield of monatomic solids at normal ion incidence," *Nuclear Inst. and Methods in Physics Research, B*, vol. 2, no. 1-3, pp. 587–591, 1984.

[46] Y. Yamamura and S. Shindo, "An empirical formula for angular dependence of sputtering yields," *Radiation Effects*, vol. 80, no. 1-2, pp. 57–72, jan 1984. [Online]. Available: http://www.tandfonline.com/doi/abs/10.1080/00337578408222489

[47] M. Tajmar, B. Foing, J. Gonzalez, and G. Noci, "Charge-Exchange Plasma Contamination on SMART-1: First Measurements and Model Verification," *40th AIAA/ASME/SAE/ASEE Joint Propulsion Conference and Exhibit, Fort Lauderdale, Florida, July 11-14, 2004*, no. July, pp. AIAA–2004–3437, 2004.

[48] J. Bernard, Y. Garnier et al., "Numerical simulation of induced environment, sputtering and contamination of a satellite due to electric propulsion," in *European Spacecraft Propulsion Conference*, vol. 398, 1997, p. 517.